

Microjet Based Noise Control of Supersonic Jets On Carrier Decks

by

Paul Aaron Ragaller

S.B. Mechanical Engineering
Case Western Reserve University, 2005

S.M. Mechanical Engineering
Massachusetts Institute of Technology, 2007

Submitted to the Department of Mechanical Engineering
in Partial Fulfillment of the Requirements for the Degree of

Doctor of Philosophy in Mechanical Engineering

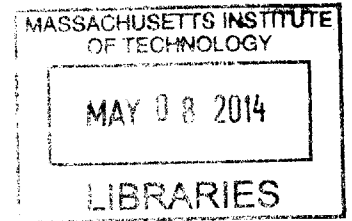
at the


Massachusetts Institute of Technology

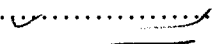
February, 2014

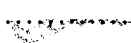
© 2014 Massachusetts Institute of Technology
All rights reserved

ARCHIVES



Signature of Author.....
 Department of Mechanical Engineering
December 10, 2013

Certified by.....

Anuradha Annaswamy
Senior Research Scientist
Thesis Supervisor

Accepted by.....
 David Hardt
Chairman, Committee for Graduate Students

Microjet Based Noise Control of Supersonic Jets On Carrier Decks

by

Paul Aaron Ragaller

Submitted to the Department of Mechanical Engineering
on December 10, 2014 in Partial Fulfillment of the
Requirements for the Degree of Doctor of Philosophy in
Mechanical Engineering

ABSTRACT

The effectiveness of ground plane water microjet control on the noise generated by a supersonic, ideally expanded, Mach 1.5, impinging jet was determined. Using a converging-diverging nozzle with a design Mach number of 1.5, the jet was operated at temperatures ranging from 60 to 1700°F. Six microjets were installed in the ground plane in a circular configuration at a radial spacing of 1.53 nozzle diameters, and an angle of 0 and 30° to tangential. Baseline and control temperature readings at the ground plane and acoustic readings at the sideline angles of 70, 80 and 90° were obtained with the microjets operating at pressures ranging from 200 to 900 psig. Additionally, in order to determine the fluid-mechanical mechanisms responsible for the control effect on the noise, high-speed images and video were obtained and analyzed.

From measurements of the average and fluctuating ground plane temperature measurements, it was found that modifications to the High Temperature Supersonic Jet Facility at Florida State University allowed for measurements of impinging jet characteristics that were congruent with previous studies.

Ground plane microjets were found to be effective in reducing feedback tones as a result of the impinging geometry of the jet. They were also effective at reducing the broadband spectral noise for lower temperatures. At temperatures higher than 600°F, however, an increase in the broadband noise was produced as a result of water microjets. At microjet injection pressures at and above 800 psig, additional noise suppression was achieved for the cold operating condition.

From obtained high-speed images and video, it was found that the breakup of the microjet in the shear layer (of the shear variety), and the entrainment of fine mist into the inception of the shear layer was responsible for the reduction in strength and size of large-scale vortical structures. At higher pressures, additional noise suppression is produced as a combined result of the breaking of the feedback loop and the microjet's ability to penetrate to the high-speed side of the shear layer.

Thesis Supervisor: Anuradha Annaswamy
Title: Senior Research Scientist

ACKNOWLEDGEMENTS

First and foremost, I would like to thank Dr. Anuradha Annaswamy, my thesis advisor, for her guidance, support, enthusiasm and attention to detail. With her leadership I have changed my way of thinking and have learned to see the bigger picture. I would also like to thank Professor Ahmed Ghoniem and Professor Doug Hart, both of whom gave countless hours of guidance and advice. Without their eye to detail this thesis would not have been possible.

The work performed at Florida State University would never have been possible without the help of several people. I would like to thank Dr. Anjaneyulu Krothapalli, Dr. Farrukh Alvi and Dr. Jonas Gustavsson for their expertise, enthusiasm and dedication to this project. I would also like to extend a special thanks to Dr. Brenton Greska for allowing me to absorb as much knowledge about jet noise, the facility and experimentation in general as possible during my time in the facility. Special mention goes to Bobby Avant, the lab machinist, who made many of the facility adaptations possible.

I would like to extend a very special thanks to Professor John Leonard for taking a chance on me to be his teaching assistant for 2.671. Being involved in the course these past years has truly changed me as a person, and has enabled me to grow into a mentor and instructor. And without his advocacy, I would have never been able to accomplish what I have.

Thank you, Dr. Barbara Hughey, for being a support structure, advocate, sounding board, shoulder and, most importantly, good friend. You have enriched my experience at MIT in ways I couldn't even begin to describe. You are undeniably a treasure to all who you encounter, and I am grateful to have been among those to be lucky enough to get to know you.

Thanks to my mother, Carol, for lending her support and her occasional reminders that deadlines are closer than they appear. Thanks to my father, Bill, for his encouragement and reinforcement – and for knowing exactly what to say at the most difficult of times. Thanks to my husband, Noah, for being so proud of me and for sharing my emotions, challenges and accomplishments. Thank you for making me laugh when I needed it most. This work is dedicated to you.

The help and consideration of those mentioned above is sincerely appreciated.

TABLE OF CONTENTS

LIST OF FIGURES.....	9
LIST OF TABLES.....	13
1. INTRODUCTION AND BACKGROUND.....	15
2. EXPERIMENTAL SETUP.....	33
2.1 Overview.....	33
2.2 High Pressure Air Supply.....	34
2.3 Burner Room.....	35
2.4 Nozzles.....	38
2.5 Microjet Injection.....	39
2.6 Anechoic Chamber.....	40
2.7 Control Room.....	41
2.8 Ground Plane Test Stand.....	41
2.9 Ground Plane Temperature and Pressure Measurement.....	45
2.10 Acoustic Measurement.....	47
2.11 Calibration.....	49
2.12 Ground Plane Microjet Imaging.....	50
3. EXPERIMENTAL PROCEDURE.....	53
3.1 Overview.....	53
3.2 Experimental Description.....	53
3.2.1 Ground Plane Pressure and Temperature Fluctuation.....	53
3.2.2 Baseline Noise Characterization.....	54
3.2.3 Nozzle Microjet Injection.....	54

3.2.4	Ground Plane Microjet Injection.....	55
3.2.5	High-Speed Microjet Imaging.....	55
3.3	Experimental Procedure.....	56
3.4	Acoustic Data Processing and Analysis.....	58
3.4.1	Frequency Spectra.....	58
3.4.2	Overall Sound Pressure Level.....	59
3.4.3	Skewness.....	60
3.4.4	Injector Flow Rates.....	60
3.5	Uncertainty Estimates.....	60
3.5.1	Acoustic Uncertainty.....	61
4.	RESULTS AND DISCUSSION.....	63
4.1	Overview.....	63
4.2	Characterization of the High-Temperature, Supersonic Jet Facility.....	63
4.3	Ground Plane Temperature Measurements.....	68
4.4	Noise Reduction with Ground Plane Fluid Microjets.....	70
4.4.1	Ground Plane Water Microjet Injection.....	70
4.4.2	Comparison with Microjet Injection at the Nozzle Exit.....	76
4.4.3	The Effect of Working Fluid Type.....	77
4.4.4	The Effect of Radial Position.....	78
4.4.5	The Effect of Injection Angle.....	79
4.5	High-Speed Imaging and Noise Reduction Mechanisms.....	81
5.	CONCLUSIONS AND FUTURE STUDY.....	109
5.1	Conclusions.....	109
5.2	Future Work Plan.....	118
	BIBLIOGRAPHY.....	131

LIST OF FIGURES

1.1: Simple schematic of the development of a high-speed jet as it issues into the ambient medium.	17
1.2: The three main noise sources and their contributions to the narrowband frequency spectrum.	18
1.3: Narrowband spectra for water injection at 100 psig.	19
1.4: Simple illustration of the inception and growth of large, coherent structures, and the entrainment of fluid within.	20
1.5: Schematic of the simultaneous growth and propagation of coherent eddies and Mach wave radiation.	21
1.6: Figure showing two distinct source locations for mach wave radiation.	22
1.7: Narrowband frequency spectra in the peak noise radiation direction illustrating the effects of Mach wave radiation.	23
1.8: Schematic of the screech tone generation mechanism.	24
1.9: Schematic of (a) an impinging jet flow field and (b) the flow field of a carrier aircraft with a blast deflector.	26
1.10: Droplet breakup regimes as a function of Ohnesorge and Weber numbers.	31
2.1.1: Simple schematic of the high-temperature, supersonic jet facility.	34
2.2.1: Simple schematic of the air supply system.	35
2.3.1: Cross section of the Venturi.	37
2.4.1: Nozzle types.	38
2.5.1: Microjet injection at the nozzle exit.	39
2.5.2: Simple schematic of the microjet injection system.	40
2.8.1: Schematic of the ground plane.	42
2.8.2: Depiction of the anechoic chamber with the moveable impingement plane.	43

2.8.3: Photograph of the back side of the ground plane with toroidal microjet supply manifold and microjet supply tubing.	44
2.8.4: Photograph of the front of the ground plane showing the detachable microjet center structure during the firing of the microjets.	45
2.9.1: Photograph of the Kulite WCT-312 water-cooled pressure transducer.	46
2.9.2: Photograph of a typical K-type thermocouple probe.	46
2.9.3: Schematic of the (a) front side and (b) back side of the custom designed, water-cooled Kulite and thermocouple housing block.	47
2.10.1: Simple schematic of a condenser microphone.	48
2.10.2: Microphone locations within the anechoic chamber.	49
2.12.1: Simple, overhead schematic of the anechoic chamber, as set up for the high speed imaging tests.	51
3.2.1: Sample high-speed image of the nozzle and shear layer.	55
3.2.2: Contour map for a microjet operating at 800 psig, overlaid on a sample image.	56
4.2.1: Summary of ground plane pressure fluctuations for (a) the High-Temperature, Supersonic Jet Facility taken at $h/d=8$ and for (b) the STOVL facility.	64
4.2.2: Ground plane frequency spectra for various jet exhaust temperatures at (a) $h/d=4$, (b) $h/d=6$ and (c) $h/d=8$	66
4.2.3: Ground plane frequency spectra at varying radial locations for an axial distance of $h/d=4$ for a jet operating at (a) the cold condition and (b) 900°F	67
4.3.1: Mean temperature profiles for a jet with ground plane located downstream of the nozzle exit at (a) $h/d=8$ and (b) $h/d=10$	68
4.3.2: Temperature fluctuations on the ground plane for a Mach 1.5 jet at (a) an axial distance of $h/d=8$ and (b) an axial distance of $h/d=10$	69
4.4.1: Spectra for the 80 and 90 degree microphones at an axial distance of 8 nozzle diameters.	71
4.4.2: Spectra for the 80 and 90 degree microphones at an axial distance of 10 nozzle diameters.	72
4.4.3: Overall sound pressure levels for the 80° and 90° microphones at various temperatures.	73
4.4.4: Reduction in farfield OASPL as a function of injection pressure for the 70, 80 and 90 degree locations with the ground plane at $h/d=8$	74

4.4.5: Reduction in farfield OASPL of a jet operating at 600°F as a function of injection pressure for the 70, 80 and 90 degree locations with the ground plane at $h/d=8$	75
4.4.6: Summary plot of noise reduction as a function of jet temperature for 800 psig water microjets at the nozzle exit for an impinging jet at $h/d=8$	76
4.4.7: Summary plot of noise reduction as a function of injection pressure for a cold jet.	77
4.4.8: Reduction of farfield jet noise as a function of injection pressure for Nitrogen microjets at the nozzle exit.	78
4.4.9: Summary plot of noise reduction as a function of temperature for water microjets at varying radial locations.	79
4.4.10: Frequency spectra for a cold jet at $h/d=8$ for microjets at $r/d=1.53$ firing (a) tangentially and (b) obliquely.....	80
4.5.1: Simple schematic showing the two noise reduction mechanisms and their regions of impact with respect to the frequency spectrum.	82
4.5.2: Comparison of the microjet behavior with the resulting noise reduction.....	83
4.5.3: Plot of average pixel value as a function of time for each microjet injection pressure.	86
4.5.4: Average shear layer pixel value as a function of injection pressure.	87
4.5.5: Zoomed shear layer brightness and corresponding Fast Fourier Transform.	89-90
4.5.6: Narrowband spectra for water injection at 100 psig.	92
4.5.7: Schematic of the effect of the droplet breakup mechanism on the frequency spectra.	93
4.5.8: Contour plot overlaid on a sample high-speed image showing the different regimes of the shear layer.	95
4.5.9: Brightness contour plot for the microjet operating at 200 psig.	96
4.5.10: Brightness contour plots for a microjet operating at (a) 400 psig, (b) 600 psig, (c) 700 psig and (d) 800 psig.	98
4.5.11: Brightness contour plot for a microjet injection pressure of 900 psig.	99
4.5.12: Upstream penetration depth as a function of microjet injection pressure.	100
4.5.13: Inward penetration depth as a function of microjet injection pressure.	101

4.5.14: OASPL as a function of injection pressure matched with its corresponding frequency spectrum.	103
4.5.15: Skewness of the pressure-time signal for baseline and control signals as a function of microjet injection pressure.	106
4.5.16: Simple summary schematic showing the effect of microjet penetration on the frequency spectra.	107
5.1: Schematic of the jet engine with a control volume	117
5.2: The three main noise sources and their contributions to the narrowband frequency spectrum.	119
5.3: Shear layer turbulence profiles showing the jet (a) without control and (b) with water microjet control	120
5.4: Normalized turbulence profiles within the shear layer for a jet (a) with no control and (b) with atomized microjet injection.....	121
5.5: Unprocessed Schlieren image showing the presence of Mach wave radiation	122
5.6: Schematic of a TSI Powersight solid-state, laser-based phase Doppler particle analyzer	124
5.7: Simple schematic of the PIV setup	125
5.8: Simple schematic of the schlieren setup	127

LIST OF TABLES

3.1: Experimental Run Conditions.....57
4.5.1: Range of Ohnesorge and Weber numbers used in this experiment..... 85
5.1: Experimental summary for future work129

CHAPTER 1

INTRODUCTION AND BACKGROUND

As passenger and military aircraft become larger, faster and more powerful, the noise generated by their engines becomes louder. In the commercial setting, most aircraft travel subsonically. Their engines are of the high-bypass, turbofan variety, which consist of two parts. At the center is a powerful gas turbine. Air enters the turbine and is compressed by the many rows of blades, then mixes with fuel. The fuel-air mixture combusts in the center of the turbine, then exits at high velocity through another set of blades. The combusted, high-speed air is exhausted through a relatively small nozzle. Meanwhile, ambient air is drawn around the outside of this turbine by a large fan. The mass of air drawn around the turbine is sometimes three times more than the air drawn into the turbine itself—hence the term “high-bypass”. As such, a large amount of fluid is accelerated by only a small amount. Originally designed to provide more thrust, the co-flow exhaust of these engines also helps to reduce the noise generated—an unintended advantage. The noise pollution caused by such aircraft during takeoff, landing and run-up time (the time the aircraft spends idle or taxiing with the engines on), however, becomes a serious issue with regards to neighborhoods that surround and encroach upon airports. This drives property values down and poses a general annoyance to those citizens living nearby. Military aircraft are generally supersonic and are powered by turbojet engines. These engines are similar to those used on commercial aircraft but with different inlet geometry which decelerates the fluid to subsonic speeds, thus abating the harmful effects of shock waves. The high-pressure, high-temperature exhaust then passes through a converging-diverging nozzle, which accelerates the fluid to supersonic speeds. The balance of momentum across the engine produces a large amount of thrust. Though

military aircraft rarely operate near residential areas and pose little annoyance to the general public, they do operate frequently within the confines of military vessels, such as aircraft carriers. Such carriers require on-deck labor—this means that someone must stand on deck and guide these aircraft during run-up and takeoff. However, the development of equipment designed to protect these deckhands against the harmful effects of high-intensity noise generated by these aircraft has not kept up with the development of faster, more powerful engines. This leaves these individuals exposed to harmful noise radiation. Therefore, any method or device designed to reduce the noise generated by an aircraft, without also reducing thrust, would prove advantageous on all fronts of this issue.

The greatest public misconception regarding the source of jet noise is the belief that the majority of the noise is generated within the engine itself. While it is true that some noise is produced by the combustion process and from moving and vibrating parts within the engine, this noise does not contribute significantly to the overall noise production of the jet engine. Interestingly, the majority of the noise is generated aft of the nozzle exit. There are two main processes that contribute substantially to the generation of jet noise—though understanding them requires a small amount of background knowledge of the structure of a free jet.

In practice, as well as in experimentation, high-speed fluid generated within the jet engine exhausts to open atmosphere. Whether this open atmosphere is quiescent, as in the laboratory setting, or moving, as with an aircraft, it generally appears to be moving with a much lower velocity with respect to the jet exhaust. Therefore, the jet of high-speed exhaust fluid is forced to interact with the ambient fluid. Figure 1.1 is a simple schematic of a high-speed jet issuing into ambient fluid.

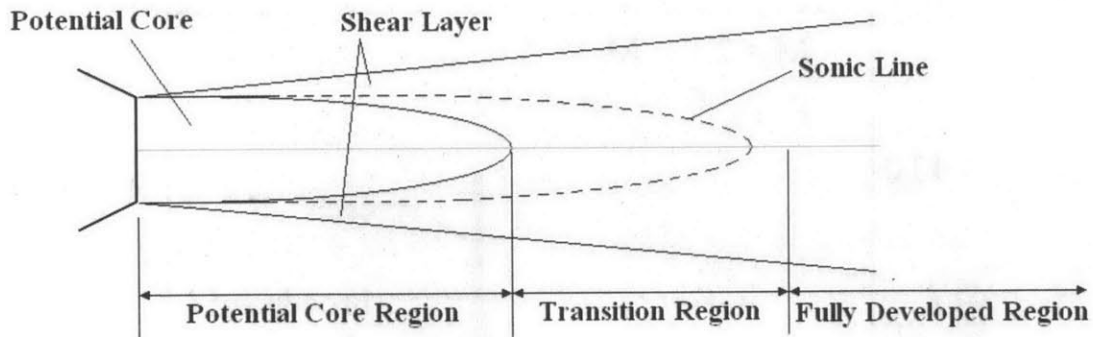


Figure 1.1: Simple schematic of the development of a high-speed jet as it issues into the ambient medium. The center most region of the jet is known as the potential core, and is defined as where the bulk fluid velocity is 99% that of the main jet exhaust. The potential core is bounded by the shear layer. The potential core ends where the shear layers meet in the middle – this is the beginning of the transition region.

As the jet issues into the ambient medium, viscous forces cause velocity gradients to form at the boundary of the jet, which in turn causes the two fluids to mix. The region where these gradients and mixing occur is known as the shear layer. Moving downstream, the thickness of the shear layer grows and intrudes on the potential core. The potential core is the region of the jet where the axial velocity is at least 99% of the velocity of the fluid exiting the nozzle. Eventually, the shear layers meet in the middle and the potential core ends. This is the beginning of the transition region. Even farther downstream, the velocity profiles become self-similar and the jet is in its fully developed region. The growth rate of the shear layer, and thus the length of the potential core, varies depending on the running conditions of the jet. Also pictured in Figure 1.1 is the sonic line. Inside the sonic line, the fluid is moving faster than the speed of sound relative to the ambient medium.

In 1977, Crighton [1] concisely outlined the three main components of jet noise: turbulent mixing noise, resonance and broadband shock noise. Later, in an investigation into the effect and optimization of water injection as a means of noise suppression, Kandula [2] modified a figure published by Crighton to highlight the contributions of each of the noise sources to the narrowband frequency spectrum. It is reproduced here in Figure 1.2.

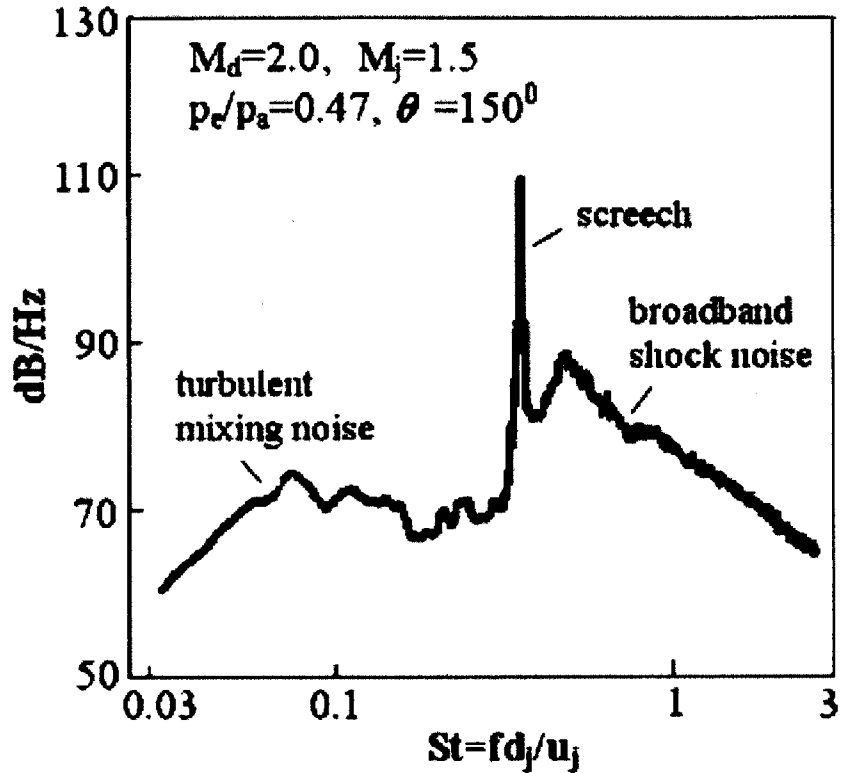


Figure 1.2: The three main noise sources and their contributions to the narrowband frequency spectrum.

In his PhD thesis, Greska demonstrated that, through the use of low-pressure water jet injection at the nozzle exit, reductions in noise could be produced [3]. In his study, the 100 psig water jets were able to produce low-frequency reduction. However, there was a crossover in the spectrum where, at very high frequency, the noise was increased. This result is reproduced in Figure 1.3. He attributed this to the water jets' inability to penetrate the high-speed side of the shear layer. As such, he attributed the low-frequency noise reduction to the droplet breakup effect discussed by Krothapalli et al [4].

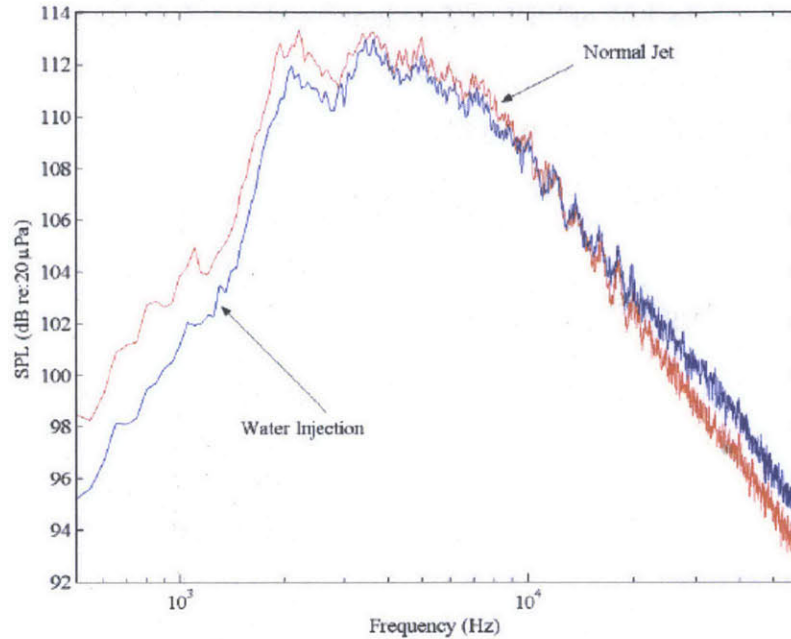


Figure 1.3: Narrowband spectra for water injection at 100 psig, as reproduced from Greska [3]. Spectral reductions were achieved at lower frequencies, which was attributed to the water droplet breakup mechanism described in earlier studies.

Krothapalli et al discussed the effects of the breakup of the microjet on the properties of the main jet [4]. Outside of the injection region, they showed that no appreciable difference to the mean flow structure was observed. However, they did show that the mean turbulence profiles were reduced through the use of water jets – this effect was attributed to the droplet breakup process. This result corroborates similar reductions in turbulence for particle-laden flows [5]. In addition, at the sideline angle of 90 degrees, they showed reductions in both near and farfield jet noise that corroborate the results obtained by Greska [3].

In the nearfield, results show a reduction along all frequencies. However, in the farfield, results show reduction of lower frequencies with no significant changes at high frequencies. They attribute this to the reduction of large-scale mixing – with which water injection “appears to interfere constructively,” and that this interference results in SPL reductions at low frequencies.

One point of confusion so far is why past studies have attributed a reduction in large-scale, low-frequency mixing noise with a droplet breakup effect. Washington et al

[6] showed, through the use of PIV and shadowgraph imaging, that these large-scale phenomena are reduced in size and strength by entrained, atomized water droplets. Therefore, their contribution to the overall noise levels may be reduced.

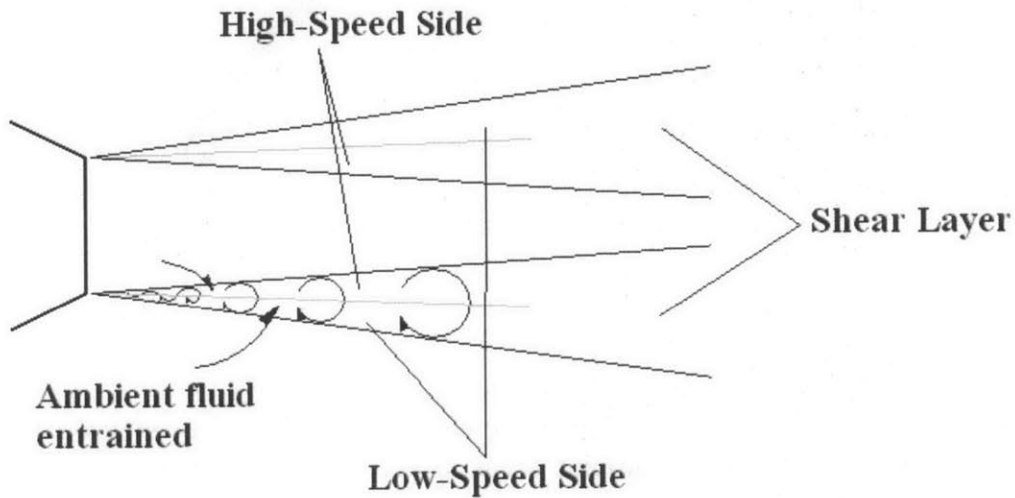


Figure 1.4: Simple illustration of the inception and growth of large, coherent structures, and the entrainment of fluid within. Instabilities due to large shear forces at the nozzle exit cause small rotating vortical structures to form. These structures grow, combine, and entrain the ambient environment thus increasing the mixing of the jet shear layer.

As stated before, the growth rate of the shear layer depends entirely on the properties of the jet. However, Papamoschou and Roshko were some of the first to discover that the shear layer of a supersonic jet grows more slowly than that of a subsonic jet [7]. This lends itself to the fact that supersonic jets have longer potential cores than their subsonic counterparts. The potential core itself is a large source of broadband mixing noise. Aside from this, Crow and Champagne found that velocity gradients were responsible for producing coherent structures with high vorticity [8]. These structures propagate downstream at velocities greater than the speed of sound with respect to the ambient medium. Moore found that these eddies are formed from initial instability waves and grow as they travel downstream [9]. He also found that these eddies entrain ambient fluid and can interact with each other, thus enhancing mixing in the shear layer. Figure 1.4 is a simple illustration of this concept. This figure also shows a light line roughly delineating the low-speed and high-speed sides of the shear layer. These coherent

structures were found by Bishop, Ffowcs Williams and Smith to be responsible for Mach wave radiation, another significant noise source in a supersonic jet [10]. Figure 1.4 shows a simple schematic of the growth of these eddies with respect to Mach wave radiation. Bishop, Ffowcs Williams and Smith also noted that the Mach waves tended to favor the high-speed side of the shear layer [10]. Thus, the Mach waves seem to be born from the extreme pressure gradients at the leading edge of each eddy. Therefore, as in Figure 1.5, the Mach waves are formed and propagate from the leading edge of the structure.

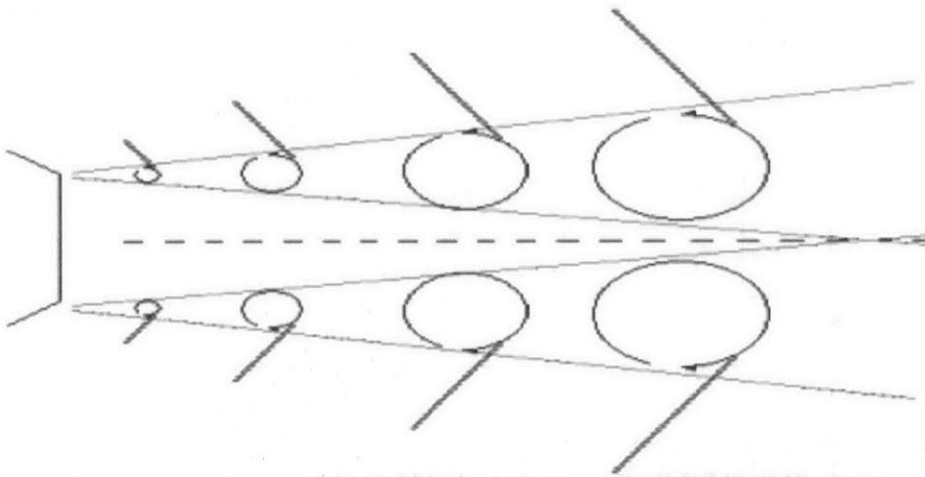


Figure 1.5: Schematic of the simultaneous growth and propagation of coherent eddies and Mach wave radiation. If the convective Mach number of these eddies is larger than 1, implying a supersonic speed with respect to the ambient environment, ballistic shock waves will form on the leading edge causing Mach wave radiation.

Crighton [1] describes two classes of Mach wave radiation: high frequency, short wavelength and low frequency, high intensity. The high-frequency, short-wavelength sources are present especially in supersonic jets where the shear layer is thinner. They are associated with the 1-4kHz range at full scale. The low-frequency sources are caused by large-scale structures.

The two types of Mach wave radiation were shown by Laufer et al to be found primarily at two axial locations [11]. The higher frequency source is found between 6 and 8 nozzle diameters downstream, while the lower frequency source is found between 14-16 nozzle diameters downstream. The two main conclusive graphs of these types of

Mach wave radiation are represented for the reader's convenience in Figure 1.6. It should be noted that, within the scope of the experiments performed for this thesis, a ground plane was used and positioned at 8 nozzle diameters downstream of the nozzle exit. Because of the geometric constraints of the experimental setup, the main jet was not allowed to evolve to the point required to produce this particular source. Therefore, the higher-frequency Mach wave radiation class, associated with smaller-scale structures, is not present.

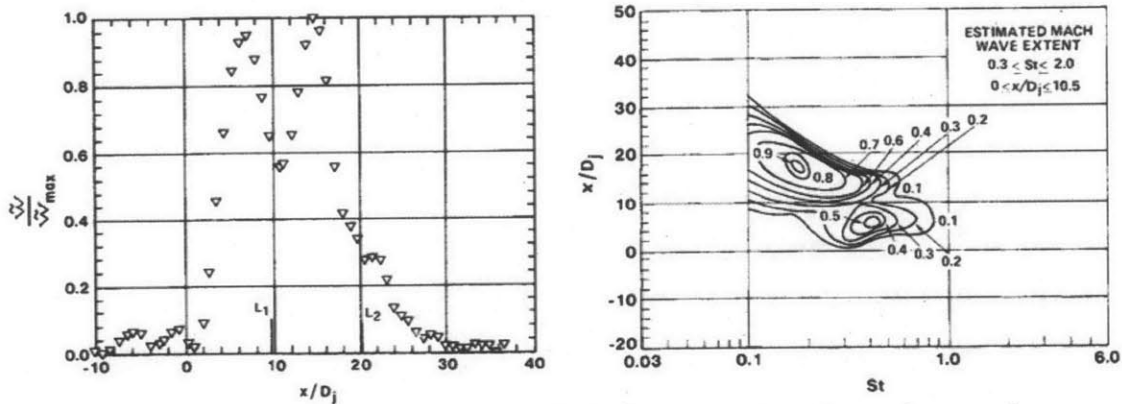


Figure 1.6: Figure showing two distinct source locations for mach wave radiation, as reproduced from Laufer et al [11]. The larger-scale, lower-frequency source is found primarily between six and eight nozzle diameters downstream. The smaller-scale, higher-frequency source, which is found primarily between 14 and 16 nozzle diameters downstream, is not present in the current study as a result of the specific geometric constraints of the experimental setup.

Greska et al [12] presents a normalized spectra, reproduced in Figure 1.7, which shows the effect of Mach wave radiation on the noise profile of a jet. The two profiles suggest that, when the convective Mach number is less than 1, the jet is acoustically subsonic. However, when the convective Mach number is greater than 1, Mach wave radiation is present and there is an increase in higher-frequency noise. From Greska, “the operating conditions of the lower spectral trend result in acoustically subsonic jets...where eddy convection in the source region is the primary noise generator of these higher frequencies. The operating conditions for the upper spectral trend result in supersonic jets with eddy convection and Mach wave radiation.”

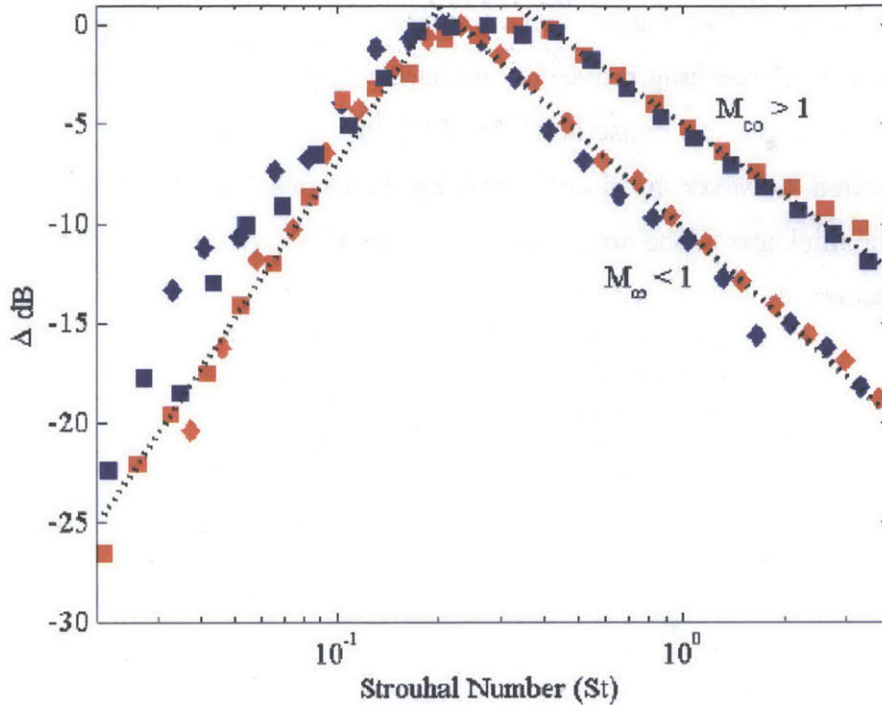


Figure 1.7: Narrowband frequency spectra in the peak noise radiation direction illustrating the effects of Mach wave radiation. These spectra were normalized with the peak spectral magnitude, where a 0 dB difference corresponds to the maximum – that is, a gain of 1. If the convective Mach number is less than unity, the noise is made up entirely of turbulent mixing noise. If the convective Mach number is greater than unity, the spectral shape is similar, however there is an increase in the spectral content at higher frequencies. This demonstrates the effect of Mach wave radiation on the spectral profile of a jet.

Due to the asymmetric shape of the shear layer, it was found that both large and small-scale structures favor the high-speed side of the shear layer [1]. Reducing these sources would require that the control be able to reach the high-speed side of the shear layer.

Aside from mixing noise and Mach wave radiation, screeching also contributes significantly to supersonic jet noise. Screeching, however, is generally only present when the jet is operated with an off-design condition. Screech tones occur at discrete frequencies, and were first identified by Powell [13]. Small disturbances born at the nozzle exit propagate downstream. They sometimes interact with the shock cells in the shear layer and part of the sound is reflected back upstream, as in Figure 1.8. This reflected disturbance reflects off the lip of the nozzle, or some other hard surface, and

enhances the original disturbance. This process of feedback continues until a screech tone is generated. Screeching proves to be a larger problem than simple tones: Alkislar showed that screeching can cause heightened Mach wave radiation [14]. Screech tones are easily quelled, however, by simply breaking the feedback loop. This can be done by decreasing the thickness of the nozzle lip or through the use of an external control such as microjet injection.

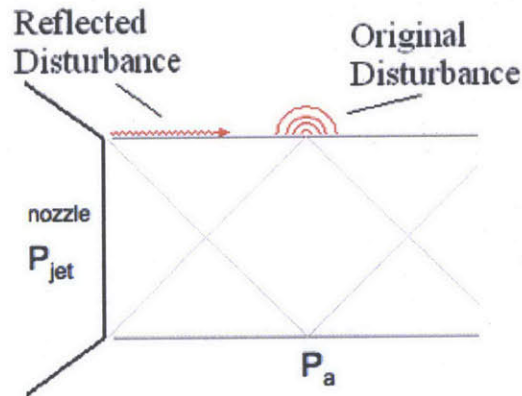


Figure 1.8: Schematic of the screech tone generation mechanism. This mechanism is common of free jets when run at off-design conditions. Shock cells generated in the jet as a result of running the jet at the under-expanded condition interact with the shear layer and produce disturbances. This disturbance travels upstream, reflects off of airframe surfaces and travels back downstream where it is amplified.

When operating off condition, some supersonic jets may produce an additional noise source known as “crackle”. Crackle is made up of intermittent, high-strength, ballistic shock waves, akin to Mach wave radiation. This noise source is found only in certain instances when the jet is operated at off-design conditions. Since the jet in this study was operated consistently at the ideally expanded condition, crackle was not present.

There have been several attempts to reduce the noise generated by a jet, though most come with large disadvantages. Many studies have focused on the use of chevrons and tabs. These consist of tabs of material that protrude from the nozzle into the jet exhaust. Bradbury and Khadem as well as Samimy, Zaman and Reeder showed that significant noise reduction could be achieved using tabs [15, 16]. However, this comes with one stark disadvantage: the tabs present themselves as a source of drag, thus producing an unacceptable amount of thrust loss. Also, tabs and chevrons cause an

energy shift in the frequency spectrum. While the noise generated at low frequencies is decreased, high-frequency noise is increased. Therefore, the reductions presented occur only in certain directions. Papamoschou developed a co-flow technique for supersonic jets similar to the high-bypass engines used on commercial, subsonic aircraft [17, 18]. While this was effective in reducing the overall noise, the inlet area required was too large to allow for its practical use. Raman, Kibens, Cain and Lepicovsky developed a technique involving a high-speed actuator [19]. The actuator would introduce tones into the exhaust to control the characteristics of the fluid flow. However, the reductions produced were marginal at best.

Much work has been done involving a new technique of jet noise suppression. Performed by Greska, this technique involves control by means of fluidic microjet injection [3]. Several small nozzles are positioned at the nozzle exit pointing into the flow. These nozzles may inject any medium, which penetrates the shear layer of the jet. This sets up streamwise vortices that inhibit the formation and growth of large-scale structures and eddies. This effect was shown by Alkisslar, Krothapalli and Butler [20]. This technique is able to achieve large noise reductions (up to 10 dB). Since the microjet nozzles themselves do not interfere with the flow of the main jet, no drag is produced.

Noise generation by aircraft exhaust flows on carrier decks specifically is a major problem since it poses a significant health hazard to on-deck personnel and can lead to damage to aircraft and carrier hardware. A standard approach to divert these flows is through the use of a jet blast deflector that is raised during run-up and takeoff. The presence of the raised deflector causes not only a redirection of the jet exhaust, but also increases the near-field, low-frequency noise generated by the aircraft exhaust. As shown in a recent report [21], the noise generated by aircraft on carrier decks has increased the health risks to on-board personnel. It has been reported that the number of military personnel tested routinely for hearing loss has increased significantly from 67,000 in 2001 to 157,000 in 2010, a major portion of which can be attributed to proximity to aircraft sorties. The F/A- 18E/F Super Hornet, for instance, has been shown to produce up to 150 dB of noise, which is well above the safe exposure limit of 84 dB. Even with advanced noise protection devices that can reduce noise by 50 dB, it has been found that safety

limits are often exceeded. Even more recently, the Naval Research Advisory Committee released a report identifying aircraft exhaust noise as a major problem requiring immediate attention [22]. While the ultimate goal is to develop a method of noise reduction for geometry resembling that of an actual aircraft carrier, the impinging jet setup, which has been studied extensively and has a broader application base, is the subject of this study.

Many engineering applications such as rocket launch and takeoff and landing of vertical takeoff and landing (VTOL)/short takeoff and vertical landing (STOVL) aircraft involve the use of impinging supersonic jets. These applications show striking similarities to free jets that strike, and are redirected by, jet blast deflectors found on aircraft carrier decks, as shown in Figure 1.9. Another advantage to impinging jets is their high heat transfer coefficient. This characteristic is taken advantage in applications such as paper drying, turbine blade cooling, and electronic equipment cooling. One disadvantage of these flows is that, under certain circumstances, they can become highly oscillatory – leading to structural and ground wear. Additionally, the high OASPL values associated with these jets can lead to sonic fatigue and wear of the aircraft structure, as well as contribute to noise pollution. It is therefore important to study the flow features of impinging jets in order to understand their responsibility for producing noise and for developing methods of noise suppression. New methods of suppression must be capable of attacking both the broadband noise as well as feedback tones.

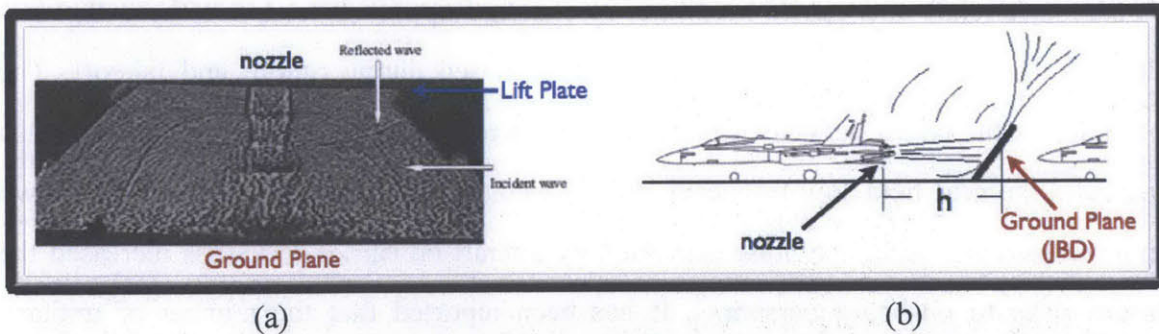


Figure 1.9: Schematic of (a) an impinging jet flow field and (b) the flow field of a carrier aircraft with a blast deflector. The anatomy of the flow field for each of these specific instances is similar in that there are downstream-propagating shock waves, which reflect and send acoustic waves back to the nozzle. The geometry also produces recirculation regions as a result of the global flow properties of the main jet.

Feedback loops, which generate strong spectral tones in impinging jet flows, are related to the interactions between the shear layer and solid layer boundary found primarily in edge tone and cavity flows [23]. This phenomenon has been studied extensively since in the work of Powell [24]. As discussed earlier, the feedback loop is the result of large-scale shear layer structures that propagate downstream from the nozzle exit. These structures collide with the ground plane and their acoustic waves propagate back upstream where they meet with aircraft geometry. The return of the wave completes the loop and a resonance phenomenon is created. At higher Mach numbers, Ho and Nossier [25] have demonstrated how upstream traveling waves may interact with the smaller-scale, higher-frequency structures present near the nozzle exit (where the shear layer is very thin). The overall flow structure of impinging jets have been studied extensively by a number of studies including by Powell [17], Donaldson and Snedeker [26], Lamont and Hung [27], Tam and Ahuja [28], Messersmith [29], Alvi and Iyer [30], Krothapalli [31] and recently by Henderson [32]. These studies show that the flow field of the impinging jet is comprised heavily of distinct impingement tones and is overall highly unstable. The generation of large-scale structures was shown by Krothapalli to induce high entrainment velocity near the nozzle exit. During hover, this results in a measurable lift loss for the aircraft. Lepicovsky and Brown [33] showed that the relationship between heating a jet and the aircraft's susceptibility to these excitations was that the raised temperature decreased the nozzle Reynolds number. For these Mach 0.8 jets, the flow was relaminarized at the higher temperatures, and it became less sensitive to induced excitations. This study also concluded that the downstream centerline velocities were also higher when the shear layer was thickened through heating. This was due to the reduction of jet mixing. Many attempts have been made to suppress the feedback loop inherent in impinging jets. These attempts have involved both passive and active methods. By fixing two parallel plates perpendicular to the jet centerline, Karamcheti [34] was able to suppress edge tones. Kweon [35] reduced screech tones and broadband shock associated noise by placing two wires perpendicular to the jet centerline axis. The feedback loop was attenuated by Elavarsan [36] using a circular plate near the nozzle exit. A reduction in the near field OASPL and a reduction in lift loss were also demonstrated. Using high-speed co-flow, Sheplak and Spina [37] were able to shield the

primary jet from the ambient environment. Shih [38] was able to suppress screech tones of jets operating off-design using counter-flow techniques at the nozzle exit. These techniques have shown reductions in noise levels, but require extreme aircraft geometry modifications and are limited to specific operating conditions.

Recently, an approach to suppress the feedback mechanism of the supersonic impinging jet has been developed and implemented at the nozzle exit. This method consists of using high-momentum microjets, and has shown encouraging results [39-42]. This technique, which produces reduction of noise without sacrificing thrust (as do previous passive and active control techniques), has been shown to be effective over a wide range of operating conditions and geometric considerations. Lou [40] performed several PIV measurements and found that microjets are effective in the same way chevrons are: by producing streamwise vorticity, which acts to inhibit the growth of large-scale turbulent structures within the shear layer. It was found that these microjets produce reductions in initial shear layer instability, shear layer turbulence, and weakening of reflected acoustic waves. In accomplishing these three things, microjets effectively break the feedback loop. Alkisar, [20] more recently, published a comprehensive paper on both microjets and chevrons and their effect on the free jet flow field of a high subsonic jet ($M=0.9$). Both microjets and chevrons were shown in this study to produce counter-rotating streamwise vortex pairs at each of the injection/protrusion points. However the difference between the two being that microjets do not produce a thrust loss or require modifications to the nozzle geometry. It should be noted that these past experiments were only performed on cold jets. For the sake of implementation and practicality, it is necessary to quantify the effects of microjets on heated jets. Previous studies have shown that there exists variation in the strength of impingement tones relative to the broadband noise at stagnation temperatures ranging from 300-500 K [43]. Full-scale tests found no distinct tonal peaks in the spectra [44]. This brings into question whether temperature or geometry is the controlling factor regarding peak strength and frequency. In this study, the geometry is held fixed and the temperature is varied. This allows for the effect of jet exhaust temperature on the features of the flow field and noise spectrum to be isolated.

While most of the previous work using microjets for noise suppression has

employed air or nitrogen as the working fluid in the microjets, several studies have been performed on utilizing the greater density of water to more effectively penetrate and affect the development of a high-speed jet. Water jets have previously been used for noise suppression in free jets, as demonstrated by Zoppelari & Juve [45], Krothapalli et al. [4], Greska & Krothapalli [46], Norum [47] and Kandula [2].

The early work using water as the working fluid focused on injection into a free jet close to the nozzle. Kandula has found that OASPL reductions as large as 8-12 dB can be achieved when using very large water-to-main jet mass flow ratios of the order unity [2]. In this case, both turbulent mixing noise and shock-associated broadband noise were suppressed. The focus in the present work is on the impact of water microjets implemented at the ground plane. Krothapalli et al. [4] found a reduction of near-field OASPL levels of 2-6 dB using only 5-10% of the main jet flow, but given the strong tonal reductions found in an impinging jet case using air injection at even smaller flow rates, as in Kumar [43], greater suppression is expected using water injection in this case owing to the increased density of water. An interesting parameter to study is the optimum injection angle when injecting from the ground plane. For injection from the nozzle, Zoppellari & Juve [45] and Norum [47] indicate that an optimum angle is 45-60° to the jet axis. When injecting from the ground plane, the impact noise between water and main jet must be taken into account along with the interaction between the wall jet and the water jets; at too high injection velocity radially into the jet, Kandula has shown that the generated parasitic noise may become significant [2].

Much of the previous work concerned with the identification of noise suppression mechanisms deals with free and impinging jets whose control technique is applied at the nozzle exit. Hsiang and Faeth [48], in a comprehensive work, characterized the breakup of fluid droplets in a second fluid medium. In knowing both the Weber (We) and Ohnesorge (Oh) numbers of one fluid with respect to the containing fluid, one could determine in which regime the droplet was breaking up. The Ohnesorge and Weber numbers are given by

$$Oh = \frac{\mu_l}{\sqrt{\rho_o d_o \sigma}}$$

$$We = \frac{\rho_g d_o u_o^2}{\sigma}$$

Figure 1.10 shows the summarized results of this study, as reproduced from their publication in the Journal of Multiphase Flow. Krothapalli et al. [4] demonstrated that, in their experiments, the fluid microjets used in their study involved droplet breakup in the shear regime. This was mostly attributed to the high velocities associated with the flow in their setup. Greska [3] demonstrated, through the use of low-pressure water microjets mounted at the nozzle exit of a free jet, that the breakup of the water droplets could be responsible for the reduction in low-frequency broadband noise. In the same study it was determined that higher-pressure microjets could reach the high-speed side of the shear layer and reduce the high frequency, shock associated noise. This noise is a result of the growth of large-scale structures within the shear layer, and which favor the high-speed side of the shear layer [20].

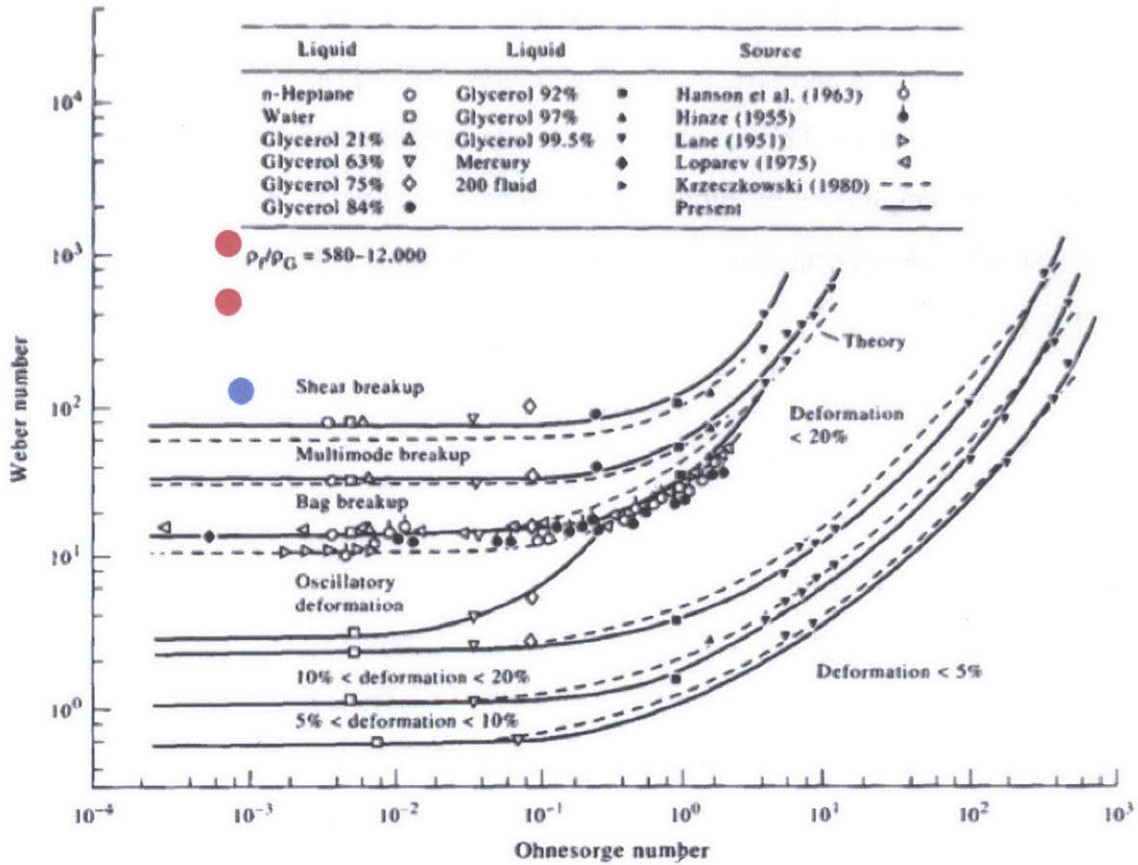


Figure 1.10: Droplet breakup regimes as a function of Ohnesorge and Weber numbers as reproduced from Hsiang and Faeth [48]. At Ohnesorge numbers less than one, the droplet breakup regime is influenced only by the magnitude of the Weber number. The flow condition in Krothapalli et al [4] is represented by the blue dot, and the range of conditions in this study is represented by the red dots.

The primary objective of the present study is to test water microjet injection from the ground plane for suppressing noise generated by an impinging jet. The motivation is that this will allow a suppression system to reside on the ground, rather than on the aircraft or rocket, allowing a much more robust system to be employed. Greska [3] showed that the use of water microjets was much more effective than air due to its higher momentum, and the use of water could prove beneficial from a practicality standpoint in that they it could also be used to actively cool the blast deflector. An ideally expanded Mach 1.5 jet was heated up to a total temperature of up to 1033K through ethylene combustion and was issued from a converging-diverging nozzle. The jet was allowed to impinge on a ground plane that could be moved to cover a range of nozzle-ground

distances. Pressure measurements were made on the ground plane over a range of nozzle-ground plane distances and stagnation temperatures. Far-field noise measurements were made using microphones. This extends the data set available in the open literature on tonal frequencies and amplitudes of impinging jets to higher temperatures. This work is also concerned with identifying and relating the fluid-mechanical mechanisms that produce reductions in noise.

CHAPTER 2

EXPERIMENTAL SETUP

2.1 Overview

This investigation involves a set of experiments that required a high-temperature, high-pressure, supersonic jet facility. Therefore, they were carried out at the High Temperature Supersonic Jet Facility, which is located at the Fluid Mechanics Research Laboratory on the Florida State University main campus. The facility consists of three adjacent rooms and a high-pressure air supply. The air supply enters the first of the three rooms, dubbed the burner room, where it is reduced to a desired pressure. The air then enters a sudden expansion (SUE) burner where combustion occurs. The high-pressure, high-temperature airflow is then exhausted to the second room—a fully anechoic chamber—where it interacts with the ambient environment then exits to the atmosphere via an acoustically treated exhaust duct. Acoustic and ambient measurements are made in the anechoic chamber. All of the jet parameters are controlled and monitored from the third room—the control room. An overall schematic of the facility is shown in Figure 2.1.1. While a brief description of the facility is presented here, a more in-depth discussion can be found in Greska.

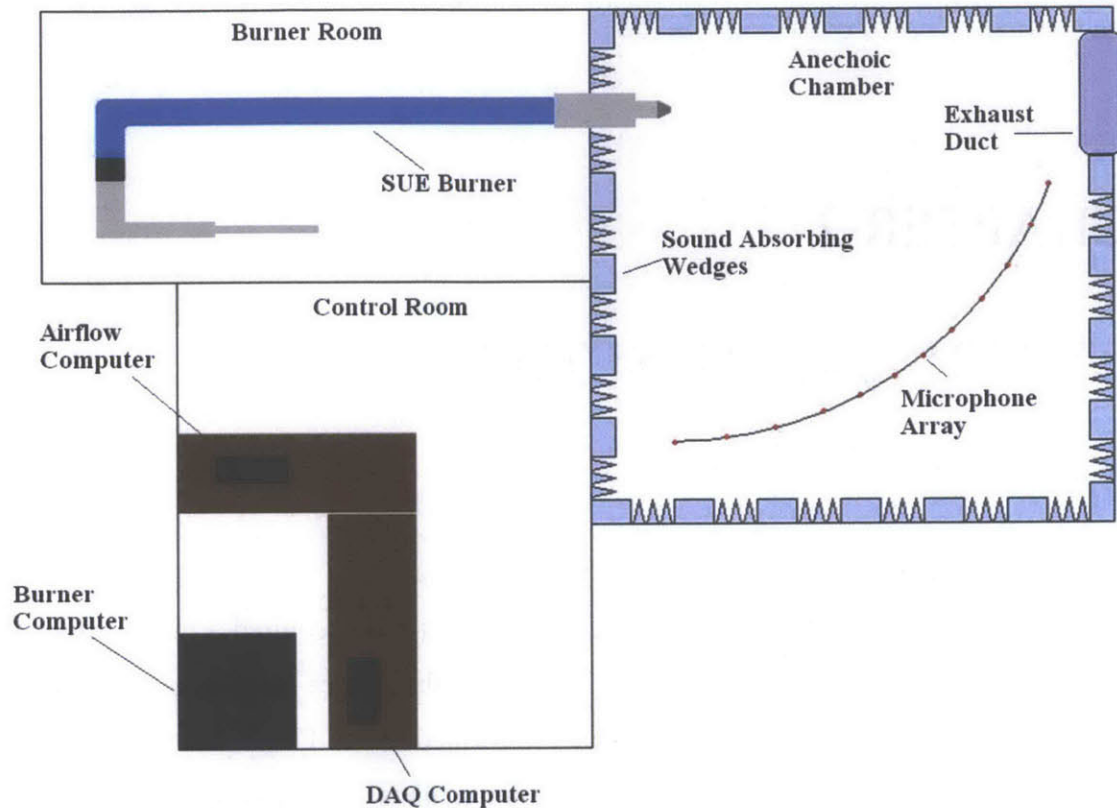


Figure 2.1.1: Simple schematic of the high-temperature, supersonic jet facility. High-pressure air enters the Burner Room, is mixed with ethylene and is combusted. The high-temperature, high-speed exhaust is directed into the Anechoic Chamber through a specially designed nozzle. The jet operating parameters are controlled, and measurements are obtained, in the control room.

2.2 High Pressure Air Supply

Air is pressurized by means of a CompAir MAKO model 5436-60E3, four-stage, high-displacement, reciprocating air compressor. This compressor has an output of 80 CFM. The local air in Tallahassee, Florida tends to be very humid, and any moisture in the air will condense within the facility, so the compressed air is then dried using a Zander model HPRDF200-W refrigerated air dryer. Oil and particulates from the atmosphere and compressor are removed by a series of filters through which the compressed air passes after leaving the refrigerators. These particulates, if not removed, would decrease the performance of the pressure regulating equipment within the facility.

The pressurized and cleaned air is then stored in a series of four interconnected storage tanks. The first of which has a volume of 5 m^3 , while the remaining three (which are identical) have a combined volume of 5 m^3 giving a total storage capacity of 10 m^3 .

Air in the tanks is pressurized to 2000 psig, and the experiments can be run until the pressure is depleted to about 500 psig. This capacity allows for a run time between 20 and 45 minutes, depending on the jet operating conditions. It takes about eight hours for the pressure in the tanks to be fully replenished. Figure 2.2.1 shows a schematic of the high-pressure air supply system.

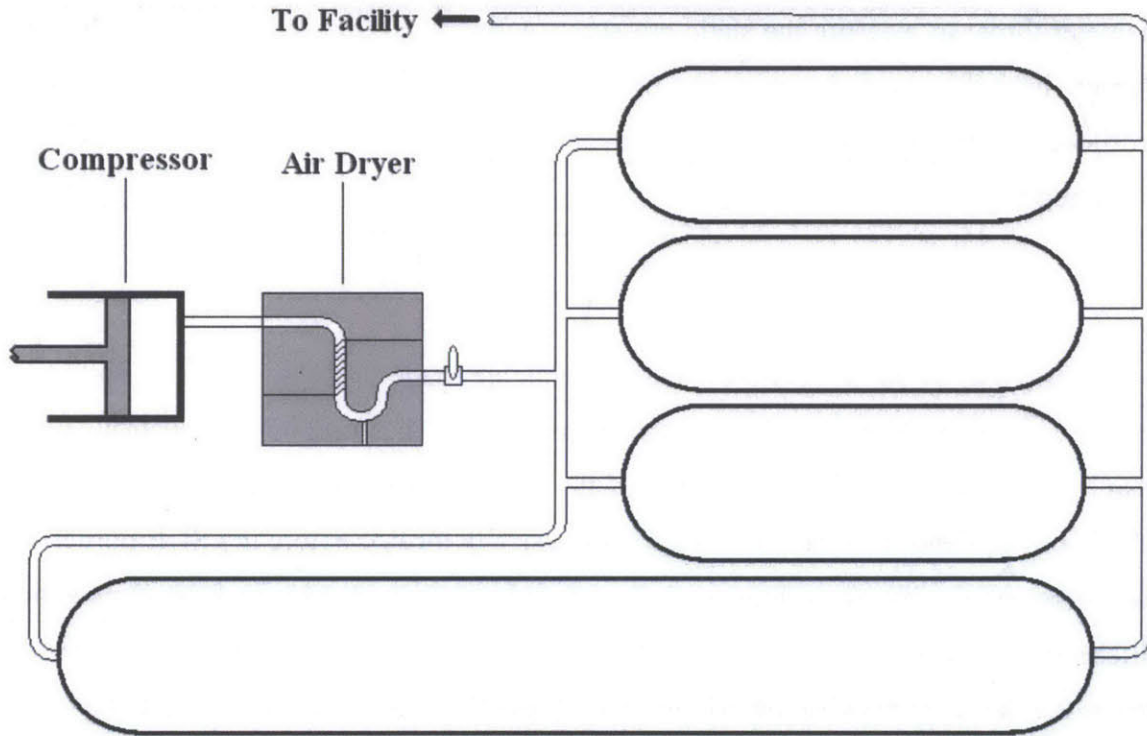


Figure 2.2.1: Simple schematic of the air supply system. Air was compressed to high pressure using the reciprocating compressor, dried to reduce the naturally high humidity, then stored in the three parallel storage tanks.

2.3 Burner Room

The high-pressure air is routed into the burner room via a network of 1.25-inch schedule 160 piping. In the burner room, the air first passes through a Jamesbury model SP200-B double-acting solenoid shut-off valve. It then passes through a 2.5-inch schedule 80 pipe on its way to the two-stage pressure control system. This consists of two 2-inch Leslie Aeroflow high-performance control valves. The first valve is designed to have a large pressure drop so that the pressure can be reduced from supply to 300 psig if necessary. The second valve has a low-pressure drop, and is used mainly for fine adjustments to the pressure. After each of the valves, for safety reasons, a Hydroseal

relief valve is implemented. The upstream relief valve is set to 1100 psig while the downstream relief valve is set to 300 psig.

To ensure that the flow does not reach sonic condition where the air mass flow measurements are made, especially when nozzles with larger throat diameters are used, a new Venturi was designed and installed. The former Venturi employed a 1.2-inch diameter throat to measure the static pressure. A flat plate surrounding the mouth of the Venturi held the stagnation pressure probe. The new Venturi features a super-ellipse profile that keeps the flow from separating as it enters the test section. This super-ellipse is defined by:

$$h(x) = b\sqrt{1 - \left(\frac{a-x}{a}\right)^{2+(x/a)^2}}.$$

Both static and dynamic pressure measurements are made in the same plane within the test section of the Venturi. This section has an inside diameter of 2.25 inches—larger than the largest throat diameter of any of the jet nozzles used. Figure 2.3.1 shows the profile of the Venturi. Since the venturi is physically located before the SUE burner, we can guarantee that the flow does not become sonic therein. A mirror of the same super-ellipse is used to blend the measurement section into a 6° sloped section. This section brings the diameter back to the original pipe diameter. The total length of the Venturi is eight inches.

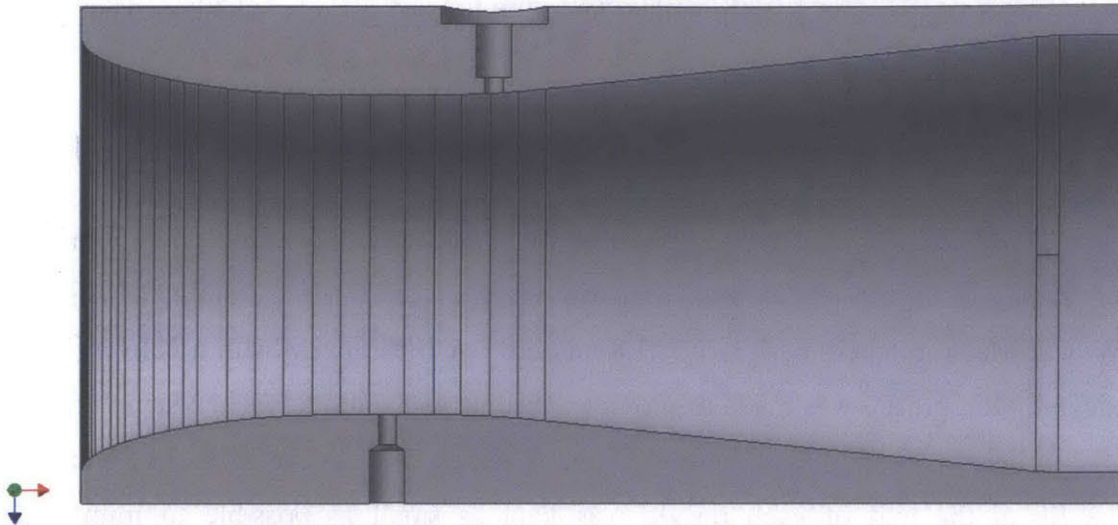


Figure 2.3.1: Cross section of the Venturi. Holes are drilled for the static and dynamic pressure taps. A super-ellipse profile is used to keep the flow from separating as it enters the measurement section. It is blended on the downstream side to a 6° sloped section.

The pressurized air then enters the SUE burner. While most hot jet facilities use electric heaters, those that use combustion burn propane (which tends to limit the maximum stagnation temperature to 1100 K). This facility uses ethylene as the fuel; its combustion can produce flows with stagnation temperatures up to 1700 K, and enables run conditions that simulate realistic jet conditions. A standard automotive spark plug is used to initially ignite the ethylene, which is fed in initially through a single tube. Six tubes inject gaseous ethylene fuel (which is fed from eight bottles in a closed, outward-facing compartment of the burner room) into the stagnation region of the expansion, thus guaranteeing a rich fuel/air mixture. The combustion of this mixture produces a high-temperature, high-pressure flow. After passing through a 1-inch thick ceramic flow straightener, the flow passes through a section where temperature and pressure are measured. Four equally spaced holes are drilled radially in this section, and an extrusion on each hole allows for the use of $\frac{1}{4}$ -inch male NPT fittings. Into two opposing holes are inserted C-type thermocouples that measure the temperature of the flow. The stagnation pressure is measured via the other two holes. Since the flow is relatively slow in this section, the stagnation and static pressures are nearly equal. The flow then travels through another straight section, then a reducing section, then finally through an adapter. The nozzles are attached directly to this adapter. Each section is attached to the previous

section with flanges and custom made Flexitallic Inconel gaskets, which prevent leaks at the joints.

2.4 Nozzles

Five nozzles were fabricated to allow for different operating conditions. Four converging-diverging (C-D), axisymmetric nozzles were made to allow for supersonic flows at Mach numbers of 1.3, 1.5, 1.8 and 2.0. A fifth nozzle with a converging (C), axisymmetric profile was made to provide subsonic and sonic flows at Mach numbers of 1.0 and below. Examples of both C-D and C nozzle profiles are given in Figure 2.4.1. The lip at the exit of each nozzle was kept as small as possible to minimize jet screeching. Larger lips allow for disturbances, which are reflected by large-scale structures, to reflect and amplify into tones. This enhances the overall broadband noise. While microjets easily quell this feedback loop, the baseline conditions without microjets will produce more noise, which will cause inaccurate baseline measurements. The lip of each nozzle was kept less than 1 mm. All of the experiments contained within this thesis, unless specifically stated, were performed using the Mach 1.5 nozzle at the ideally expanded operating condition.

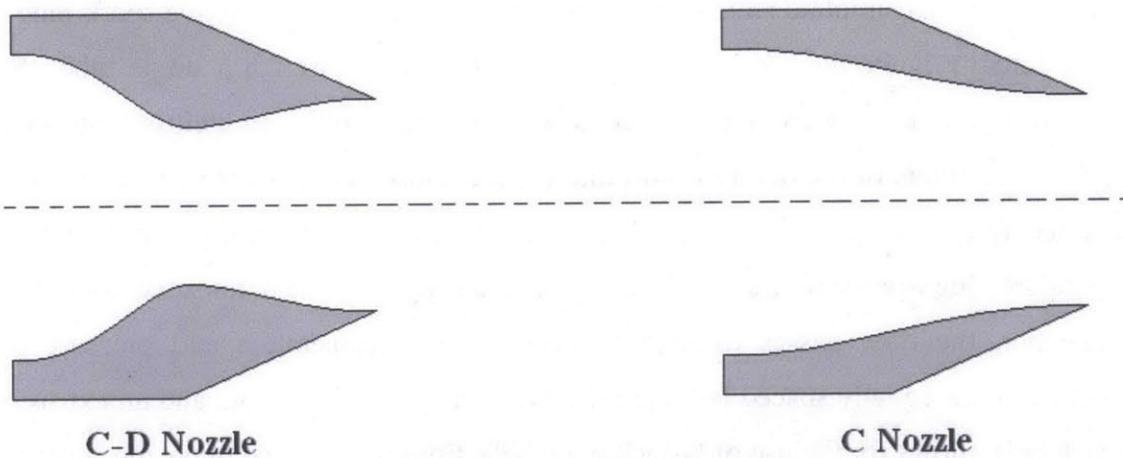


Figure 2.4.1: Nozzle types. On the left is a converging-diverging (C-D) nozzle used for supersonic flow generation. On the right is a converging (C) nozzle used for subsonic and sonic flow.

2.5 Microjet Injection

Nitrogen is used to pressurize the microjets. Three nitrogen tanks are used as the high-pressure store, and they feed into a dome regulator. This dome regulator, a Tescom model 26-1121-262, is located in the burner room with the tanks and controlled from the control room. This allows the pressure to be set and changed from a remote location so that no one has to enter the burner room while experiments are in progress.

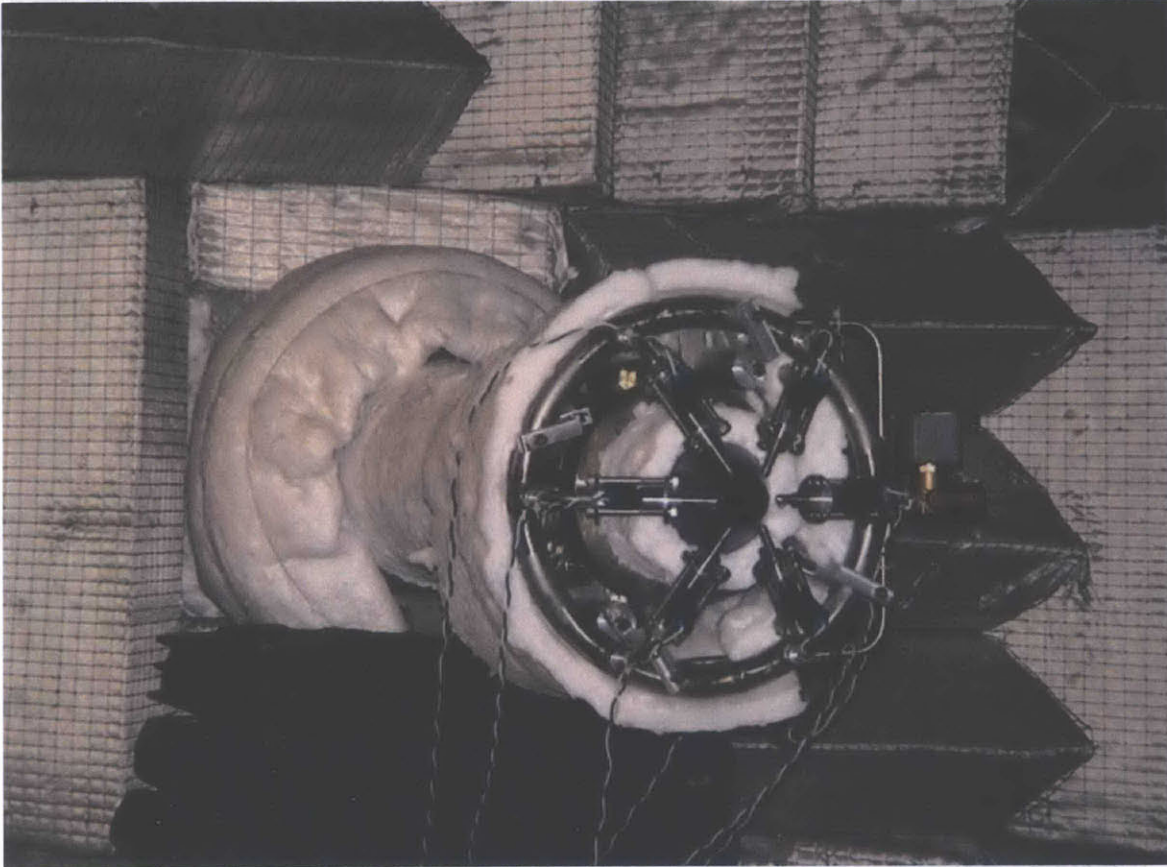


Figure 2.5.1: Microjet injection at the nozzle exit. Six injectors are mounted around the nozzle and are fed from the toroidal manifold to ensure that each microjet injects water at the same pressure.

The microjets can be run with either water or nitrogen as the injection medium. When nitrogen is used, the supply gas is passed through 3/8-inch stainless steel tubing to a Brooks model 3853i flow meter located in the burner room. The same tubing then takes the gas into the anechoic chamber where it reaches a toroidal manifold. The pressure of the fluid is monitored in the manifold via four pressure taps that are evenly spaced around the backside of the ring. Six 3/8-inch Swagelok fittings were fish-

mouthed and welded to the front side of the ring manifold at evenly spaced locations. Six feeder tubes connect the microjets to the manifold and hold them at an angle of 60° to the jet axis. Figure 2.5.1 shows the microjets mounted on the manifold around the nozzle. When water is used, a separate tank is employed. Air at the desired pressure enters the tank and forces the water up a long tube that extends down to the bottom of the tank. The water travels through the same 3/8-inch tubing out to the circular manifold. When water is injected the flow meter is not used as it is calibrated with nitrogen as the working fluid. Water flow rates are determined experimentally with an individual microjet. A schematic of the injection system is shown in Figure 2.5.2.

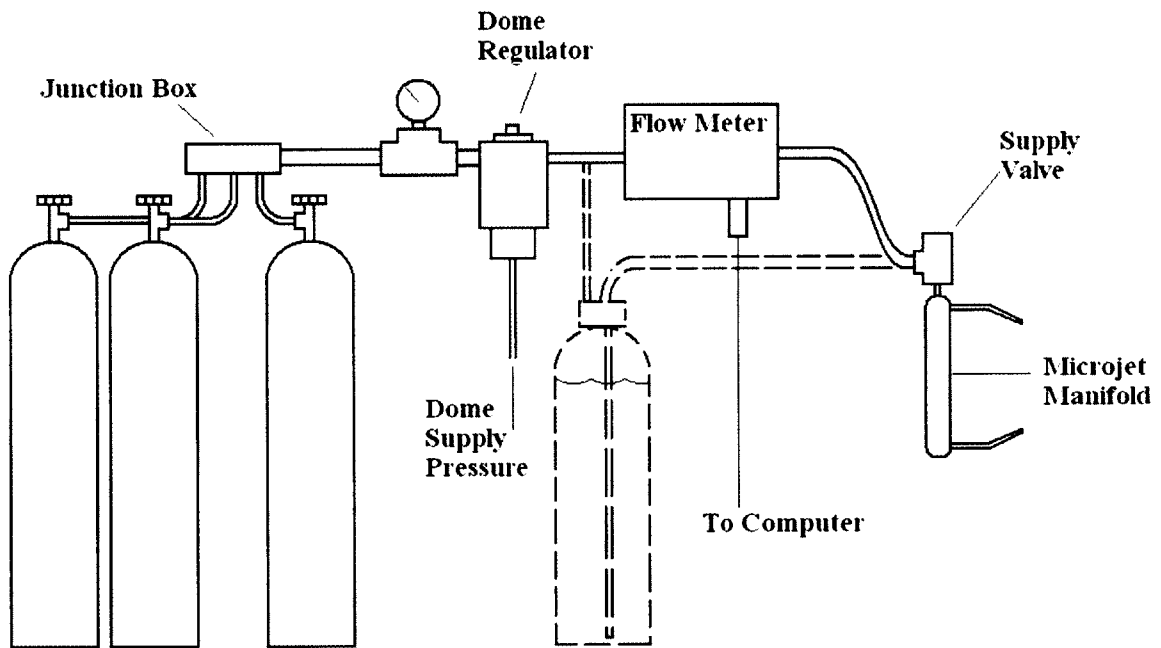


Figure 2.5.2: Simple schematic of the microjet injection system. Three nitrogen bottles provide the backpressure for the microjets. When using water injection, the nitrogen is used to pressurize a water tank, forcing pressurized water out of the tank to the manifold. This path is shown by the dashed lines.

2.6 Anechoic Chamber

The nozzle itself is located in a fully anechoic chamber and the jet exhausts there. The chamber measures 5.2 m wide, 5.8 m long and 4.0 m high. On the opposing wall to the nozzle is an acoustically treated exhaust duct that routs the flow up to the roof of the facility. In order to minimize acoustic reflection, the walls, ceiling, floor and door are all fully covered with sound-absorbing wedges. Each wedge panel houses three wedges that

measure 304.5 mm high, 609.6 mm long and 203.2 m wide. These wedges are rated to absorb frequencies above 300 Hz. The side of the chamber behind the microphone array has grating installed so that key features of the chamber are easily accessible. However, the grating closest to the jet is covered with wedge panels to inhibit acoustic reflection. The room is ventilated so that the jet properly entrains ambient air. Therefore, the temperature in the room never rises above 320 K for the jet conditions described in this thesis. The ambient pressure, temperature and relative humidity of the chamber are monitored in strategic locations from the control room.

2.7 Control Room

In the control room three Windows-based PCs control the operation of the jet. One PC controls the airflow, and another controls the burner. The third acquires the acoustic measurements. All three computers run LabVIEW graphical user interface (GUI) programs. For baseline and pulsed measurements, the data acquisition (DAQ) computer collects three seconds of data. For transient tests, it collects seven seconds with the microjets turning on and off three times at a frequency of 0.5 Hz and 50% duty cycle. It also records the start, stop, and microjet on/off times for analysis purposes. At the start of data collection, a signal is sent to the burner computer so that each run can be matched with its corresponding ambient conditions.

2.8 Ground Plane Test Stand

Traditionally, STOVL facilities mimic the actual geometry involved in such aircraft applications. That is to say the main exhaust jet points downward toward the ground, and a moveable plate, able to traverse upwards and downwards, simulates the relationship between the stationary ground and the aircraft as it approaches or departs. The main advantage to performing the experiments in the High Temperature, Supersonic Jet Facility was the ability to reach temperatures and exit velocities similar to those found in real aircraft. Therefore, in creating an impinging jet setup, no significant changes were made to the existing setup. Rather, a full impinging jet stand was designed and built. This stand housed a $\frac{1}{4}$ inch, stainless steel impingement plane. All of the required

transducers and noise suppression apparatuses were housed on this plane. A schematic of the overall impingement plane setup is shown in Figure 2.8.1.

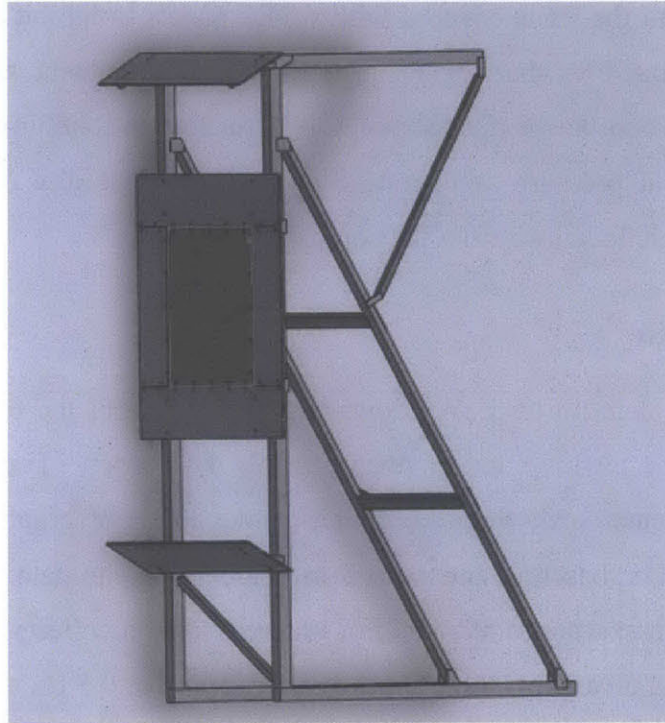


Figure 2.8.1: Schematic of the ground plane. The structure is designed using aluminum members, and the ground plane is constructed from $\frac{1}{4}$ inch stainless steel plate. This material was chosen due to its durability at the high temperatures at which the jet would operate.

The entire impingement plane setup is mounted on rails using linear bearings. This allowed for various h/d settings to be tested. A linear positioner mounted to the bottom of the test stand allows for the real-time positioning of the setup. The position of the ground plane may be modified mid-experiment, allowing for the simulation of in-situ takeoff conditions.

The facility was originally designed and optimized to perform free jet experiments. In modifying the facility to perform impinging jet experiments, care had to be taken to ensure that the flow was properly directed through the chamber towards the exhaust vent at the back. Originally, simple entrainment of the main jet would ensure that the high-temperature exhaust would exit through the vent and through the room. However, with the addition of the moveable ground plane, no such entrainment could

take place. Therefore, flow deflectors were added to guide the wall jet backwards, away from the chamber walls, and toward the vent. This ensured that the ambient temperature of the chamber would not rise above the safe operating temperature of the more sensitive equipment housed within. A schematic of the moveable ground plane with its flow deflectors in the chamber is shown in Figure 2.8.2. The nozzle is shown to the left of the figure and is covered in fiberglass insulation. The exhaust vent is shown at the right.

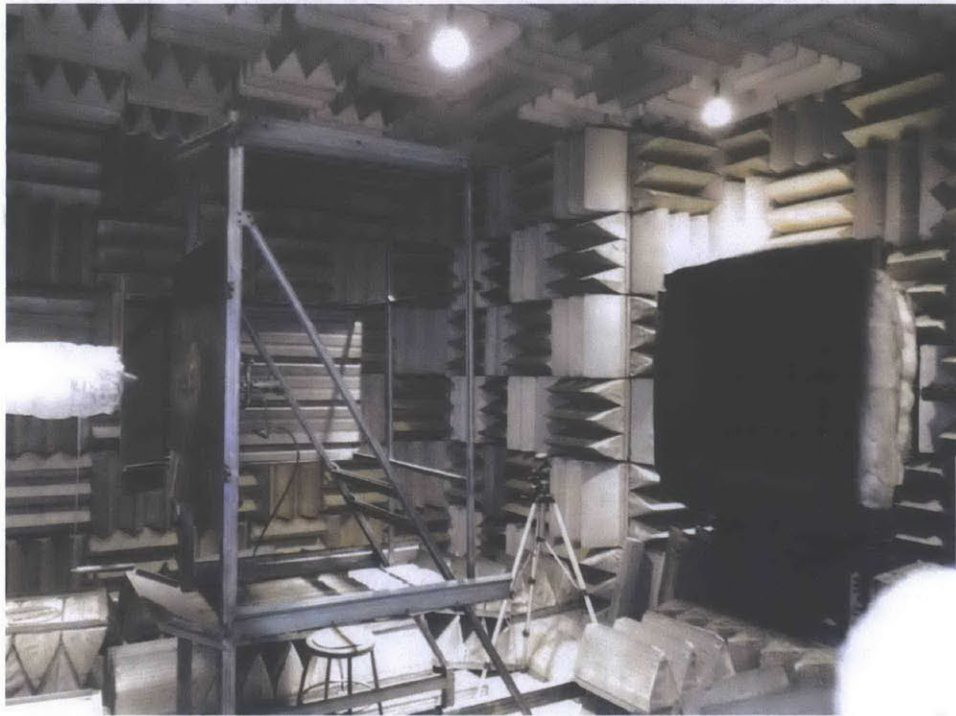


Figure 2.8.2: Depiction of the anechoic chamber with the moveable impingement plane. Ground plane transducers and microjets were installed behind the plane. A removable center section allowed for the installation and use of both pressure and temperature transducers and microjets.

When performing ground plane microjet injection, a special manifold and leader system was used. First, a custom center section was machined for installation into the ground plane. Into this center section were drilled eight $\frac{1}{4}$ inch countersunk mounting holes as well as six angled holes into which the microjet tubing was installed. The tubing used was $\frac{1}{16}$ inch stainless steel tubing with an inner diameter of 0.044 inches. This tubing was selected specifically for its ability to hold up to the high pressures and temperatures to which it would be exposed. These tubes were welded in place and then ground flush with the front of the plate. Using standard compression fittings, the tubes

were joined to the $\frac{1}{4}$ inch stainless steel riser tubes. These risers were then attached to the toroidal supply manifold. The manifold was machined from $\frac{3}{4}$ inch stainless steel tubing, and fittings were fish mouthed and welded on. As mentioned earlier, the manifold was fed from the high-pressure supply located in the burner room. The manifold was supported using aluminum clamps. This ensured that the delicate microjet tubing would not be damaged due to movements as a result of the pressurization or weight of the manifold. The microjet supply from the backside of the center section is shown in Figure 2.8.3.

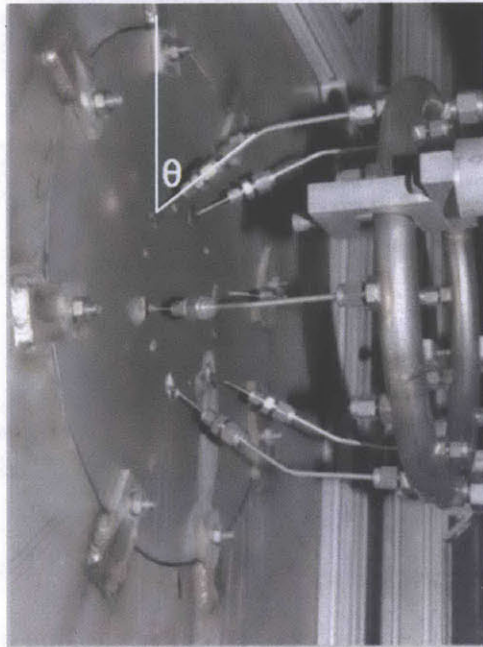


Figure 2.8.3: Photograph of the back side of the ground plane with toroidal microjet supply manifold and microjet supply tubing. Specialty tubing was used to construct the microjets, which were welded in place. One-quarter inch stainless steel riser tubing was used, in conjunction with standard compression fittings, to connect the microjets to the supply manifold. The injection angle of the microjet is shown by the Greek letter θ .

Much care was taken to ensure that the microjets were firing properly before each experiment run. Filtered water was used in order to minimize the amount of solid particulates introduced into the injection system. Regardless, the micro nozzles were cleaned before each run and tested to ensure proper function. The microjet flow and angle were also carefully checked. As shown in Figure 2.8.4, when operating properly, the microjets converge on a single point a prescribed distance upstream of the injection

plate. This convergence point is located on the jet centerline. It should be noted that Figure 2.8.4 shows the microjets operating at low pressure. The purpose of this photograph was to demonstrate how alignment and operation was determined. During actual tests, the microjets were operated at much higher water injection pressures.

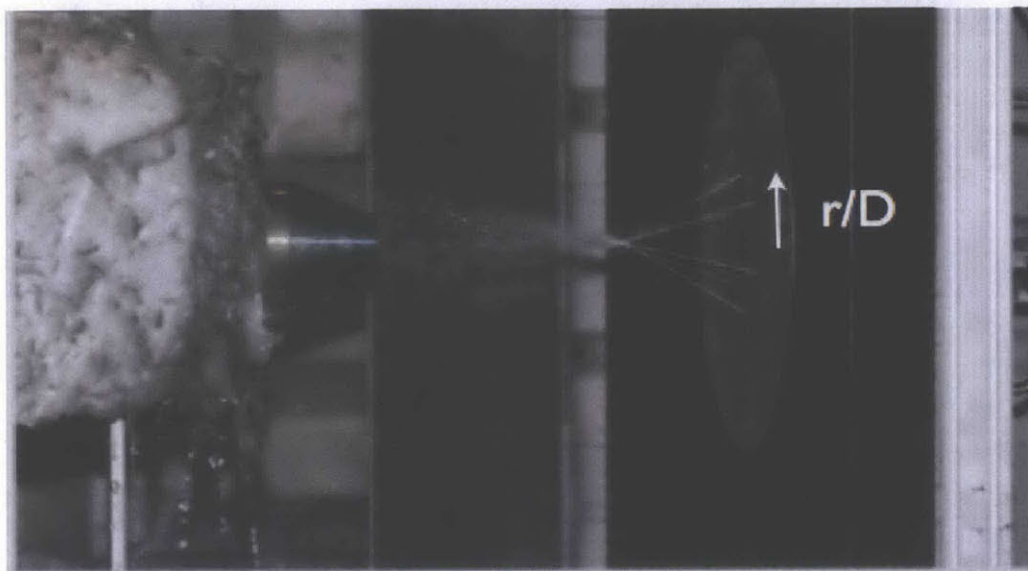


Figure 2.8.4: Photograph of the front of the ground plane showing the detachable microjet center structure during the firing of the microjets. In this photograph the microjets were being fired at low pressure in order to check their alignment. Great care was taken to assure that the microjets were operating properly before each test, and that all six microjets converged at the correct point. The radial direction, r/D , is indicated on the figure.

2.9 Ground Plane Temperature and Pressure Measurement

Measuring pressure and temperature fluctuations at the ground plane present a specific challenge in that the area of interest is exposed to high-temperature flows with large pressure fluctuations. This environment makes the use of ordinary temperature and pressure sensors impossible, as the operating conditions exceed their recommended settings. Therefore, special care was taken to choose sensors that, with proper care and design forethought, could withstand such conditions. This is especially true of the pressure transducers. In order to measure the pressure fluctuations on the ground plane, Kulite water-cooled WCT-312 transducers were used. A picture of such a transducer is shown in Figure 2.9.1. These sensors include a $\frac{1}{4}$ inch threaded plug for ease of installation and a water-cooled body jacket. Using 35 psig water at a 0.15 gal/min flow rate, these sensors can operate at ambient temperatures up to 2000°F. These transducers

used an independent water-cooling loop with a flow rate of 0.15 gal/min through each transducer. In order to measure temperature fluctuations on the surface of the ground plane, K-type, exposed-tip thermocouples were employed. Such a thermocouple is shown in Figure 2.9.2.

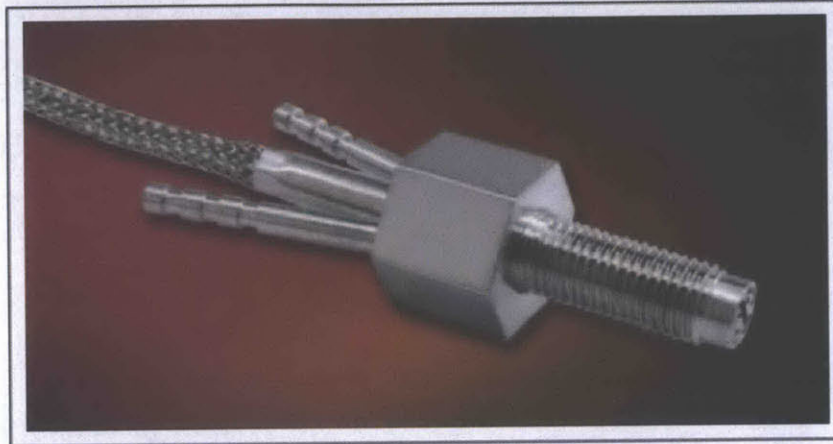
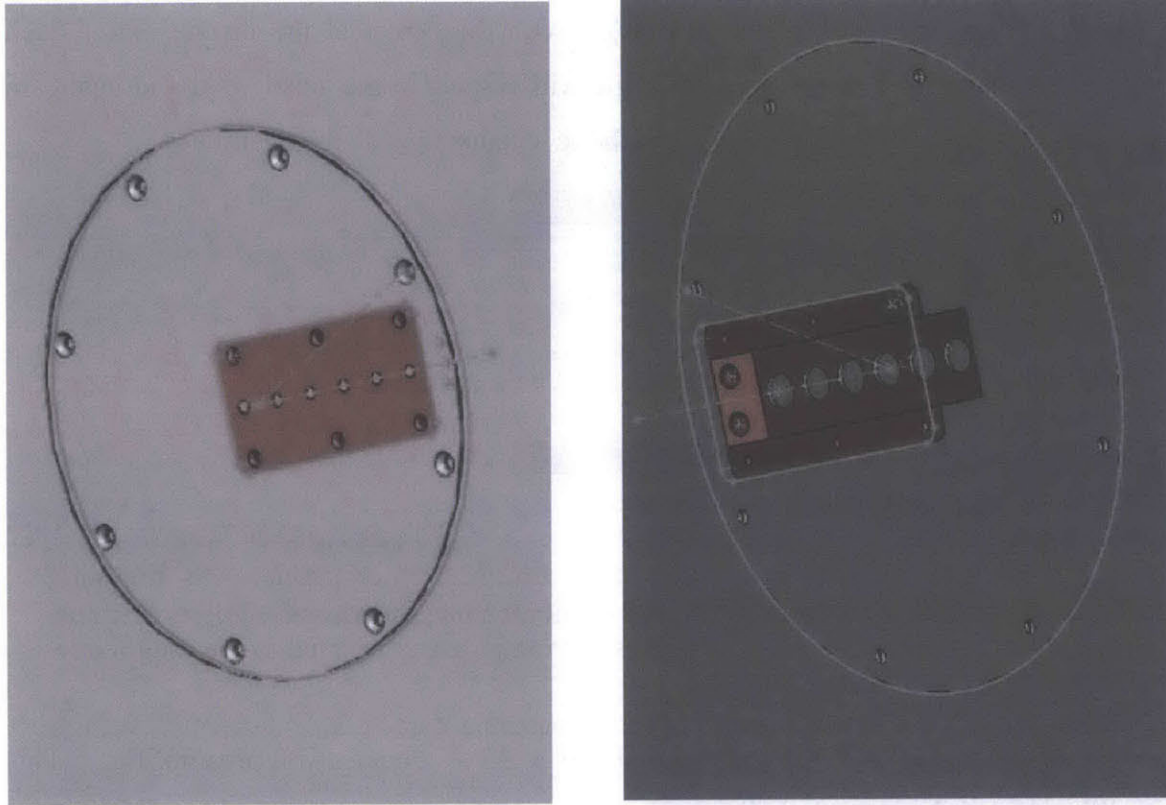


Figure 2.9.1: Photograph of the Kulite WCT-312 water-cooled pressure transducer. The body of each of these special transducers contains a water-cooling loop. Providing water at the required flow rate ensures that the transducer will be able to operate at the high temperatures generated by the main jet.



Figure 2.9.2: Photograph of a typical K-type thermocouple probe. This particular probe shows a grounded style tip. The type of thermocouple used in these experiments was the exposed tip thermocouple type, allowing for faster response.

The Kulite pressure transducers were mounted in a custom-designed, copper, mounting block. This block was designed to fit into a specially designed stainless steel center ground plane piece. Six threaded holes allowed the transducers to be mounted in the copper block, while sitting flush with the surface of the front side of the block. As an added precaution, the copper block was cooled through the use of an independent water loop. A schematic of the copper mounting block is shown in Figure 2.9.3. To mount the thermocouples, threaded copper plugs were created. These plugs tightly held the thermocouples in place while filling the space occupied by the Kulite.



(a)

(b)

Figure 2.9.3: Schematic of the (a) front side and (b) back side of the custom designed, water-cooled Kulite and thermocouple housing block. The copper block allowed for six transducers to be mounted with one at the jet stagnation point and five others radially outward at one inch increments. The block was water-cooled using a freestanding water circulation loop.

2.10 Acoustic Measurement

The microphone array allows for up to twelve microphones to be installed. Data are collected from each of the utilized microphones simultaneously. Twelve Brüel & Kjær (B&K) model 4939 ¼-inch condenser microphones are available to acquire all of the acoustic data. In this thesis data were acquired from a configuration of 2, 3 or 12 microphones, depending on the type of experiment being performed. Figure 2.10.1 is a schematic of a simple condenser microphone. The microphone basically consists of two parallel plates, like a capacitor, though one plate is mounted while the exposed plate is free to move on a membrane. A voltage is supplied to the movable plate and the voltage on the stationary plate is measured. This change in voltage corresponds to a specific pressure, based on the microphone's sensitivity. The microphones sit in a 3.048 m

circular array in the same plane as the jet, with the center at the nozzle exit. Each microphone is referred to by its radial angle with respect to the nozzle exit and upstream direction. Figure 2.10.2 shows the microphone locations inside the chamber.

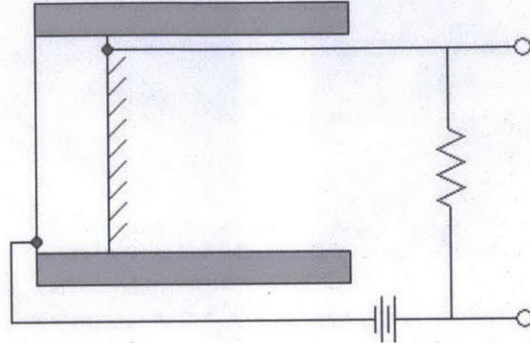


Figure 2.10.1: Simple schematic of a condenser microphone. As pressure fluctuations move the front plate of the microphone, the voltage drop across the series resistor changes. These changes in voltage are correlated to the magnitude of the pressure fluctuation.

Each microphone connects directly to a B&K model 2670 preamplifier. This amplifier has a 2 m cord that terminates at a 7-pin male LEMO connector. Four microphone/preamplifier pairs connect directly into a B&K Nexus 2960 conditioning amplifier; three conditioning amplifiers are used in all to handle all twelve microphones. The microphone sensitivity and polarity is programmed, through the menus on the front screen, directly into the conditioning amplifiers. The acoustic measurements are also low-pass filtered by the conditioning amplifiers with a cutoff frequency of 100 kHz, which is the upper limit of the microphone bandwidth.

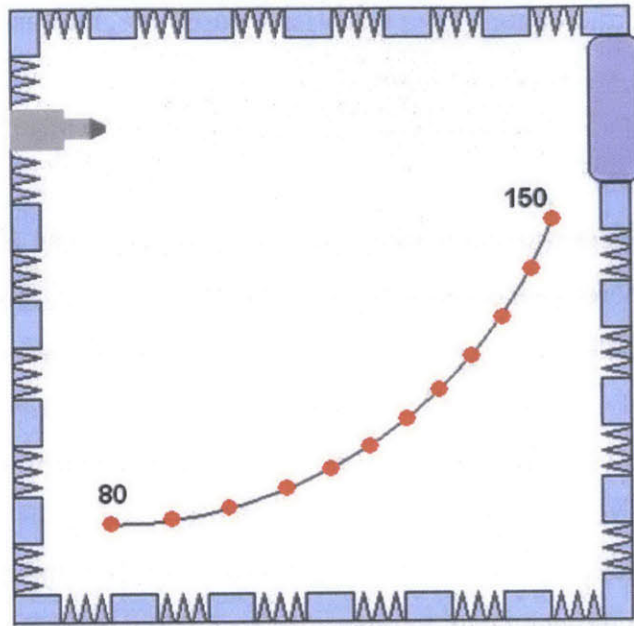


Figure 2.10.2: Microphone locations within the anechoic chamber. The array is a 3.048 m arc whose center is located at the nozzle exit. The microphone is referred to by its downstream angle relative to the flight direction.

Each amplifier channel outputs to a female BNC connector. Coaxial cables then transfer the signal from the conditioning amplifiers in the anechoic chamber to the data acquisition cards in the control room. These cables are terminated with male BNC connectors. Three National Instruments PCI-6110 high-speed data acquisition cards then connect to the DAQ computer. Each card has four analog input channels so in all 12 channels may be sampled simultaneously. The cards have a maximum sampling frequency of 5 MHz, though each microphone is sampled at 204.8 or 250 kHz. The voltage output of each microphone is plotted on the front panel of the DAQ GUI program so that a quick visual inspection may be performed before saving. The data is corrected using the microphone calibration values and converted to pressure (in Pascals) before saving.

2.11 Calibration

Calibration of the microphones is performed using a B&K model 4220 Pistonphone. The pistonphone produces a very accurate 250 Hz signal at 124 dB. The pistonphone has a ¼-inch opening at one end, which is placed over each microphone one at a time. Its weight is supported by a stand that was fabricated in-house. A signal was

collected from each microphone by a LabVIEW based program and the computed SPL value was compared to the 124 dB known SPL. A correction value was found and stored in a correction file. During data acquisition, the program calls this file and automatically adjusts each microphone signal accordingly.

Though very accurate, calibrating with the pistonphone can prove to be extremely time consuming. Therefore, to verify the initial calibration, and thus cut the calibration time, a technique called Charge Injection Calibration (CIC) was used. Within the conditioning amplifier, a small capacitance is introduced—typically 0.2 pF, with a very high leak impedance (50 T Ω). Then a known reference signal is introduced at one of several given frequencies. The resulting measured response is compared with the stimulus and a CIC gain is found from the RMS values. Given the properties of the CIC capacitance, even small changes in the measurement chain cause extreme changes in the CIC gain. As a result, given the fact that no major changes to the CIC gain have occurred, the original calibration values can be verified, and a new calibration need not be performed. Another advantage of using CIC is that changes in the entire measurement chain (not just within the microphone and preamplifier) are detected. Therefore by testing several frequencies, the exact cause of the change (be it a problem with the microphone or a faulty cable) may be diagnosed.

2.12 Ground Plane Microjet Imaging

In order to determine the behavior of the ground plane water microjet within the shear layer, high-speed grayscale videos were obtained. These image data were acquired through the use of a Redlake Y5 high-speed camera with an 85mm/1.4 lens. Grayscale images were taken at a rate of 500 frames per second and with an exposure time of 1997 μ s per image. The camera was sampled for two seconds. A 0 dB sensor gain was used. A glass cage enclosed the camera to protect it from the fine spray of the microjets. Additional illumination was provided through the use of the three 500 W halogen lamps. All of the imaging tests were performed at the cold exhaust condition in order to both avoid damage to the high speed imaging equipment and to allow for full visualization of the microjet. A schematic of the imaging setup including object placement is shown in Figure 2.12.1.

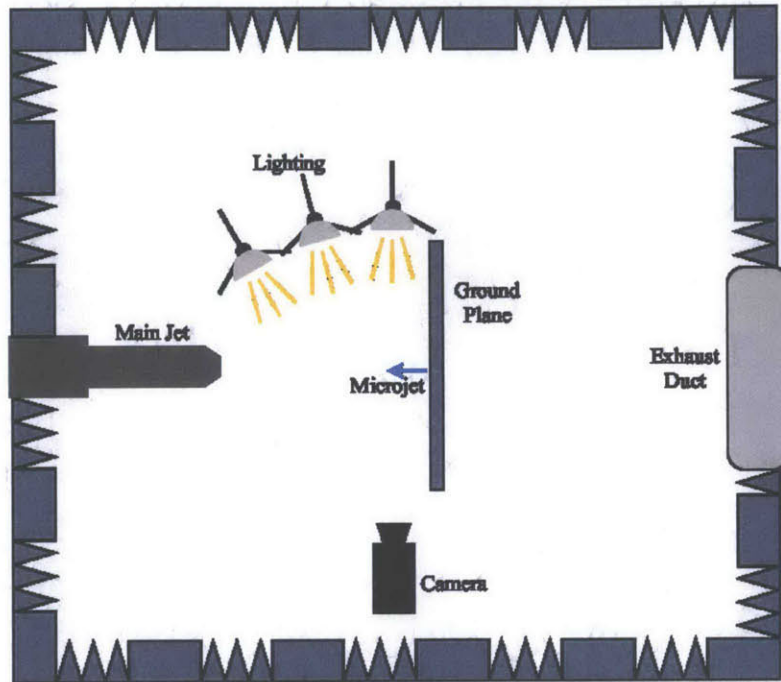


Figure 2.12.1: Simple, overhead schematic of the anechoic chamber, as set up for the high speed imaging tests. The high-speed camera was set up so as to capture the microjet from the side profile angle. Three high-wattage lights were situated, from the point of view of the camera, behind and slightly below the microjet. All imaging tests were performed at the cold exhaust condition.

CHAPTER 3

EXPERIMENTAL PROCEDURE

3.1 Overview

The types of experiments performed over the course of this investigation include ground plane pressure and temperature fluctuations, baseline noise characterization, nozzle microjet injection, ground plane microjet injection, and high-speed microjet imaging. The following chapter discusses the purpose and procedure for each test, as well as the data processing and analysis techniques used.

3.2 Experimental Description

This section describes the basis for each type of experiment. Five types of experiments were conducted to determine the capability of ground plane microjet injection to reduce supersonic jet noise. Each type of test is described in this section.

3.2.1 Ground Plane Pressure and Temperature Fluctuation

The term “baseline” refers to a test performed with no external noise suppression techniques. It is the pure noise profile one would expect when measuring the noise produced from a real jet engine. The efficacy of each noise reduction technique was measured based on the total baseline noise produced by the jet at its operating condition. Therefore, baseline tests play a critical role in this investigation.

Previous work with microjets was performed using a steady injection condition. Using this method, a noise reduction of up to eight dB could be achieved. This quantity refers to the reduced noise as compared with the baseline noise in the peak radiation

direction. The effectiveness of any noise reduction technique is measured against the steady injection noise reduction.

3.2.2 Baseline Noise Characterization

The term “baseline” refers to a test performed with no external noise suppression techniques. It is the pure noise profile one would expect when measuring the noise produced from a real jet engine. The efficacy of each noise reduction technique was measured based on the total baseline noise produced by the jet at its operating condition. Therefore, baseline tests play a critical role in this investigation.

Previous work with microjets was performed using both steady and pulsed injection at the nozzle exit. Using these methods, a noise reduction of up to eight dB could be achieved. This quantity refers to the reduced noise as compared with the baseline noise in the peak radiation direction. The effectiveness of any noise reduction technique is measured against the baseline noise condition.

3.2.3 Nozzle Microjet Injection

Essentially all of the previous work performed using fluid microjets as a method of noise suppression of supersonic jets has focused on the location of these microjets at the nozzle exit. That is to say that a circular array of fluid microjets, fed by a single supply manifold, are arranged so that they point radially inward towards the jet centerline, and enter the shear layer at its inception just downstream of the nozzle exit. Such an implementation was intended as a modification of the aircraft.

Much of the motivation for this study involves a practical approach to the implementation of fluid microjets within the context of reducing military aircraft noise. As such, nozzle microjet injection would not be possible in real-world applications, as they would involve said modifications to the aircraft. Regardless, these tests were carried out both for the sake of comparison and to more properly assess the efficacy of ground plane control.

3.2.4 Ground Plane Microjet Injection

The main goal of this research was to quantify the ability of ground plane fluid microjets to reduce the noise generated by supersonic military aircraft. As such, fluid microjets were mounted into the surface of a ground impingement plane and fired upstream towards the main jet exhaust. The resulting noise signal was compared against the baseline signal in order to quantify the amount of overall noise reduction achievable. This signal was also compared to the effect of microjet injection when implemented at the nozzle exit.

3.2.5 High-Speed Microjet Imaging

In order to characterize the mechanisms by which ground plane microjet injection is able to reduce noise, high-speed videos were obtained. One microjet at the top of the array was utilized to visualize its effect. A high-speed grayscale camera was situated perpendicular to the plane of injection of the microjet. From these videos, the penetration depth and microjet breakup characteristics were observed.

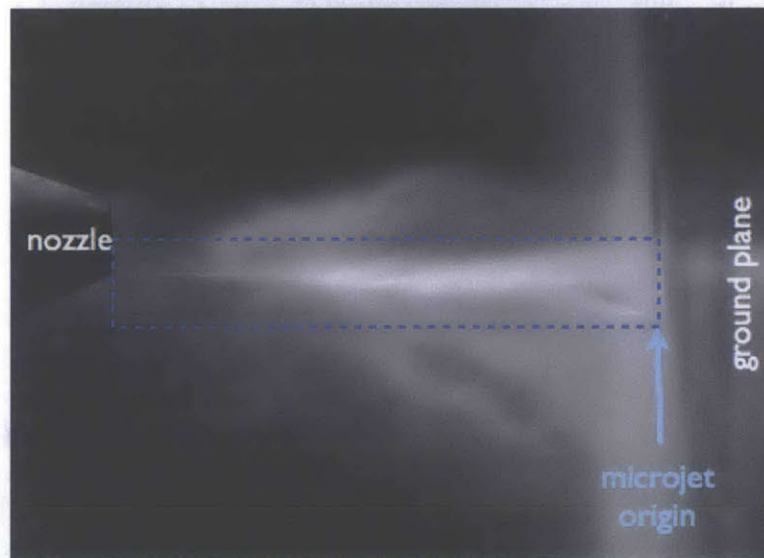


Figure 3.2.1: Sample high-speed image of the nozzle and shear layer. The shear layer was isolated and the average pixel value was calculated. The amount of droplet breakup in the shear layer (evidenced by the presence of fine mist) is proportional to the brightness of the shear layer.

The amount of droplet breakup was characterized by the quantification of fine mist in the shear layer of the jet. This was performed by isolating the shear layer in each image, then calculating the average pixel value. The higher the pixel value the more fine mist is present in the shear layer. A sample image is shown in Figure 3.2.1. It can be seen from this figure how the shear layer was isolated.

In order to quantify the penetration characteristics of the microjet, the same high-speed images were analyzed using contours. For each microjet injection pressure, 500 images were averaged in order to assess the global behavior of the microjet. Brightness contours were then plotted showing areas of equal brightness. A brightness corresponding well with the bounds of the coherent microjet was chosen to be 180 (on a scale from 0-255), and the related contour was analyzed to determine maximum upstream and inward penetration depth. An example of a calculated contour map overlaid on a sample image is shown in figure 3.2.2.

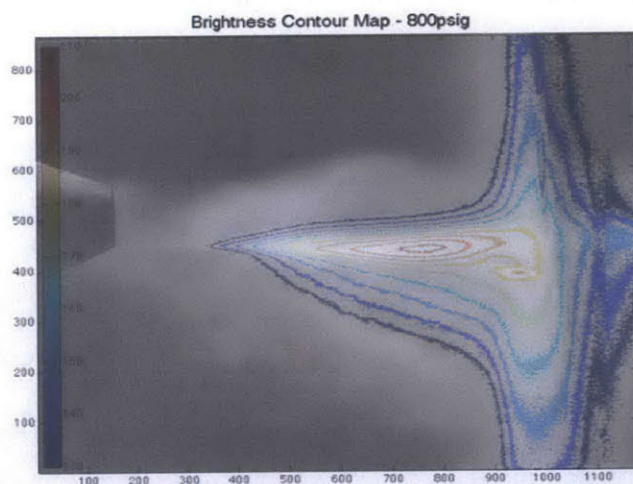


Figure 3.2.2: Contour map for a microjet operating at 800 psig, overlaid on a sample image. A brightness level of 180 (corresponding to the yellow contour) was chosen to most accurately represent the geometric bounds of the coherent microjet. This contour was then analyzed in order to determine the maximum upstream and inward penetration depths.

3.3 Experimental Procedure

As stated in section 2.1.7, three computers located in the control room operate the facility. One computer runs a program for monitoring the SUE burner and another runs a separate program that controls the airflow through the facility. The third computer is the

DAQ computer. It runs a third, separate program that obtains acoustic measurements. Operation of the hot jet facility requires at least two people. The first monitors the burner and flow control computers, as the user interfaces are located at one workstation. The second is responsible for the DAQ control computer.

Each operation condition consists of a given pressure ratio and temperature. A list of these conditions is given in Table 3.1. Once the burner is lit and sufficiently warmed up, temperature control is turned on. This consists of a controller that adjusts the main fuel valve, based on the temperature read by thermocouples downstream of the burner, allowing more fuel for higher temperatures. As such, the pressure ratio may be adjusted easily and the temperature will self-adjust to the target value. The first operator adjusts the air supply settings until the jet is running steadily at the operating condition. In order to fire the microjets, the researcher responsible for burner and flow control will adjust the injection pressure using a dial at that workstation. A rocker switch next to the microjet pressure adjustment dial is thrown to send a signal to a relay, which opens the valve just upstream of the toroidal microjet manifold. Once thrown, the microjets are allowed to reach steady state before acoustic data collection begins. The researcher signals to the second operator that condition is reached and that microjets are firing at steady state. At that point, the second operator starts the data acquisition program. At the start of the program, a signal is sent to the flow control program, which logs the instantaneous room humidity, ambient pressure and temperature. The program then takes three seconds of data simultaneously on all microphones. The program then prompts the second operator to save the data to an appropriately named file. Control parameters and file names are entered prior to program initiation. Once the data has been saved, the second operator signals to the first that it is okay to move to the next operating condition.

Table 3.1: Experimental Run Conditions

Nozzle Design Mach Number	Run Temperature ($^{\circ}\text{F}$ / K)	Nozzle Pressure Ratio
1.5	60 / 290	3.69
1.5	600 / 590	3.64
1.5	1000 / 810	3.60
1.5	1400 / 1033	3.57
1.5	1700 / 1200	3.54

3.4 Acoustic Data Processing and Analysis

In collecting acoustic data, the overall sound pressure level is the most obvious indicator of the noise generated by a jet, as well as the amount of noise reduction achieved. This value is derived from the frequency spectra obtained from the raw pressure data. The methods by which the frequency spectra and overall sound pressure level were calculated are described in the following section. Also discussed is the technique by which the flow rates through the injectors were measured.

3.4.1 Frequency Spectra

In order to compare noise reductions, it is necessary to convert the pressure-time signal (the form in which it arrives from the microphones) into a single overall sound pressure level (OASPL) value. This is a catchall value that, in effect, is a measure of the magnitude of the noise at a given location. Derived from the frequency spectrum, its computation uses the methodology described in Bendat and Piersol [49]. First discussed will be the computation of the frequency spectrum.

The microphones are sampled at for three seconds at a frequency of 204,800 Hz. At each microphone location, this gives a total of 614,400 samples. First, it is necessary to subtract the mean from the pressure-time signal. This gives a new signal, $p' = p - \bar{p}$, which has a zero mean, from which it is easier to calculate the frequency spectrum. It is computationally advantageous, at this point, to divide p' into subsets of equal size. Choosing a subset size of a power of two ensures that the subsequent Fourier transforms are simple to perform. Therefore, in this case, the subset size is chosen as 4096, or 2^{12} . Then, to increase the number of subsets, the data is overlapped by 50%. This gives a total of $2\left(\frac{N}{n_s}\right) - 1 = 2\left(\frac{614,400}{4096}\right) - 1 = 299$ subsets. Before a Fourier transform is performed, the subsets are windowed using a Hanning window, which is defined by

$$w_h = 1 - \cos^2 \frac{\pi t}{T},$$

where T is the length of the subset, or 4096, and t is the index of the sample. The subsets are windowed in order to reduce side lobe leakage, and are thus ready for Fourier transformation. Using the Cooley-Tukey procedure, each windowed subset is transformed. The subset is then multiplied by the Hanning scale factor of $\sqrt{\frac{8}{3}}$. Each value in the transformed subset is then multiplied by its complex conjugate to ensure that the entire subset contains only real parts. Then all the subsets are averaged, and a spectrum is obtained. The spectrum has units of [pressure²/frequency]. Using the notation in Bendat and Piersol [49], the one-sided autospectral density function is then estimated by

$$\hat{G}_{pp}(f_k) = \begin{cases} \frac{2}{n_d N \Delta t} \sum_{i=1}^{n_d} |P_i(f_k)|^2 & k = 1, 2, 3, \dots, [(N/2 - 1)] \\ \frac{1}{n_d N \Delta t} \sum_{i=1}^{n_d} |P_i(f_k)|^2 & k = 0, (N/2) \end{cases} .$$

Multiplying \hat{G}_{pp} by the frequency spacing, $\Delta f = \frac{f_s}{n_s} = \frac{204,800}{4096} = 50$, gives the autospectral density function with units of [pressure²]. The final step is then to calculate the frequency spectrum in terms of the sound pressure level (SPL) by

$$SPL(f_k) = 10 \cdot \log \left(\frac{\hat{G}_{pp}(f_k)}{p_{ref}^2} \right),$$

where p_{ref} is defined as 20 μ Pa.

3.4.2 Overall Sound Pressure Level

The overall sound pressure level is calculated from the autospectral density function discussed in the last section. The autospectral density function is integrated numerically by Simpson's method using the frequency spacing, Δf , as the step size. This value, referred to as p_{rms}^2 , has units of [pressure²]. The final OASPL value is then calculated by

$$OASPL = 10 \cdot \log \left(\frac{p_{rms}^2}{p_{ref}^2} \right),$$

where p_{ref} is again defined as 20 μPa .

3.4.3 Skewness

In order to more carefully isolate the reduction in OASPL due to Mach wave radiation, the skewness of the pressure-time signal was computed. Previously, this metric has been used only as an indicator of the presence of the crackle in the jet. Skewness levels above 0.4 indicate that crackle is indeed present, while values below this value are inconclusive.

Since Mach wave radiation and crackle are within the same family of noise generation – that is, ballistic shock waves – crackle can be used as a comparative metric to quantify the relative amount of suppression of the Mach wave radiation noise source. It is computed from the pressure-time signal and its standard deviation as follows:

$$k = \frac{\langle p^3 \rangle}{\sigma_p^3}.$$

Though the magnitude of the skewness is not expected to exceed the 0.4 threshold to signify the presence of crackle, a reduction in baseline skewness values will suggest a reduction in the Mach wave radiation noise source.

3.4.4 Injector Flow Rates

A rather elementary, but effective, method was used to determine the flow rate of water through each injector for various injection pressures. The microjet injection pressure was adjusted accordingly and the valve opened so as to allow water to flow freely for three seconds. The water ejected during the operation period was collected in a beaker of known mass, and the mass of the water was determined using a triple-beam balance. Dividing this mass by three seconds yields the mass flow rate.

3.5 Uncertainty Estimates

Great care was taken in the design of the facility and of the data acquisition systems used in the collection of this data. Therefore, few sources of error and uncertainty exist. However, this section discusses the few remaining uncertainties and their effect on the results.

3.5.1 Acoustic Uncertainty

While there are several schools of thought regarding uncertainty, the absolute uncertainty, which gives the worst-case scenario, is presented. Since the microphone response is taken into account in the data acquisition program, and is factored even before saving, the only remaining uncertainties lie with the resolution of the DAQ cards in conjunction with the gains specified by the card and the amplifier. The worst-case scenario with respect to uncertainty occurs when the input range is set to ± 10 V and the amplifier gain is set to 3.16 mV/Pa (its lowest value). Since the DAQ resolution is constant (12 bit), the uncertainty in pressure is obtained by the following:

$$\varepsilon_p = \frac{1}{2} \frac{\text{range}}{\text{resolution}} \frac{1}{\text{gain}} = \frac{1}{2} \left(\frac{20V}{4096} \right) \frac{1}{3.14 \text{ mV/Pa}} = 0.77 \text{ Pa}.$$

For the range that is most important to this study, that around 130dB, this corresponds to an uncertainty of ± 0.1 dB.

CHAPTER 4

RESULTS AND DISCUSSION

4.1 Overview

Throughout the course of this study, many types of experiments were conducted in order to characterize the facility, obtain baseline measurements without control, and to assess the efficacy of ground plane fluid microjet injection to reduce the noise generated by supersonic military aircraft. This section describes the results of those experiments along with a discussion of their implications.

4.2 Characterization of the High-Temperature, Supersonic Jet Facility

As previously mentioned, the experiments performed as part of this study were carried out at the High-Temperature, Supersonic Jet Facility on the main campus of the Florida State University. Prior to this study, the facility had been exclusively utilized to measure the noise generated by free jets. Past studies involving impinging jets had been performed in other laboratories, namely, the Short Take Off and Vertical Landing (STOVL) laboratory at the same university. While able to perform experiments with more complicated geometry, the STOVL facility was not without its limitations. Specifically, it was designed initially for the purpose of flow visualization. As such, only the cold condition could be achieved. Recently, high-power electric heaters were installed to allow for main jet exhaust temperatures up to 600K to be achieved. However, most military aircraft, especially during takeoff, operate near 1200K. In order to mimic these conditions, an impinging setup was constructed within the anechoic chamber of the High-Temperature, Supersonic Jet Facility. In order to be able to fully compare the

results obtained in this facility, ground plane pressure fluctuation measurements were taken at lower temperatures and compared to results obtained previously in the STOVL facility. The results of these tests are shown in Figure 4.2.1.

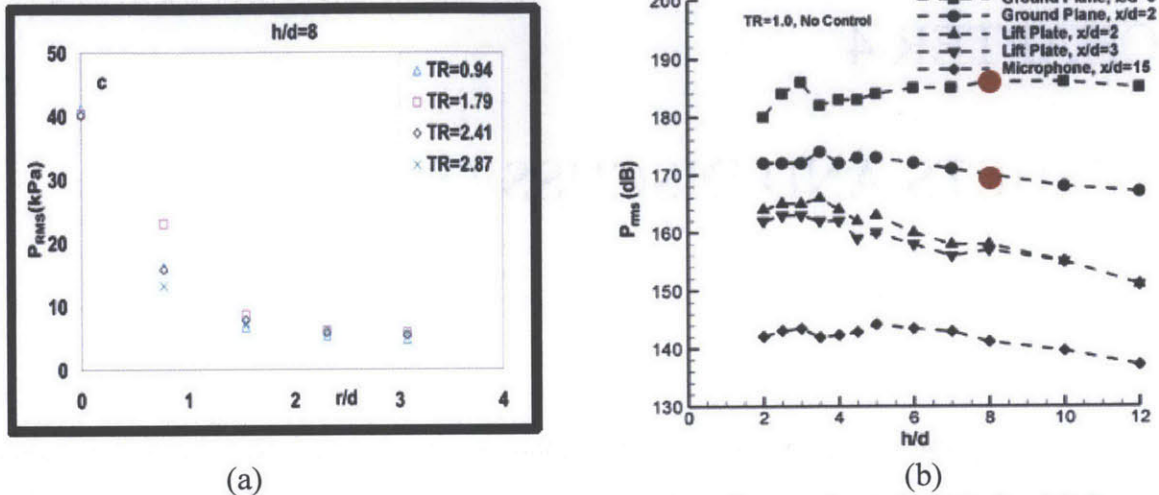


Figure 4.2.1: Summary of ground plane pressure fluctuations for (a) the High-Temperature, Supersonic Jet Facility taken at $h/d=8$ and for (b) the STOVL facility (Kumar et. al. [43]). There is only a small temperature effect on the ground plane pressure fluctuations, as can be seen especially at an r/d of 0.8. However, both studies show matching results at $r/d=0$, where the pressure fluctuations were determined to be 186 dB, and at $r/d=1.53$ ($r/d=2$ for Kumar et. al.), where the pressure fluctuations were determined to be 170 dB. The agreement of the corresponding points from the present study is shown in (b) by the red dots.

The results in Figure 4.2.1(a) were obtained using ground plane mounted, water-cooled Kulite pressure transducers. The ground plane was positioned a distance of $h/d=8$ from the nozzle exit, and the Kulites were spaced 1.0 inches apart, from the jet centerline radially outward. The results shown in Figure 4.2.1(b) were obtained using ordinary Kulite pressure transducers by Kumar et al. As expected, the magnitude of the pressure fluctuations falls off monotonically with radial distance from the jet centerline. One interesting detail is the lack of temperature effect on the fluctuations. Small variations can be seen at $r/d=0.8$, possibly due to the change in the development of the shear layer as a result. However, no significant differences at the other locations were observed.

From Figure 4.2.1, good agreement between the results obtained in both facilities is observed. At $r/d=0$, corresponding to the pressure transducer located at the jet centerline, both studies report pressure fluctuation with a magnitude of 186 dB. At

$r/d=1.53$ (or $r/d=2$ for Kumar et. al.), both studies report pressure fluctuations with a magnitude of 170 dB. This agreement is shown in Figure 4.2.1(b) by the red dots, which correspond to the conditions previously mentioned from this study.

The frequency spectra for the ground plane pressure transducers are shown in Figure 4.2.2. This figure demonstrates that although the overall pressure levels vary little with temperature changes (as shown from Figure 4.2.1), great differences exist in the tonal location and spectral energy densities. For example, as the temperature is raised, the higher frequency energy content is raised. That is, the broadband noise above 5 kHz is increased at higher temperatures. Another interesting feature of Figure 4.2.2(a) is that, at a temperature ratio of 2.20, there appears to be less low frequency broadband noise than at other temperature ratios. This is also true at $h/d=6$. However, it appears that this effect is not significant at $h/d=8$.

Another clear feature of Figure 4.2.2 is the presence of large feedback tones. As the ground plane is moved away from the nozzle exit, the magnitude of the primary peak over the broadband noise decreases. For example, for the cold jet at $h/d=4$, the primary feedback tone is approximately 25 dB above the broadband noise. At $h/d=6$ the tone decreases to only about 18 dB above the broadband noise, and at $h/d=8$ the tone shrinks to only about 12 dB above the broadband noise.

As the temperature is raised, the location of the primary feedback tone shifts significantly, though it falls consistently within the 3-6 kHz range. The peak frequency of each of the spectra is a function of the flow characteristics of the jet as well as the geometry, and indicates the tonal feedback frequency. As can be seen from this figure, the peak frequency corresponds well with those found in previous studies.

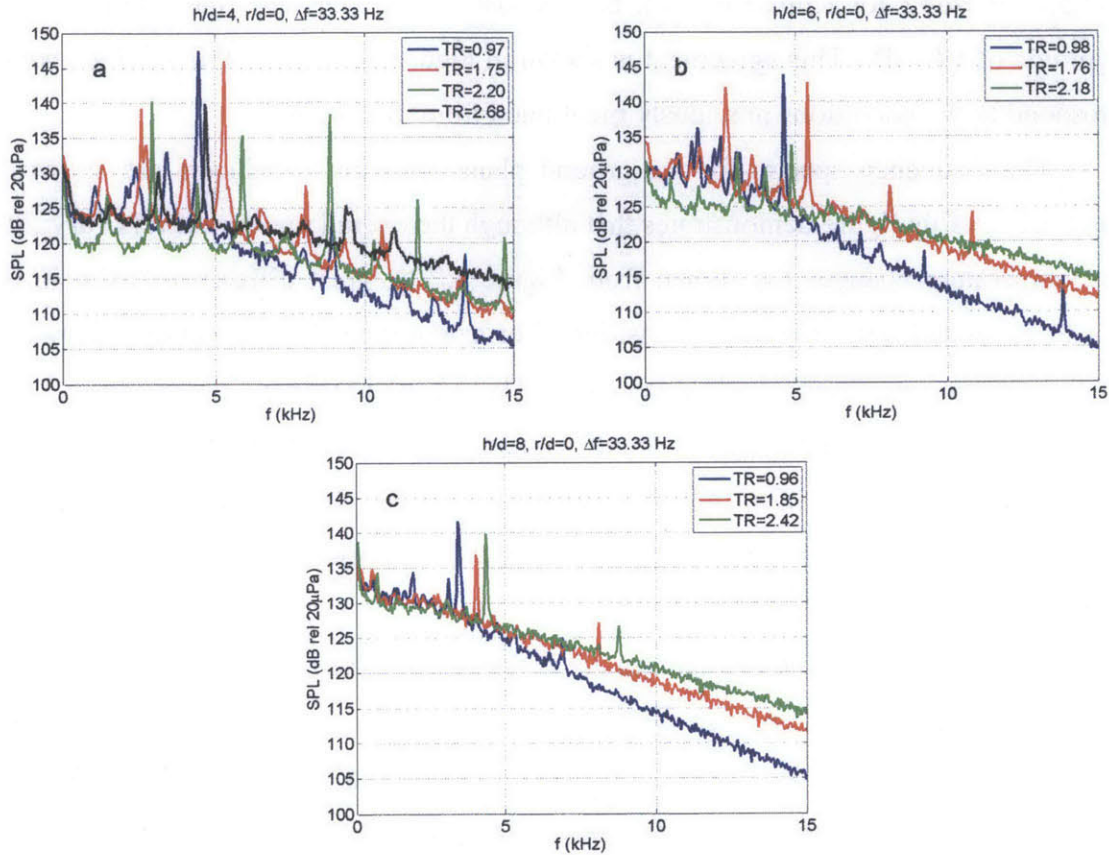


Figure 4.2.2: Ground plane frequency spectra for various jet exhaust temperatures at (a) $h/d=4$, (b) $h/d=6$ and (c) $h/d=8$. The primary peak location, indicating the feedback tone frequency, matches well with previous studies. It should be noted that this frequency changes as the temperature is adjusted. This is due to the fact that the feedback phenomenon is governed by certain flow and geometric parameters such as the axial distance of the ground plane and the convective velocity of the large scale vortical structures.

As the temperature is raised, the feedback tone shifts. This is a result of the feedback frequency's dependence on the flow parameters of the jet as well as the geometric properties with which it is constrained. The frequency can be predicted by the equation

$$f_{feedback} = \left(\oint \frac{1}{U_{pressure}} ds \right)^{-1},$$

where $U_{pressure}$ is the velocity of the pressure wave, and is evaluated along its path from the nozzle exit to the ground plane and then back again. Essentially, the meaning of this integral is just the inverse of the sum of the time required from a pressure wave to be

convected downstream by its associated vortex from the nozzle exit to the ground plane and the time required to propagate back to the nozzle exit after reflection. Ideally, this integral would be evaluated continuously along the path of the pressure wave. However, this requires explicit knowledge of the local temperature everywhere along the path of the wave. While this is not realistically possible, the feedback frequency can be estimated quite well using the convective velocity and the ambient speed of sound. The integral is simplified in the following manner:

$$\begin{aligned}
 f_{feedback} &= \frac{1}{t_c + t_{ref}} \\
 &= \frac{1}{\frac{h}{U_c} + \frac{h}{a_\infty}} \\
 &= \frac{U_c a_\infty}{h} \left(\frac{1}{U_c + a_\infty} \right)
 \end{aligned}$$

where t_c is the convection time and t_{ref} is the reflection time. As can be seen from this relationship, the primary feedback tone frequency is dependent on jet operating temperature through the convective velocity variable.

For further comparison, the ground plane pressure frequency spectra for varying radial measurement location are shown in Figure 4.2.3.

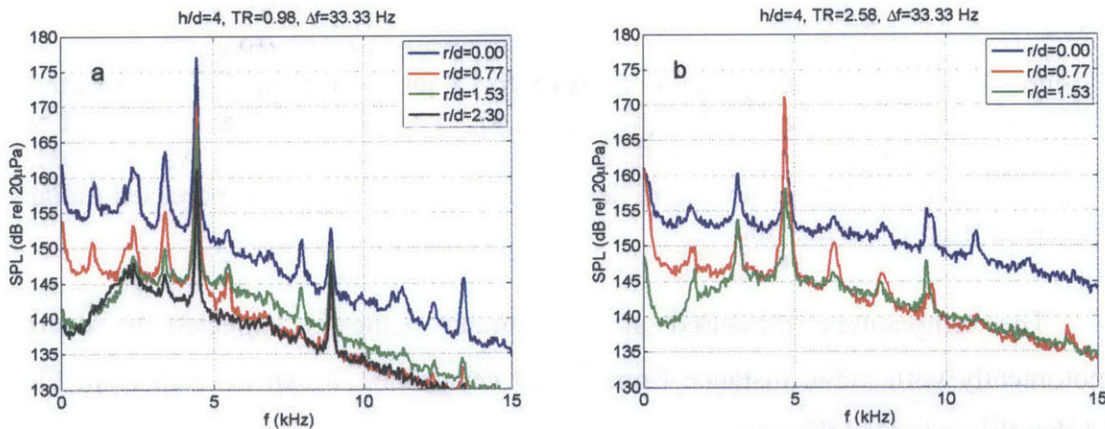


Figure 4.2.3: Ground plane frequency spectra at varying radial locations for an axial distance of $h/d=4$ for a jet operating at (a) the cold condition and (b) 900°F . In this case, the location of the primary feedback tone is not affected by the location of the measurement. It is, as can be seen through comparison of the two figures, affected by the operating temperature.

As can be seen from Figure 4.2.3, the location of the primary feedback tone is not affected by the radial measurement location. This is to be expected, as the feedback reflection phenomenon is, with respect to the ground plane, a global phenomenon.

4.3 Ground Plane Temperature Measurements

In order to further characterize the impinging jet modifications to the High-Temperature, Supersonic Jet Facility, as well as to further investigate behavior of the jet upon interaction with the ground plane, exposed bead thermocouple transducers were used to measure the temperature behavior radially outward from the jet centerline. The mean temperature profiles for each of the operating conditions at $h/d=8$ and 10 are given in Figure 4.3.1.

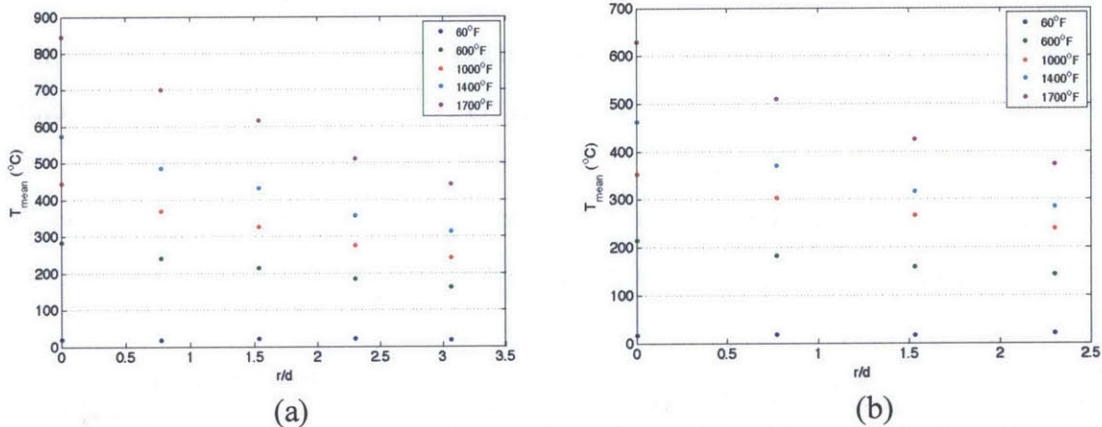


Figure 4.3.1: Mean temperature profiles for a jet with ground plane located downstream of the nozzle exit at (a) $h/d=8$ and (b) $h/d=10$. Data are presented at varying temperatures and radial distances from the jet centerline. As expected, the mean ground plane temperature decreases monotonically with increased radial distance from the centerline.

The temperature measured at the ground plane is expected to decrease monotonically with radial distance from the jet centerline. It can be seen from Figure 4.3.1 that this is indeed the case.

It was found by Kumar et al. [43], that the ground plane temperature fluctuations match well with the fluid-mechanical structures at that location. A local maximum in temperature fluctuations would suggest an area of increased fluid-mechanical activity at the same location. Figure 4.3.2 shows the results from these temperature experiments.

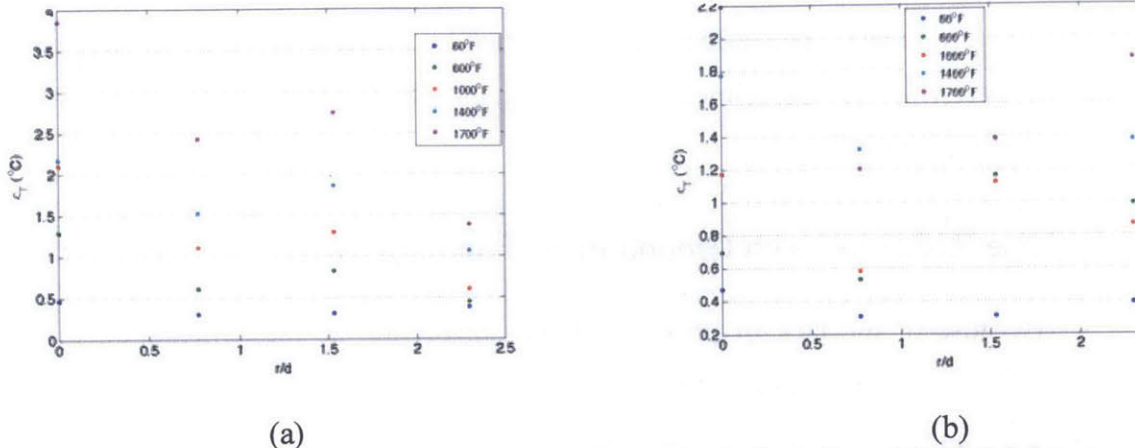


Figure 4.3.2: Temperature fluctuations on the ground plane for a Mach 1.5 jet at (a) an axial distance of $h/d=8$ and (b) an axial distance of $h/d=10$. Unlike the pressure fluctuations, temperature fluctuations demonstrate a local maximum at $r/d=1.53$, indicating that temperature fluctuations, and thus fluid mechanical fluctuations, reach a maximum at that location.

Generally, as before, the magnitude of temperature fluctuations decreases with radial distance from the jet centerline. However, it should be noted that there exists a local maximum in these data at a radial location of $r/d=1.53$. This would serve to suggest an area of increased fluid-mechanical activity at this location. As a first approximation, the shear layer may be assumed to grow linearly, and the potential core (where the shear layer meets at the jet centerline) exists at a location given empirically by:

$$\frac{x}{d} = 3.134e^{(1.043M_j - M_c)},$$

where M_j is the main jet Mach number, and M_c is the convective Mach number, given by the formula:

$$M_c = \frac{U_j - U_\infty}{a_j + a_\infty}.$$

For these particular conditions, x/d ranges from 7.81 for the cold jet to 5.87 for the jet operating at 1700°F. That is to say, as the temperature increases, the relative location of the $r/d=1.53$ thermocouple is closer to the center of the shear layer where large-scale vortical structures exist. This would serve to explain the more exaggerated local maximum behavior in Figure 4.3.2(a), and 4.3.2(b) for temperatures up to 1400°F. The behavior showing large temperature fluctuations at the $r/d=2.31$ location for the jet with the ground plane located at an axial distance of $h/d=10$ at the higher temperatures may be

a result of entrainment. This effect was not studied by Lazic, as the experimental facility used to perform the experiments in that publication could only reach exhaust temperatures up to 600°F.

4.4 Noise Reduction with Ground Plane Fluid Microjets

Because of the lack of previous studies involving the implementation of noise control at the ground plane, many variables associated with microjet control were investigated and optimized through the course of this study. To that end, jet noise reduction tests were performed using ground plane fluid microjets primarily with water as the working fluid. However, ground plane tests were also performed using nitrogen gas as the working fluid. The majority of the experiments were performed with the microjets aimed toward the jet centerline at 60° from the ground plane normal (See Figures 2.8.3 and 2.8.4). However, the effect of adjusting both the injection angle and origin was considered. For the sake of comparison, experiments were also carried out using microjet injection at the nozzle exit. The results of these tests are presented in this section.

4.4.1 Ground Plane Water Microjet Injection

The 80° and 90° microphone spectra are presented in Figure 4.4.1 at an axial distance from the nozzle exit of 8 nozzle throat diameters. In all of these spectra, there is a main peak associated with the resonance tone resulting from feedback. This tone is located at approximately 3 kHz, and corresponds well to the peak found in the spectra from previous studies, as well as that found in the temperature fluctuation spectra shown earlier. The first set of spectra below, corresponding to Figure 4.4.1(a), show the results obtained for an exhaust temperature near 60°F. Without control, both microphones show significant resonance tones due to the shockwave feedback mechanism in the flow. With control, both microphones show an attenuation of these resonance tones. This suggests that the ground plane water jets are effectively breaking the feedback loop responsible for these tones. This is also apparent for the 600°F and 1000°F cases where the feedback mechanism is present. In Figure 4.4.1(a) and (b), there is also an additional reduction of the high-frequency broadband noise. Raising the temperature to 1000°F, however, the high-frequency broadband noise is actually increased.

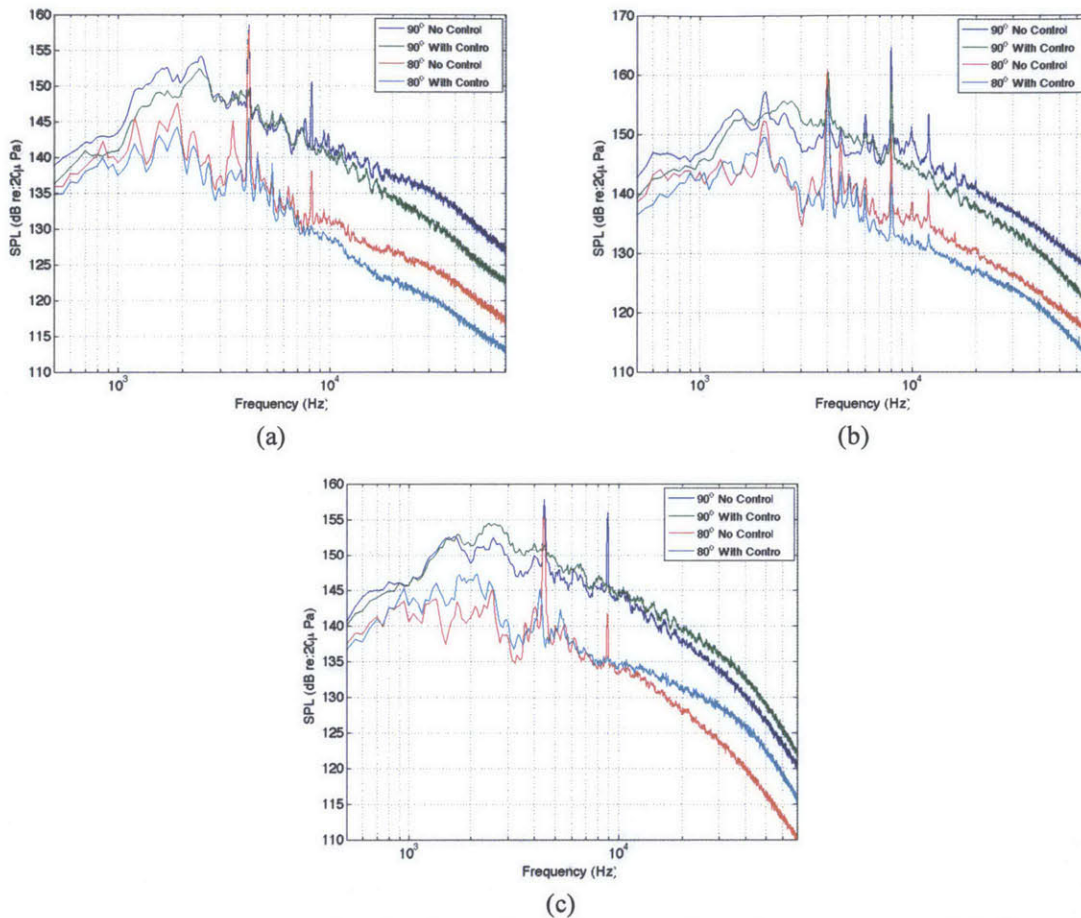


Figure 4.4.1: Spectra for the 80 and 90 degree microphones at an axial distance of 8 nozzle diameters. Individual plots with baseline and control cases are given for temperatures of (a) 60, (b) 600 and (c) 1000°F. In all cases, ground plane microjet control produces significant reduction of the feedback tones. This suggests that they are effective in breaking the feedback loop. For lower temperatures, broadband noise reduction is also achieved.

Figure 4.4.2 shows the 80° and 90° microphone spectra obtained with the ground plane at 10 throat diameters downstream from the nozzle exit. As with the previous cases, for exhaust temperatures of 60°F and 600°F (corresponding to a and b respectively), the spectra show an attenuation of the resonance tones as well as a reduction of the high-frequency broadband noise. Figure 4.4.2(c) and (d) show the results for the 1000°F and 1400°F jet respectively. Unlike the previous cases, the baseline spectra show no evidence of resonance tones. With no feedback loop to break, the water jets produce no tonal attenuation. Also, as was the case at 8 throat diameters

and higher temperature, these two cases show an increase in the high-frequency broadband noise.

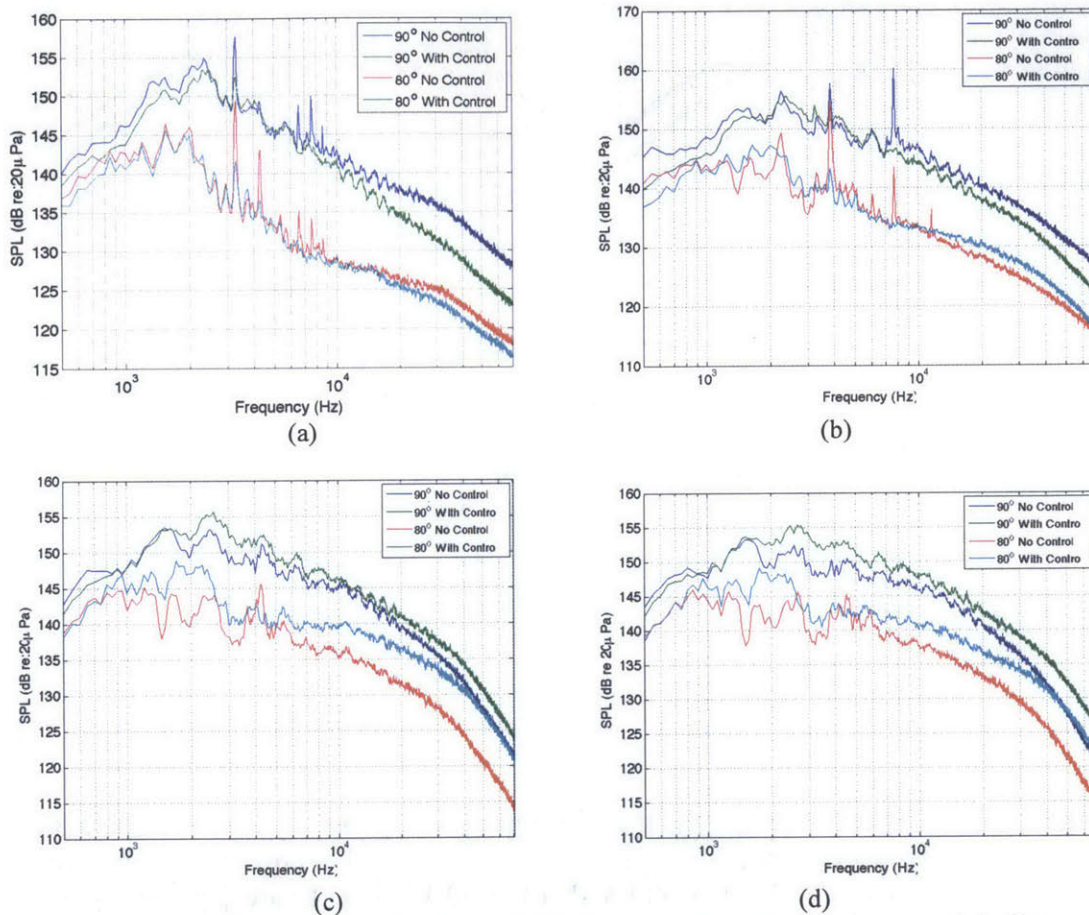


Figure 4.4.2: Spectra for the 80 and 90 degree microphones at an axial distance of 10 nozzle diameters. Individual plots with baseline and control cases are given for temperatures of (a) 60, (b) 600, (c) 1000 and (d) 1400°F. Where present, the feedback tones were shown to be reduced using ground plane microjet control. Again, for lower temperatures, broadband noise reduction is achieved as well.

Finally, in figure 4.4.3, OASPL values are presented for both downstream locations. This figure clearly shows the trend of noise reduction using oblique water jets. For both cases, there is a crossover between 600°F and 1000°F where, between these values, the water jets change from producing an overall beneficial to a detrimental effect on the noise produced by a Mach 1.5 impinging jet. It should be noted, however, that the crossover point for the axial distance of 8 throat diameters appears to be less drastic than that for the second case. In both instances, increases in the high frequency, broadband noise were produced. However, resonance tone attenuation was produced in the first case

while no tones were observed in the second. This may serve to explain why the magnitude of the crossover for the first case is less severe than that of the second case.

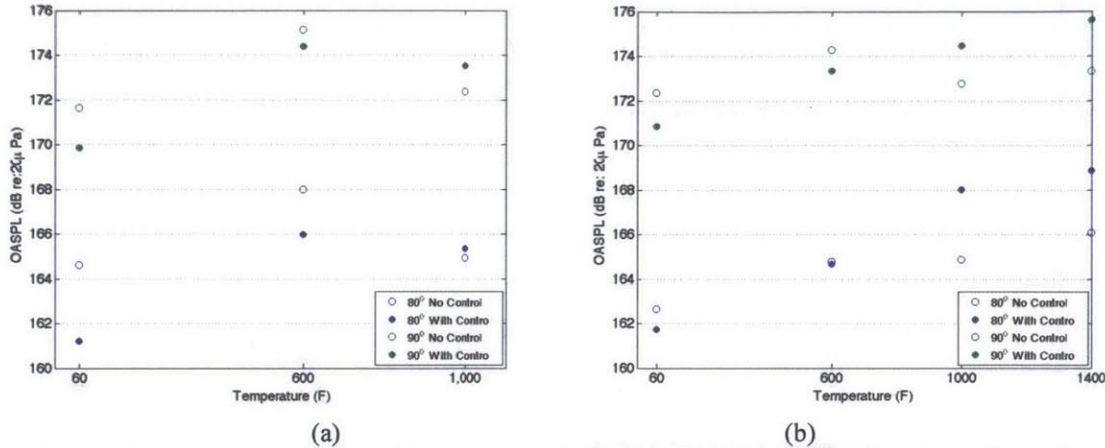


Figure 4.4.3: Overall sound pressure levels for the 80° and 90° microphones at various temperatures. The data for downstream axial distances are presented for both (a) 8 and (b) 10 nozzle throat diameters. There appears to be a crossover point where, when increasing the temperature, the OASPL is no longer reduced by microjet control.

It has been shown up to this point that water microjet injection is effective in reducing the spectral tones associated with feedback. In order to reduce these tones, the feedback need simply be broken. Traditionally, this has been accomplished by modifying a feature of the nozzle exit. That is to say, reducing the nozzle lip thickness, adjusting aircraft geometry, or implementing noise control at the nozzle exit are all successful methods in breaking the feedback loop. However, the results in this study show that breaking the feedback loop at the ground plane is also an effective method for reducing feedback associated tones. Additionally, for lower temperatures, ground plane microjet injection is effective in producing a reduction in the broadband, shock-associated noise.

One would expect that the amount of water injected (as indicated by injection pressure) would have a positive effect on the amount of noise reduction achieved for a given run condition. Figure 4.4.4 shows the results of adjusting injection pressure on the overall sound pressure level.

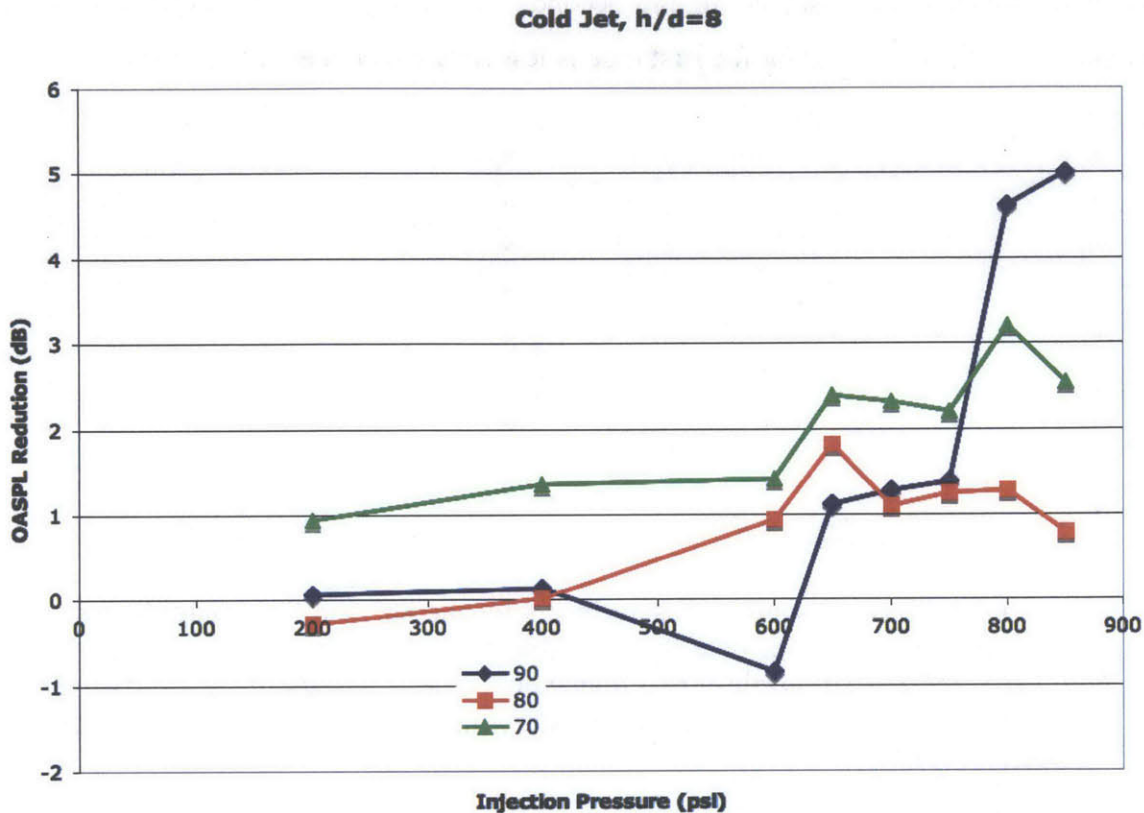


Figure 4.4.4: Reduction in farfield OASPL as a function of injection pressure for the 70, 80 and 90 degree locations with the ground plane at $h/d=8$. Minimal reductions are achieved below an injection pressure of 600 psig. Pressures at and above 600 psig show larger reductions for all microphones, while a drastic increase in reduction, especially for the 90 degree microphone, is shown for injection pressures above 750 psig.

Indeed, it can be seen from the data that increasing injection pressure produces greater reductions in the OASPL. Interestingly, however, is the fact that a drastic increase in noise reduction for the 90 degree microphone is shown at pressures greater than 750 psig. This phenomenon, as well as an explanation for the mechanism, will be discussed further in Section 4.5.

Similarly, a summary plot of the reduction in OASPL as a function of microjet injection pressure for the jet operating at 600°F is shown in Figure 4.4.5. No reduction in noise is achieved for microjets operating at pressures below 600 psig. In fact, with the exception of the 90 degree microphone at 600 psig a net increase in sound was generated. However, at pressures above 600 psig, all three microphone locations saw net reductions in noise. This effect was especially pronounced for the 70 degree microphone, where

reductions of nearly 2 dB were achieved. While the extra advantage of the microjets at high pressure is not observed at this elevated pressure, a similar trend is observed in that high pressure microjets are required to produce appreciable noise reductions.

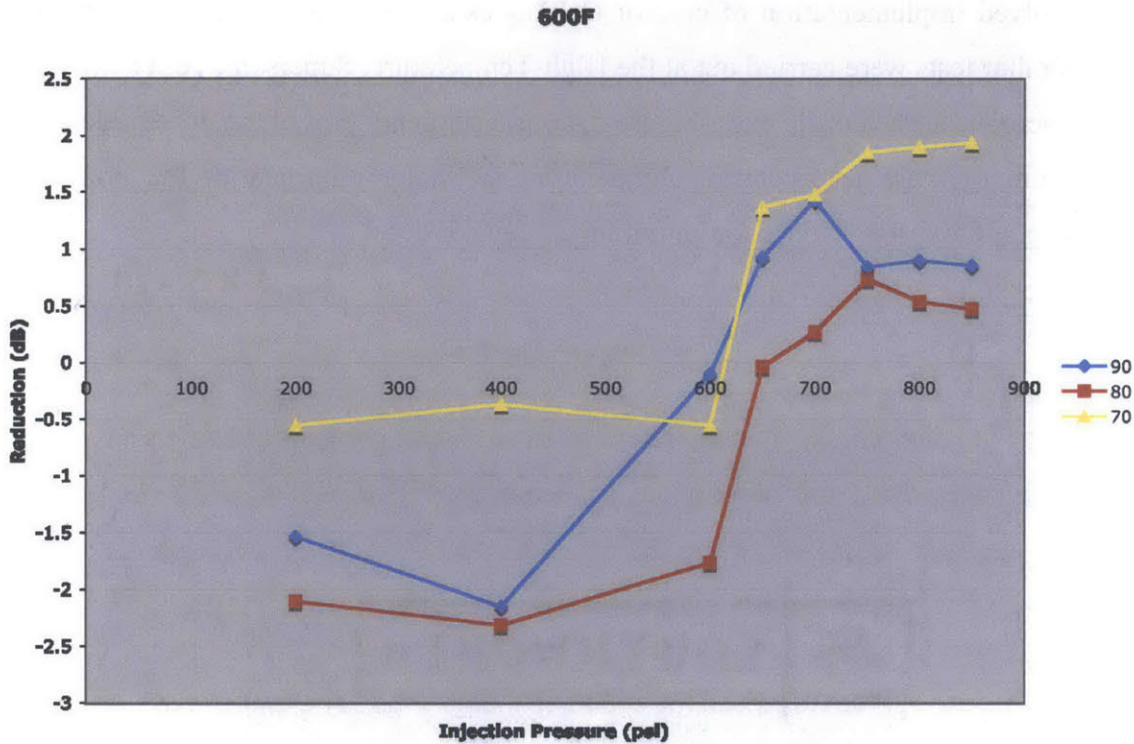


Figure 4.4.5: Reduction in farfield OASPL of a jet operating at 600°F as a function of injection pressure for the 70, 80 and 90 degree locations with the ground plane at $h/d=8$. No reduction was achieved at and below an injection pressure of 600 psig. Pressures above 600 psig show larger reductions for all microphones, and especially for the 70 degree location.

One notable difference between the reduction curves of the cold jet and the jet operating at 600°F is that larger pressures are required in the latter case in order to produce appreciable reductions in the farfield noise. As temperature increases, the shear layer grows more rapidly and is therefore thicker at the ground plane. A microjet must penetrate the thicker shear layer to the same point in order to effect the same amount of reduction. At a given pressure, a microjet is not able to penetrate relatively as far for higher temperature jets. Therefore, only microjets operating at higher pressure are able to reach this location.

4.4.2 Comparison with Microjet Injection at the Nozzle Exit

Up until this point, the state of the art with noise suppression of supersonic jets has involved implementation of control techniques at the nozzle exit. For comparison sake, similar tests were carried out at the High-Temperature, Supersonic Jet Facility using fluid microjets at the nozzle exit. Figure 4.4.6 is a summary plot of the noise reduction as a function of main jet operating temperature for water microjets at the nozzle exit operating at 800 psig. This is for an impinging jet at $h/d=8$.

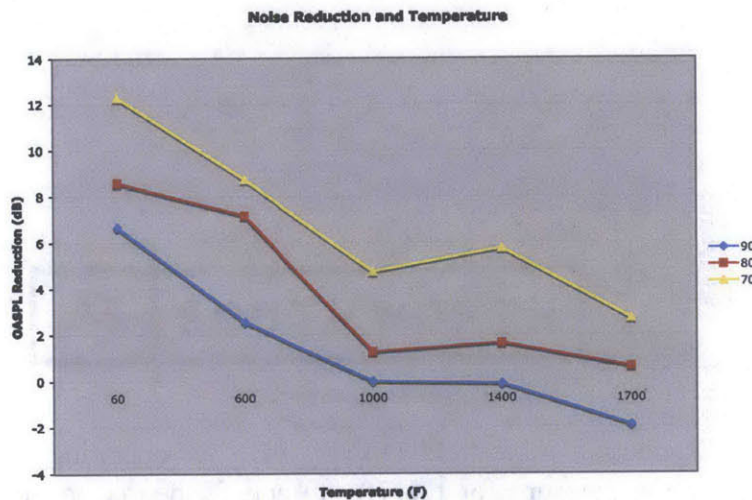


Figure 4.4.6: Summary plot of noise reduction as a function of jet temperature for 800 psig water microjets at the nozzle exit for an impinging jet at $h/d=8$. The most noise reduction (12 dB) is achieved for the 70 degree microphone for the cold jet. As expected, for all three microphones, the noise reduction falls off as temperature increases.

From this figure it can be seen that the most noise reduction is seen by the 70 degree microphone while the jet was operating at its cold condition. The amount of noise reduction decreases as the exhaust temperature of the main jet is increased. In his thesis, Greska saw reductions between 8 and 10 dB. In this study, larger reductions are seen at the sideline angles, but this is due primarily to the presence of strong feedback tones observed in this study that were not present in the free jet tests he performed.

A summary plot of noise reduction for a cold jet operating at $h/d=8$ is shown as a function of microjet injection pressure in Figure 4.4.7. As expected, the amount of noise

reduction increases monotonically with injection pressure. Interestingly, the most noise reduction is seen at the 70 degree location.

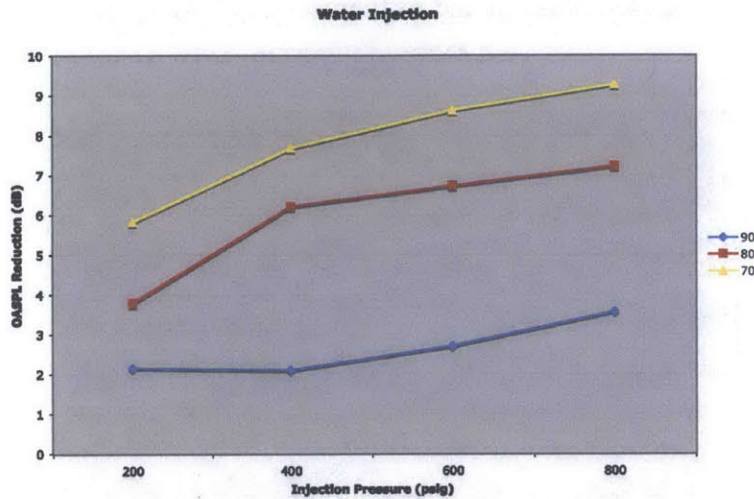


Figure 4.4.7: Summary plot of noise reduction as a function of injection pressure for a cold jet. As expected, the amount of noise reduction increases with microjet injection pressure for all three microphone locations.

4.4.3 The Effect of Working Fluid Type

Essentially all of the previous work involving reduction of impinging jet noise using microjets has involved using air (or nitrogen) as the working fluid. This has proved quite successful when implemented at the nozzle exit, both for steady injection and pulsing. This is attributed to the ability of the microjet to inhibit the growth of large-scale vortical structures right from the nozzle exit. They are thus able to decrease the mach wave associated noise as well as feedback tones. In order to measure the influence and effect of the working fluid type, several experiments were performed using nitrogen gas as the working microjet fluid.

A summary plot of the reduction of farfield noise using nitrogen microjets at the nozzle exit as a function of injection pressure is shown in Figure 4.4.8. For this figure, the jet is impinging on the ground plane at an axial distance of $h/d=8$. Interestingly, it can be seen from this figure that the injection pressure has very little influence on the amount of noise reduction achieved for the 90 and 80 degree microphones. Slight gains are achieved at higher injection pressures for the 70 degree microphone. At higher injection pressures, the microjets actually exhaust supersonically into the main jet flow.

So although the microjets are effective at breaking the feedback loop, reducing feedback tones, and breaking up large-scale vortical structures in the shear layer, they become sources of shock-associated noise in and of themselves at higher pressure.

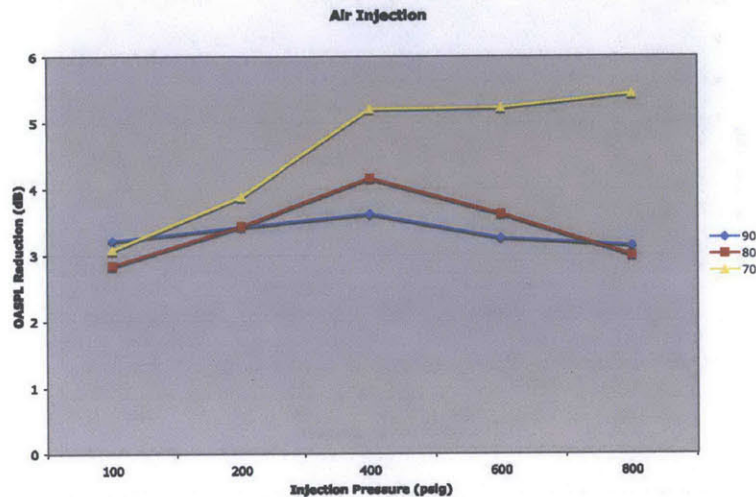


Figure 4.4.8: Reduction of farfield jet noise as a function of injection pressure for Nitrogen microjets at the nozzle exit. The results obtained here match well with those of previous studies. These microjets are effective even at low injection pressures. At the sideline angles, no discernable advantage is seen for using higher injection pressures. This is due to the fact that at higher pressures, the microjets become supersonic and become noise sources in and of themselves

4.4.4 The Effect of Radial Position

Previously, many experiments were performed by taking measurements along the ground plane at varying radial distances from the jet centerline. Similarly, a series of experiments was carried out in order to determine the effect of adjusting microjet radial position on the noise reduction of the main jet. In order to vary the microjet radial location, new center ground planes were machined out of stainless steel in which mounting holes at the required radial distance were drilled. The microjet tubes were mounted into these new holes.

A summary plot of the noise reduction as a function of temperature is shown in Figure 4.4.9. Microjet locations of one, two and three inches were studied. It was found that, for the cold jet, reductions near 5 dB were obtained when the microjets were placed at a radial distance of two inches. The amount of reduction at this location decreased with temperature. Another interesting feature of Figure 4.4.9 is the local maximum for

both the $r=1$ and 3 locations at a temperature of 600°F . For example, microjets at a radial distance of one inch are able to produce a reduction of over 5 dB. This local maximum behavior is likely due to the change in evolution of the shear layer at higher temperatures. Starting closer to the jet centerline (as is the case for the microjets at a radial distance of one inch) allows the microjets to penetrate farther into a thicker shear layer.

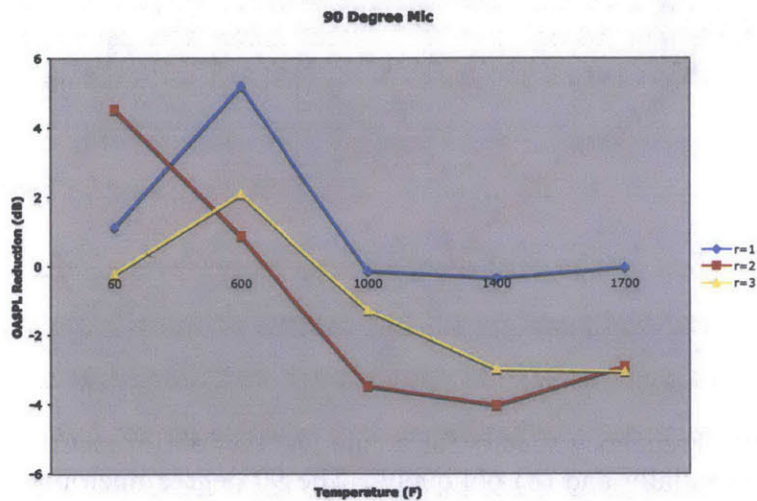


Figure 4.4.9: Summary plot of noise reduction as a function of temperature for water microjets at varying radial locations. For the cold jet, the most noise reduction is achieved at a radial location of two inches, while the most noise reduction for the jet at 600°F is produced with microjets at a radial location of one inch.

4.4.5 The Effect of Injection Angle

Another variable investigated through the course of this study was the injection angle of the microjets. Greska determined that the optimum injection angle of microjets at the nozzle exit is 60 degrees from the direction of exhaust. In his study, it was found that this angle allowed for the microjet to more effectively penetrate the shear layer by slipping between the convected Mach waves of the shear layer, parallel to their angle of propagation. This is not physically possible from the ground plane, as it would require either outward injection or injection into the ground plane. Neither of these options make physical sense. Therefore, as an alternative, an injection angle of 30 degrees from the ground plane normal was chosen, as it is perpendicular to the angle of the Mach wave radiation. In order to test the effect of injection angle on the microjets' ability to reduce noise, a series of tests was performed using oblique microjets at 30 degrees from the

normal and tangential microjets at 0 degrees from the normal. It was found that the tangential microjets did not produce appreciable reductions in the OASPL. However, conclusions may be drawn from the spectra obtained from these tests. The results are shown in Figure 4.4.10.

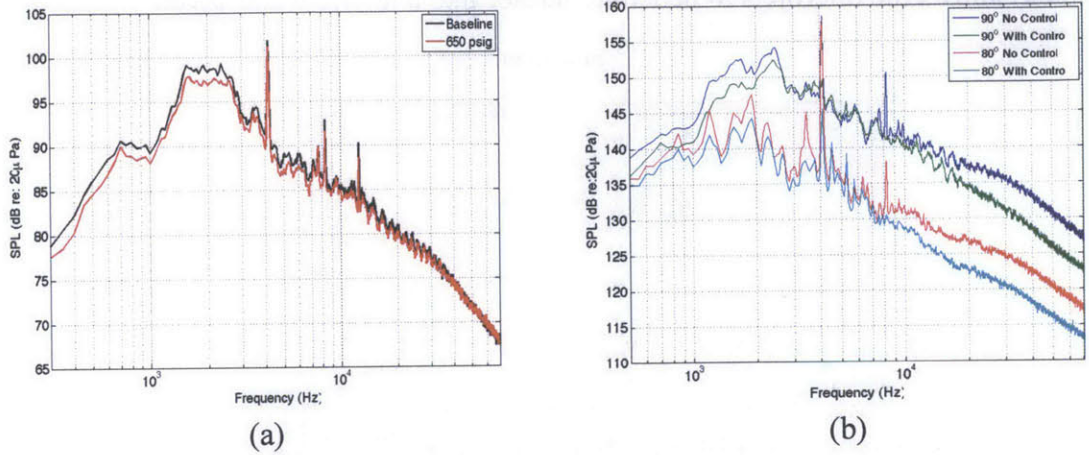


Figure 4.4.10: Frequency spectra for a cold jet at $h/d=8$ for microjets at $r/d=1.53$ firing (a) tangentially and (b) obliquely. The 90 degree microphone results are shown in (a) and demonstrate that lower frequency, turbulence-associated noise is reduced while leaving feedback tones and higher frequency, shock-associated noise in tact. Oblique microjets, on the other hand, reduce tones and spectral energy across all frequencies.

From this figure it can be seen that the tangential microjets are not effective in reducing feedback tones. This is due to the fact that, as they are injected tangentially, they are not able to penetrate the shear layer and break the feedback loop. They are also not capable of reducing the high-frequency, shock-associated noise, as shear layer penetration is required for this as well. They are, however, able to marginally decrease the lower frequency, turbulence associated noise, as some of the microjet fluid is broken away and swept into the shear layer. Once there, it acts as a momentum sink, reducing the shear layer vorticity as a result of its larger density.

As discussed earlier, oblique microjets, on the other hand, are capable of reducing feedback tones and high-frequency, shock-associated noise, as they are effective at penetrating the shear layer. They are also much more capable of reducing higher-frequency, turbulence-associated noise, as the microjet is able to penetrate the shear layer before it is broken up. Therefore, more fluid is conveyed to the shear layer where it can

more effectively be broken up into smaller and smaller droplets. These phenomena will be described in greater detail in section 4.5.

4.5 High-Speed Imaging and Noise Reduction Mechanisms

It has been shown so far that ground plane microjets are effective in producing noise reductions for various jet operating conditions. Traditionally, microjet injection at the nozzle exit has proven effective at inhibiting the growth of large-scale vortical structures in the shear layer, and thus reducing the effect of mach wave radiation. This is also effective at breaking the feedback loop in impinging flows and removing the feedback-associated tones. At higher flow rates, it has been shown that water microjets (due to their larger momentum ratios) are able to reduce the turbulence associated noise by reducing the vorticity of the main jet. The fact that such significant reductions have been shown in this study suggests that ground plane microjets are effective at reducing noise generated from these same sources. This section explores the mechanisms responsible for producing these reductions using high-speed imaging techniques.

Previous research has shown that lower frequency mixing noise of a free jet is reduced through the use of microjets and chevrons implemented at the nozzle exit. In reducing the microjet injection pressure (and thus flow rate), one can ensure that the microjet does not have sufficient power to penetrate the shear layer and initiate the streamwise vorticity needed to inhibit the growth of large-scale vortical structures. In this way, one can ensure that reductions achieved under these conditions are the result exclusively of the reduction of main jet turbulence. In his PhD thesis, Greska showed just this. Using low-pressure water jets, Greska was able to produce noise reductions manifesting themselves as a reduction of the low-frequency spectral energy, without shifting that energy to higher frequencies. This suggests that the breakup of the microjet into smaller and smaller droplets is responsible for the reduction in turbulence-associated noise. Previous studies have also shown that the large-scale vortical structures tend to develop favorably in the high-speed side of the shear layer. The growth of these structures is inhibited when the microjet (or chevron) is of sufficient strength to penetrate

the shear layer to the high-speed side and set up streamwise vorticity. This thus affects the higher-frequency, shock-associated noise source.

With respect to an impinging jet these mechanisms would manifest in a slightly different manner. The penetration depth of the coherent microjet (before full breakup) would indicate its ability to reduce high-frequency shock-associated noise. A deeper penetration of the microjet would imply larger reductions of high-frequency noise. The first indicator of the breakup of the microjet in the shear layer would be the presence of fine mist. This would suggest its breakup into smaller and smaller droplets, which would be responsible for reducing the lower-frequency, turbulence-associated noise sources. A summary of these two mechanisms with their respective regimes of effect is shown in Figure 4.5.1.

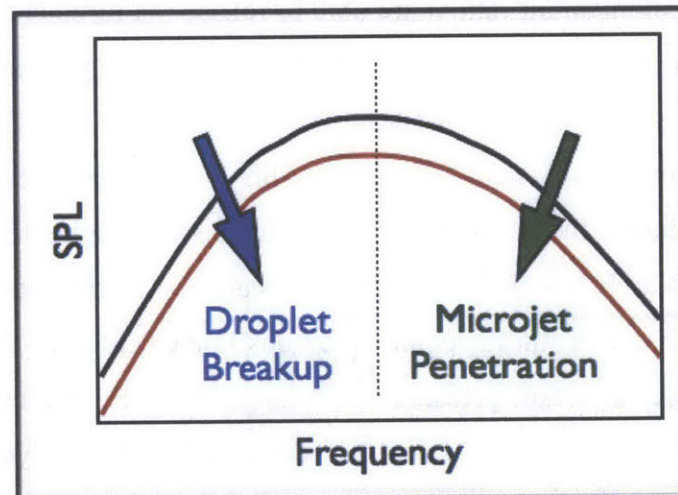


Figure 4.5.1: Simple schematic showing the two noise reduction mechanisms and their regions of impact with respect to the frequency spectrum. The breakup of the microjet into smaller and smaller droplets would be evidenced by the reduction of lower-frequency turbulence-associated noise, while the ability of microjets to penetrate into the shear layer would be evidenced by the reduction of higher-frequency, shock-associated noise.

In order to explore these noise reduction mechanisms more thoroughly, a set of experiments was performed in order to observe the interaction of the microjet with the shear layer of the main jet using high-speed imaging techniques. As described earlier, once the images were obtained they were analyzed in order to determine and quantify the amount of droplet breakup as well as the penetration ability of the microjet. Upon first inspection, several inferences can be made by comparing representative images at

varying microjet injection pressures to their corresponding noise reduction, as shown in Figure 4.5.2.

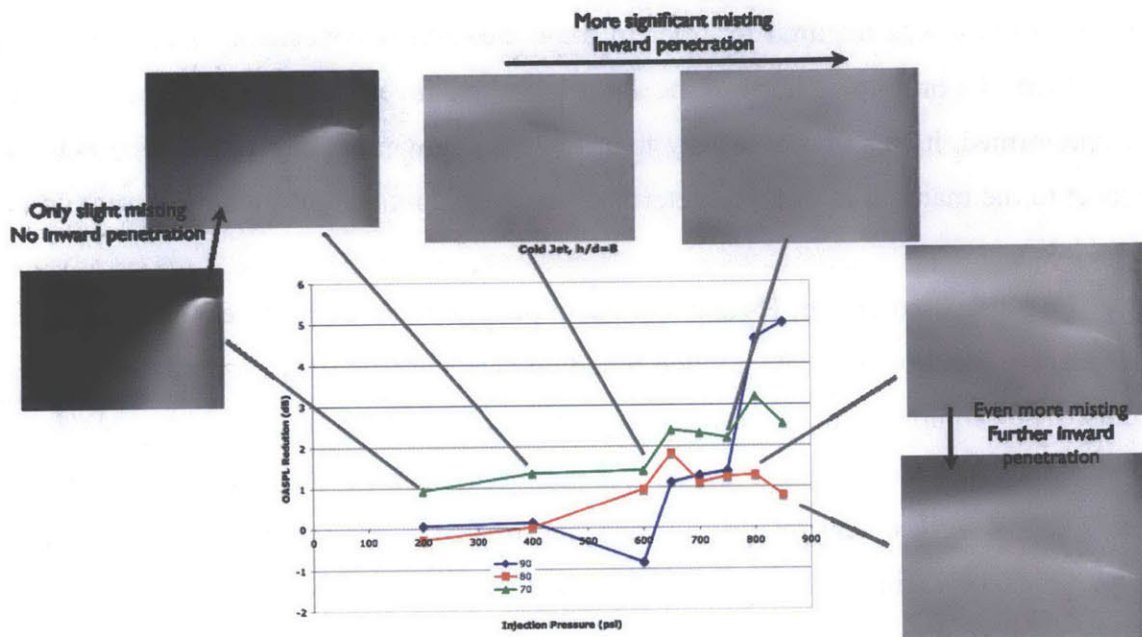


Figure 4.5.2: Comparison of the microjet behavior with the resulting noise reduction. At very low injection pressures there is only slight misting and no inward penetration. As the pressure is increased, the amount of misting increases. Also to be noted is the significant increase in both upstream and inward penetration depth of the microjet, especially at injection pressures above 700 psig.

From this figure, it can be seen that the amount of mist present increases as the injection pressure is increased. Interestingly, the mist does not exist within the shear layer until pressures at and upwards of 600 psig are achieved. This is due primarily due to the fact that the microjet is not strong enough at lower pressures to penetrate the shear layer. This can be seen by the fact that the microjet is deflected away from the main jet centerline when operating at injection pressures of 200 and 400 psig. Upon initial inspection, the upstream penetration of the microjet appears to grow with injection pressure. Also, in a corresponding manner, the inward penetration depth of the microjet also appears to grow with increasing pressure, though at 200 and 400 psig the inward penetration depth is actually negative – meaning that the microjet is deflected away by the wall jet along the ground plane before it has a chance to penetrate the shear layer. Above 400 psig, the microjet is able to effectively penetrate the shear layer, and its inward penetration depth increases with injection pressure.

The implications of Figure 4.5.2 are expected, however they do not fully account for the added reductions achieved at injection pressures above 750 psig. Therefore, further analysis was required in order to draw meaningful conclusions from the image data. First, the brightness level of the shear layer was investigated. Before any analysis was performed, it was first necessary to analyze the flow properties of the microjet with respect to the main jet in order to determine the breakup mode of the droplets within the shear layer.

As discussed earlier, Hsiang and Faeth performed an exhaustive study in order to characterize the droplet breakup mode based on characteristic flow properties of the two fluids. They compared the Ohnesorge number (which is a ratio of the fluid viscous forces to its surface tension forces) to the Weber number (which is a ratio of the fluid inertial forces to its surface tension forces), and constructed a chart indicating the different droplet breakup regimes. For convenience, the Ohnesorge and Weber numbers are given below.

$$Oh = \frac{\mu_l}{\sqrt{\rho_o d_o \sigma}}$$

$$We = \frac{\rho_g d_o u_o^2}{\sigma}$$

If the flow has a low Ohnesorge number (less than 1), the breakup regime is affected almost entirely by the Weber number. In such instances, low Weber numbers (less than 10) produce only droplet deformations. As the Weber number is raised, the droplet breakup regime progresses through the bag breakup regime, the multimode regime, and finally to the shear breakup regime. At larger Ohnesorge numbers, the Weber numbers required to advance through these regimes increase. Krothapalli et. al. showed that it was in this shear breakup regime that lower-frequency, turbulence-associated noise was affected. This was corroborated by Greska when using water microjets at the nozzle exit at very low injection pressures. Eliminating the microjets penetration ability guaranteed that noise reductions achieved were caused only by the reduction of turbulence as a result of the breakup of the microjet. Few of the parameters used to calculate these two numbers may be easily varied. The viscosity, surface tension and density, for example, may not be touched without changing the composition of the exhaust or changing the working microjet fluid. Therefore, essentially only the relative velocity between the two

fluids may be easily adjusted by changing the microjet injection pressure. To summarize, in order to ensure that the droplet breakup mechanism is in the shear breakup regime, one would need to increase the relative velocity of the fluid as much as possible. The range of Ohnesorge and Weber numbers in this study were calculated as shown in Table 4.5.1.

Table 4.5.1: Range of Ohnesorge and Weber numbers used in this experiment. All cases studied in the current research were well above those performed by Krothapalli et. al., and demonstrate that, for all cases, the droplet breakup was of the shear variety.

Run Condition	Reynolds Number $Re = \frac{\rho_g u_o d_o}{\mu_g}$	Ohnesorge Number $Oh = \frac{\mu_l}{\sqrt{\rho_o d_o \sigma}}$	Weber Number $We = \frac{\rho_g d_o u_o^2}{\sigma}$
Cold	4440	9.18×10^{-3}	471
1700°F	8910	9.18×10^{-3}	1897

The low value of the Ohnesorge number, being much less than 1, suggests that the droplet breakup regime is only affected by the magnitude of the Weber number. For the full range of experiments presented in the current study, the Weber numbers found show that the droplet breakup is always within the shear regime. Therefore, the presence of fine mist in the shear layer is evidence that the microjet is breaking up as a result of the shear forces in the fluid there. This breakup is directly a result of the reduction of shear layer turbulence and, therefore, its associated noise. In other words, the turbulence energy in the shear layer is transferred to the new surface energy of the droplets as they break up, as well as their inertial energy (a result of the thousand-fold difference between the density of the main jet exhaust and the water used in the microjets).

The next step in the misting analysis was to examine the amount of mist within the shear layer for each case. In each image, the shear layer region of the main jet was isolated, and an average pixel value was calculated. This pixel value is proportional to the amount of fine mist in the shear layer, which corresponds to the reduction of shear layer turbulence. The average pixel value of the shear layer is plotted as a function of time for each injection pressure in Figure 4.5.3.

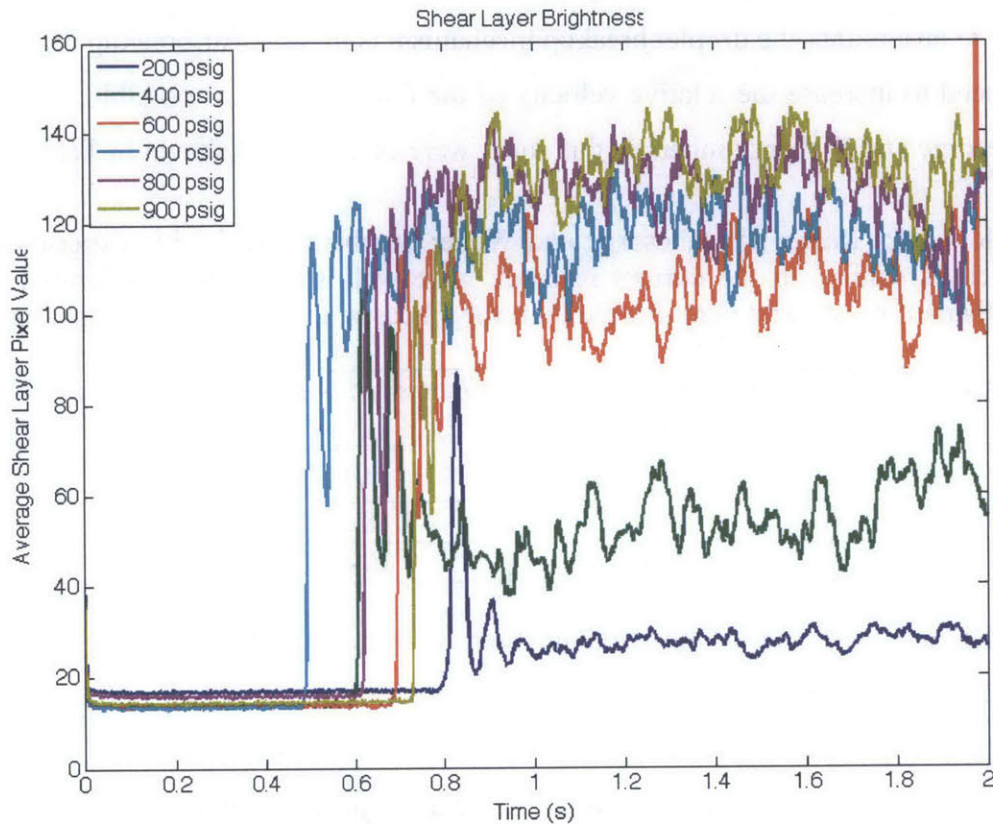


Figure 4.5.3: Plot of average pixel value as a function of time for each microjet injection pressure. Each plot shows an initial period before the firing of the microjet, followed by a period of microjet firing. As expected, the average pixel value increases with injection pressure with an apparent plateau effect.

For each microjet injection pressure, the signal begins with a period before the microjet is fired. Then the microjet is fired some time before one second, and the remaining portion of the signal corresponds to where the microjet is firing. As soon as the microjet is fired there is a short transient section followed by a steady-state section. This transient section is more pronounced at the lower pressures, as evidenced by the large overshoot spike. This can be seen especially for the 200 and 400 psig injection cases. The overshoot is no longer apparent at injection pressures at and above 600 psig. As the pressure is increased, the average shear layer pixel value seems to approach a value between the 140 and 150 brightness levels (on a scale of 0-255, where 255 corresponds to the brightest pixel value). In order to view this behavior more clearly, the average value over the last second of microjet firing was computed. The computed time-averaged brightness value is shown as a function of injection pressure in Figure 4.5.4.

The time-averaged shear layer pixel value for low-pressure injection is just below 30 (corresponding to the 200 psig injection case), which is only about 10 higher than the non-firing value of about 18. The value increases quickly with microjet injection pressure, climbing to 55 for the 400 psig case and 105 for the 600 psig case. At pressures above 600 psig, however, it can be seen that the amount of misting in the shear layer, as indicated by the pixel value, begins to plateau. It appears that increasing injection pressure beyond 900 psig (this case corresponds to a pixel value of approximately 133) would achieve insignificant further gains, where a maximum attainable pixel value would be between 140 and 150. It should be noted here that the average pixel value is being used as a surrogate quantity for the amount of misting in the shear layer, since the actual droplet counts cannot be computed from the video data obtained in this study. The pixel value is, however, an indication of the amount of mist within the shear layer, and therefore, an indication of the breakup of the coherent microjet into small droplets within the shear layer.

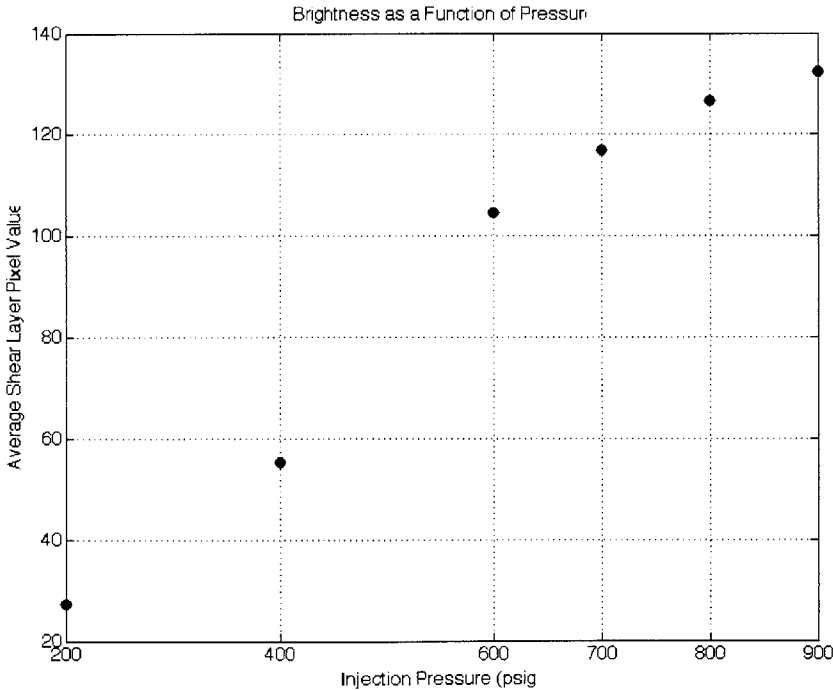
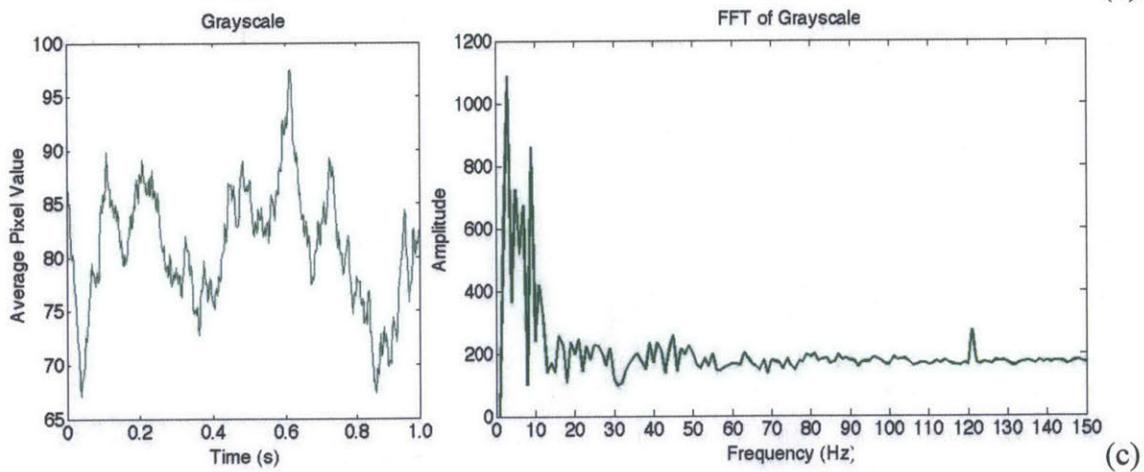
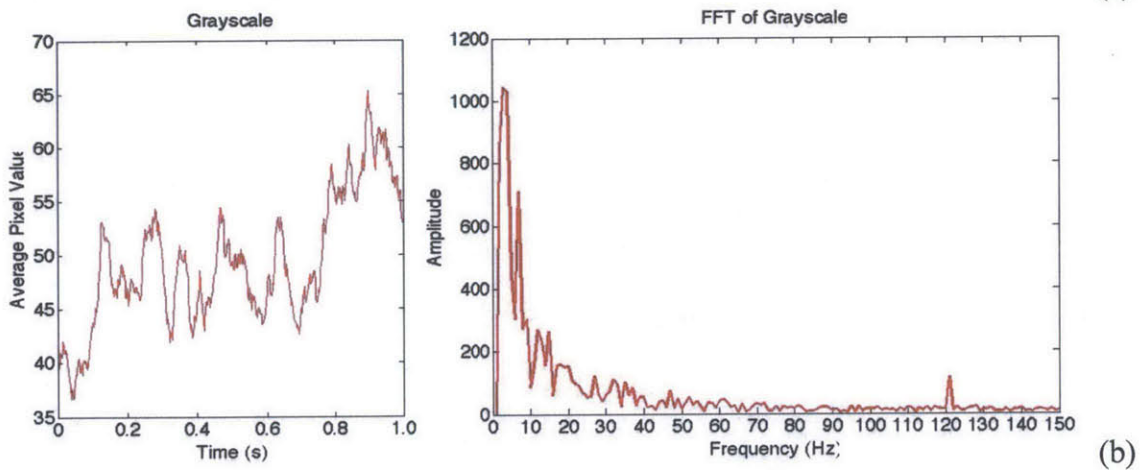
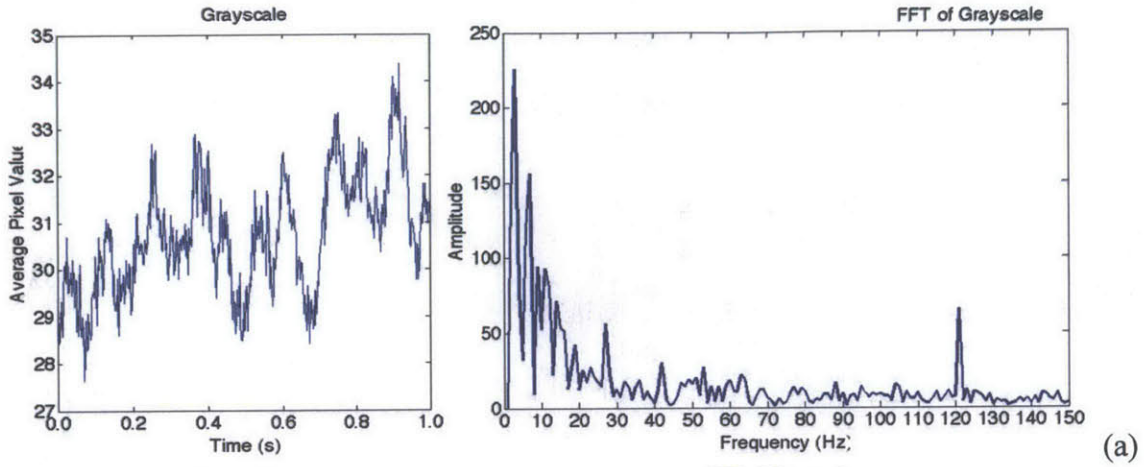


Figure 4.5.4: Average shear layer pixel value as a function of injection pressure. The plateau effect that was inferred from the time signals is clearer here. Increases in farfield noise reduction are partially a result of the increase in shear droplet breakup.

This plateau behavior has been seen in many other instances with respect to microjet injection. Greska demonstrated, for example, that one could achieve nearly 10 dB of noise reduction using microjets at the nozzle exit at momentum ratios over 12. However, no additional gains could be obtained by increasing the momentum ratio any further. In this case, the shear layer, being a restricted geometric location, can only hold so much water. The wall jet would simply wash away any additional water pumped into the shear layer by the microjet.

This hypothesis is corroborated through inspection of the videos accompanying this thesis. As the microjet pressure is increased, the exit velocity of the jet, and therefore the volumetric flow rate of the jet, is increased. The microjet interacts with the shear layer of the jet in complex ways, and the depth is influenced significantly by slower, flapping modes of the main jet. The flapping of the jet can be observed visually, as well as analytically, from the videos – especially when the microjet is operated at higher pressures. As the jet flaps down toward the microjet, the microjet penetrates the shear layer and is eventually broken down into a fine mist consisting of small droplets. These droplets accumulate in the shear layer until the jet flaps back up away from the microjet, at which time the wall jet washes away the mist.

Since the brightness is affected by the amount of mist in the shear layer – which is affected by the flapping of the jet – the frequency of this phenomenon can be determined by performing the Fast Fourier Transform on the brightness level of the shear layer, as shown in Figure 4.5.5.



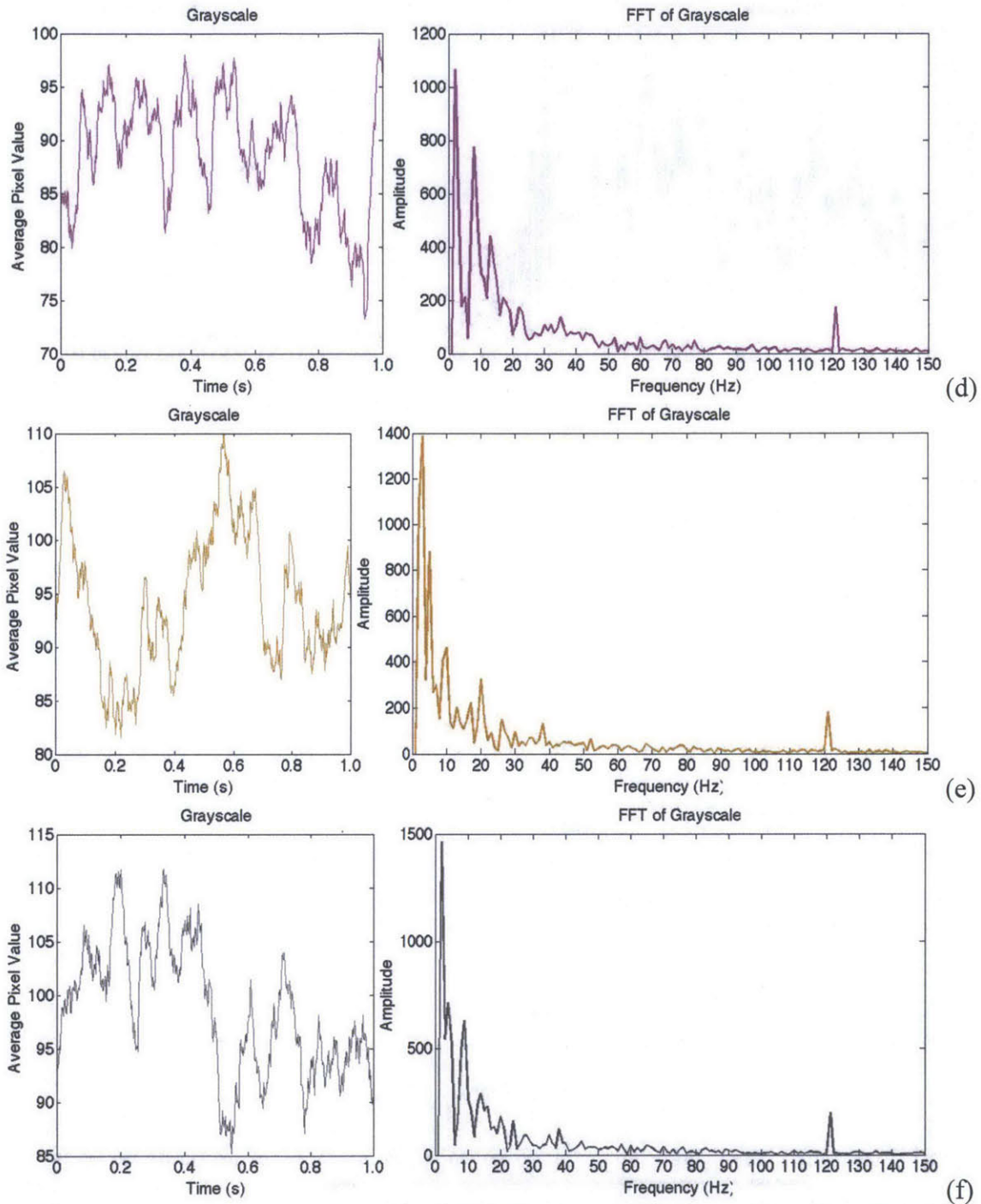


Figure 4.5.5: Zoomed shear layer brightness and corresponding Fast Fourier Transform. Results are given for a microjet operating at (a) 200 psig, (b) 400 psig, (c) 600 psig, (d) 700 psig, (e) 800 psig and (f) 900 psig. All of the FFT plots show an initial large peak at 1-2 Hz, followed by a secondary peak at 7-9 Hz. Based on the video data, the second peak corresponds to the rate of jet flapping, wherein the accumulated shear mist is cleared away before the process repeats.

It can be seen from this figure that, for each microjet operating pressure, there is an initial large peak at 1-2 Hz followed by a secondary peak at 7-9 Hz. The second peak corresponds to the flapping of the jet. This can be verified visually by the video data, since the flapping mechanism causes accumulated mist in the shear layer to be carried away as the jet flaps away from the microjet origin. In each of the FFT plots there is also a small peak near 120 Hz. This however is simply an artifact of the 60 Hz alternating current present in the lab, and was verified by comparing the FFT of the video without the microjet running.

Also observable from the accompanying videos, is the fact that the jet breaks up within the shear layer when the pressure exceeds 600 psig. At these high pressures, large water droplets are sheared apart and trapped in the recirculation region of the jet. This region takes ejected particles and returns them to the shear layer near the nozzle exit. Therefore, while no control is actively implemented at the nozzle exit, there is an effective circumstantial control in this region that is capable of significantly affecting the development of the shear layer.

In his PhD thesis, Greska demonstrated that, through the use of low-pressure water jet injection at the nozzle exit, reductions in noise could be produced [3]. In his study, the 100 psig water jets were able to produce low-frequency reduction. However, there was a crossover in the spectrum where, at very high frequency, the noise was increased. This result is reproduced in Figure 4.5.6. He attributed this to the water jets' inability to penetrate the high-speed side of the shear layer. As such, he attributed the low-frequency noise reduction to the droplet breakup effect discussed by Krothapalli et al [4].

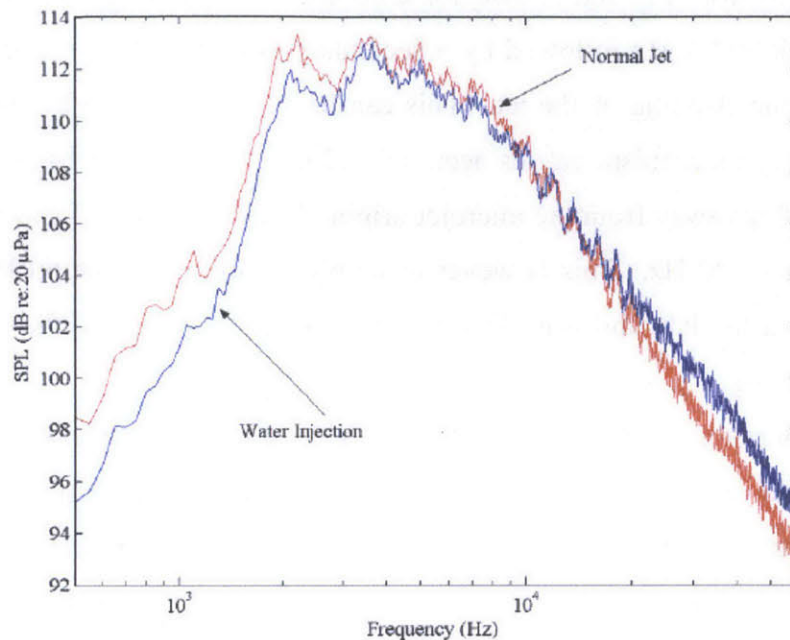


Figure 4.5.6: Narrowband spectra for water injection at 100 psig, as reproduced from Greska [3].

Krothapalli et al discussed the effects of the breakup of the microjet on the properties of the main jet [4]. Outside of the injection region, they showed that no appreciable difference to the mean flow structure was observed. However, they did show that the mean turbulence profiles were reduced through the use of water jets – this effect was attributed to the droplet breakup process. This result corroborates similar reductions in turbulence for particle-laden flows [5]. In addition, at the sideline angle of 90 degrees, they showed reductions in both near and farfield jet noise that corroborate the results obtained by Greska [3].

In the nearfield, results show a reduction along all frequencies. However, in the farfield, results show reduction of lower frequencies with no significant changes at high frequencies. They attribute this to the reduction of large-scale mixing – with which water injection “appears to interfere constructively,” and that this interference results in SPL reductions at low frequencies.

One point of confusion so far is why past studies have attributed a reduction in large-scale, low-frequency mixing noise with a droplet breakup effect. Krothapalli et al [6] showed, through the use of PIV and shadowgraph imaging, that these large-scale

phenomena are reduced in size and strength by entrained, atomized water droplets. Therefore, their contribution to the overall noise levels may be reduced.

To summarize, Greska demonstrated that, with low pressure microjet injection at the nozzle, where essentially all noise reduction was the result of the breakup of the microjet in the shear layer of the main jet since it lacked the strength to penetrate the shear layer effectively and set up streamwise vorticity, low-frequency, turbulence-associated noise was reduced. This was accomplished through the reduction in size and strength of larger scale structures in the shear layer, thus producing a reduction of lower frequency noise (that is, for the case of the experiments in this study, frequencies lower than 2 kHz) in the frequency spectra. A simple summary schematic of this effect is shown and highlighted in Figure 4.5.7.

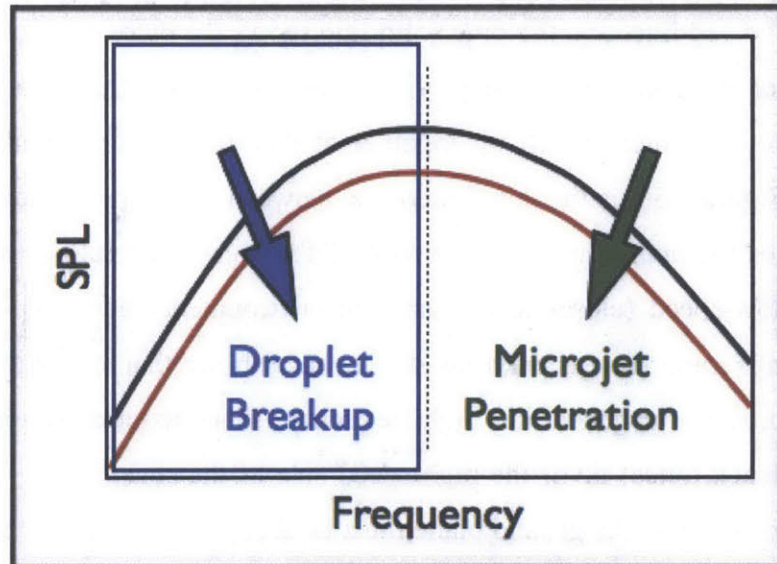


Figure 4.5.7: Schematic of the effect of the droplet breakup mechanism on the frequency spectra. The lower frequency, turbulence-associated noise is reduced by the shear breakup of the microjet. This is evidenced by the presence of fine mist within the shear layer of the jet.

The next step of the high-speed image analysis was to determine the effect of the penetration depth of the coherent microjet on the high-frequency, shock-associated noise. The shear layer of the main jet can be said to grow linearly with downstream axial distance from the nozzle exit. The region bounded internally by the shear layer is known as the potential core, and is defined as where the bulk fluid velocity is equal to 99% of

the exhaust velocity of the main jet. The growth rate of the shear layer, and therefore, the length of the potential core, is dependent upon the temperature and velocity of the main jet, as well as the temperature of the ambient environment. The relationship is given empirically as

$$\frac{x}{d} = 3.134e^{(1.043M_j - M_c)}$$

where M_j is the Mach number of the main jet and M_c is the convective Mach number, as given by

$$M_c = \frac{U_j - U_\infty}{a_j + a_\infty}.$$

For the cold jet case, this produces a potential core length of 7.81 nozzle throat diameters. The boundaries of the shear layer are shown in Figure 4.5.6 below. The thick dashed line shows the jet centerline. The boundary between the shear layer and the potential core is given by the solid red line, and the blue solid line shows the outer boundary of the shear layer (this outer boundary is actually visible by inspection from the shape of the brightness contours, which bunch up together at the shear layer boundary). Also of importance in Figure 4.5.8 is the thin dotted line between the two shear layer boundaries. This line denotes the approximate delineation of the high-speed (closer to the potential core) and the low-speed (closer to the ambient environment) sides of the shear layer. This delineation is important, as previous studies have shown that the large-scale, vortical structures responsible for generating high-frequency, shock-associated noise (as well as generating feedback tones) favor the high-speed side of the shear layer. Therefore, any control technique used on the ground plane must be able to penetrate past this point in the shear layer to be able to effectively control this noise source.

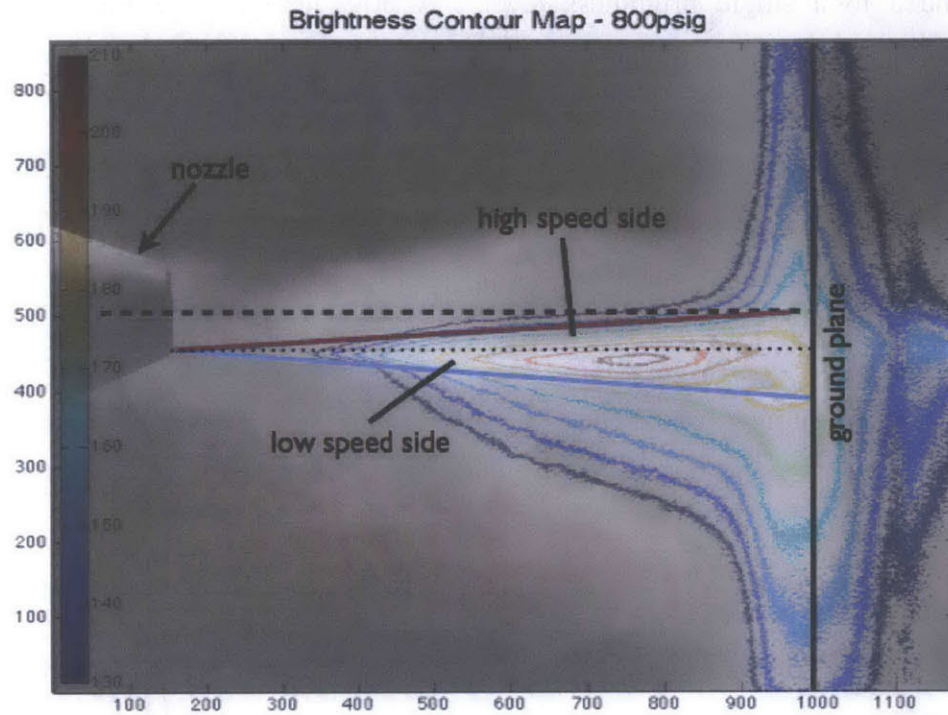


Figure 4.5.8: Contour plot overlaid on a sample high-speed image showing the different regimes of the shear layer. The shear layer can be said to grow linear with axial distance. The blue line indicates the location of the outer boundary of the shear layer, and can be seen in the contour plots. The red line indicates the inner boundary. This line shows the outer bounds of the jet potential core. The fine dotted line delineates the high speed side of the shear layer (closest to the potential core) from the low speed side, while the thick dashed line represents the jet centerline.

In order to explore the effects of the microjet penetration depth on noise reduction, further analysis was required. The goal of this analysis was to examine the geometric bounds of the coherent microjet – that is, to determine the extent to which the microjet penetrated the shear layer prior to breaking up into small droplets. When viewing the videos of the microjet’s interaction with the shear layer, a simple visual inspection of this behavior is near impossible.

As the flapping phenomenon occurs periodically, the penetration depth is apparently also periodic. Therefore an algorithm was designed to determine a time-averaged geometry of the coherent microjet. The last 500 images for each run condition were averaged together to produce a single, time-averaged image. Then, Matlab was used to generate contours on each of these time-averaged images. Each contour

corresponded to a single brightness level. A brightness of 180 was identified as corresponding well with the boundary of the coherent microjet (prior to breakup). This can be seen from the overlay of the contours with the sample image in Figure 4.5.8. The geometric bounds of the 180 brightness contour were then determined. The brightness contour plot for the microjet operating at 200 psig is shown in Figure 4.5.9. The ground plane and nozzle boundaries are shown for the reader's reference as well.

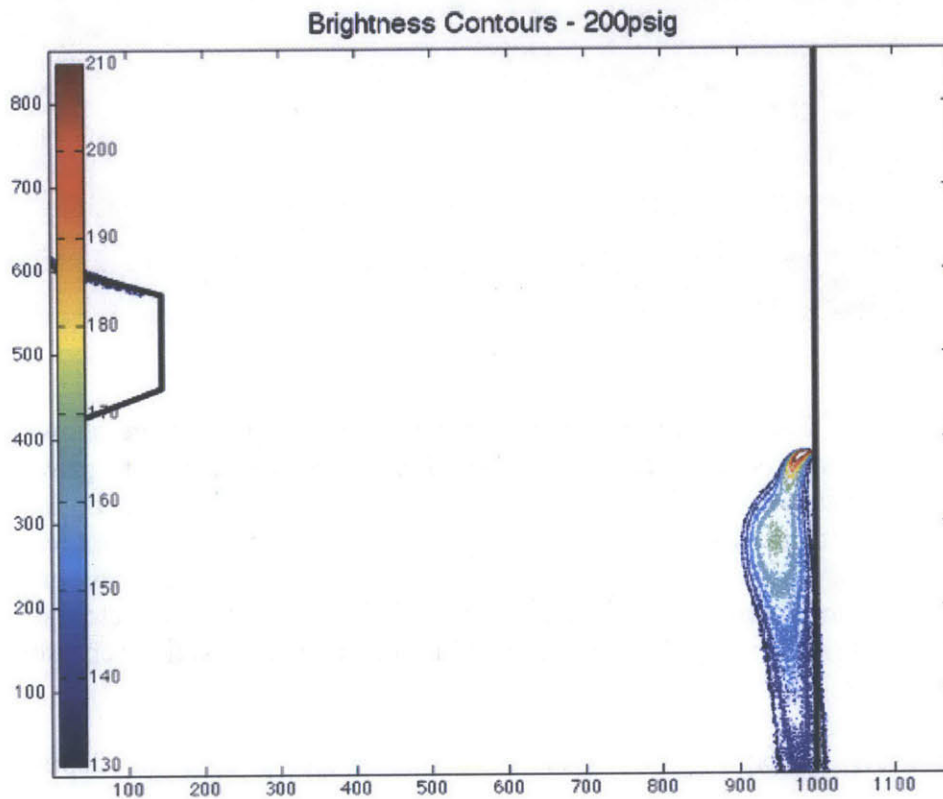


Figure 4.5.9: Brightness contour plot for the microjet operating at 200 psig. The upstream penetration is extremely small and the inward penetration is in the opposite direction, indicating a negative penetration.

From Figure 4.5.9 it can be seen that the low-pressure microjet has little penetrative ability. The microjet is able to penetrate only minimally upstream. From the contours associated with lower brightness, that is the blue contours, it can be seen that the microjet is deflected away from the jet centerline by the wall jet produced by the main jet. The microjet operating at 200 psig simply does not have the power required to penetrate the shear layer in any meaningful way.

The brightness contour plots for the microjet operating at 400, 600, 700 and 800 psig are shown in Figure 4.5.10. In Figure 4.5.10(a) it can be seen that, again, the 400 psig microjet has little power with respect to penetrating the shear layer in any meaningful way. It is able to penetrate upstream much more effectively than the 200 psig microjet. However, it is also swept away by the wall jet before it is able to penetrate inward at all. For both the 200 and 400 psig microjet (corresponding to Figure 4.5.9 and Figure 4.5.10(a) respectively), the inward penetration of the microjet is actually in the negative direction. That is to say that the microjet is not actually able to penetrate inward, but is instead swept away by the wall jet.

A positive inward penetration depth is seen first in the case of the microjet operating at 600 psig, as shown in Figure 4.5.10(b). The microjet in this case is strong enough to penetrate a small distance into the shear layer and produces a small positive inward penetration. It is also capable of penetrating much farther upstream than the previous two cases. At injection pressures of 700 and 800 psig, corresponding to Figure 4.5.10(c) and 4.5.10(d) respectively, the strength of the microjet increases. Even greater upstream penetration depths are achieved. The microjet operating at 700 psig is able to penetrate upstream 3.7 nozzle throat diameters, while the microjet operating at 800 psig is able to penetrate upstream 4.7 nozzle throat diameters. Inward, the microjet operating at 700 psig is able to penetrate inward nearly 0.6 nozzle throat diameters, while the microjet operating at 800 psig is capable of penetrating inward 0.75 nozzle throat diameters.

Another feature of Figure 4.5.10 is the increase in number of contours as the injection pressure is increased. This is an artifact of the presence of more mist in the shear layer at increased injection pressures. Also, as the strength of the microjet increases, its brightness also increases. The smoothing of the contour is also a result of the time-varying behavior of the main jet. That is to say, the flapping of the jet causes the microjet to interact with the shear layer in ways that vary with time. This interaction causes the contours to smooth. Also, as stated earlier, the outer boundary of the shear layer can be seen from these plots where the contours bunch up together. This phenomenon is first seen for the 600 psig microjet case, and can be seen for the cases

involving microjets operating at 700 and 800 psig as well. The outer boundary of the shear layer is not visible from the plot of the 400 psig microjet.

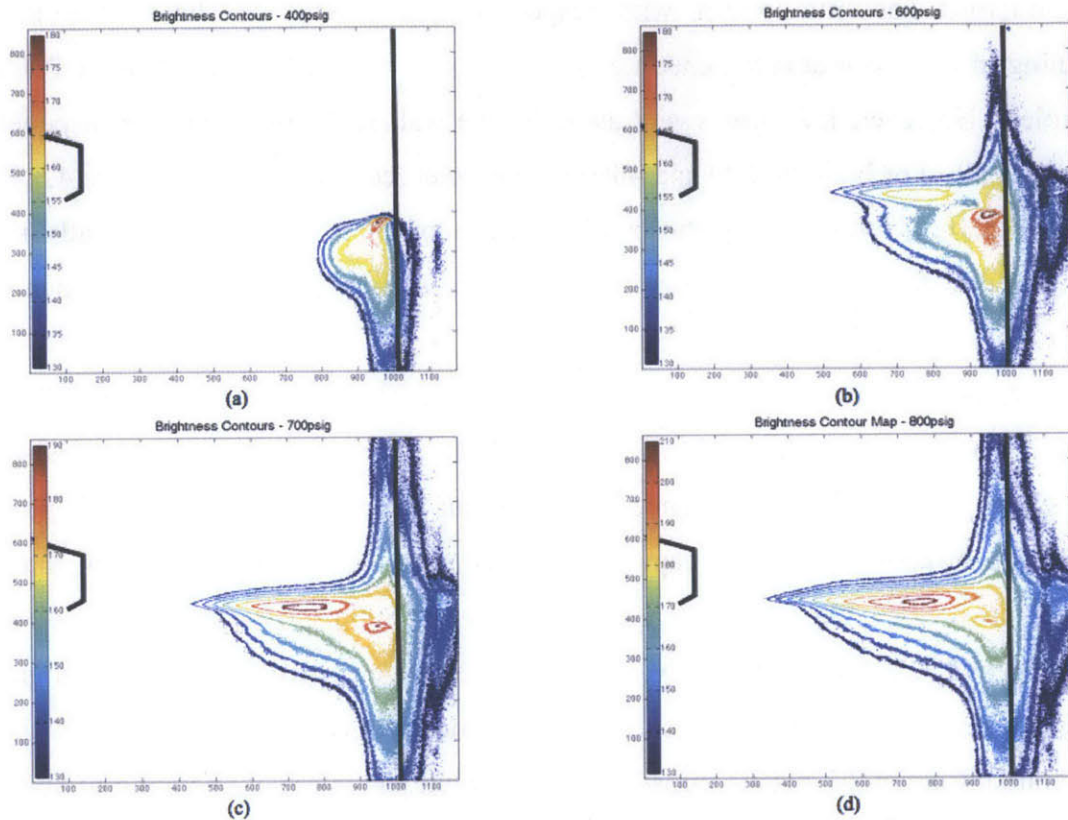


Figure 4.5.10: Brightness contour plots for a microjet operating at (a) 400 psig, (b) 600 psig, (c) 700 psig and (d) 800 psig. The upstream penetration depth increases as the injection pressure is increased. The inward penetration for the 400 psig microjet is still in the opposite direction, indicating a negative depth. However, above 600 psig, the microjet is able to penetrate inward into the shear layer, indicating a growing positive depth.

Finally, the brightness contour plot for the microjet operating at 900 psig is shown in Figure 4.5.11. The outer boundary of the shear layer is most apparent from this figure, as the brightness contours bunch up clearly on each other. The microjet operating at 900 psig is shown to have the most effective penetration ability. It is able to penetrate upstream 4.9 nozzle throat diameters, and is able to penetrate inward 0.6 nozzle throat diameters. This figure also shows the largest number of brightness contours – a result of the highest level of brightness of the coherent microjet, as well as the presence of the most amount of mist in the shear layer, as discussed in the mist analysis earlier.

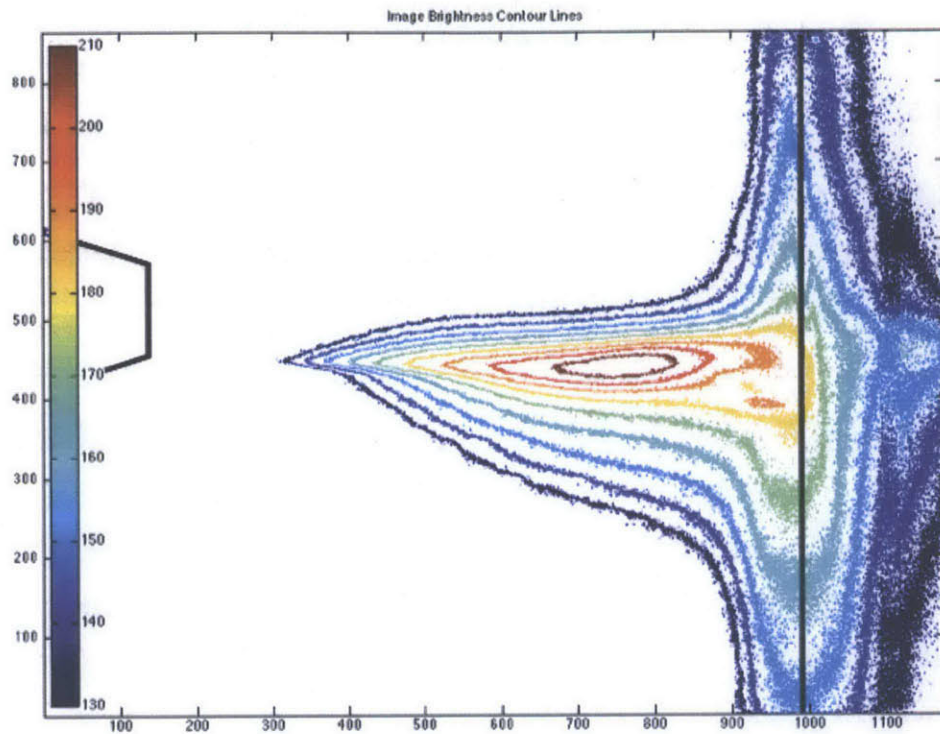


Figure 4.5.11: Brightness contour plot for a microjet injection pressure of 900 psig. The upstream and inward penetration depths are highest for this case. The brightness contour associated with 180 (yellow) demonstrates a large area of coherent microjet influence.

To better observe the upstream penetration trend of the microjet operating at varying injection pressures, Figure 4.5.12 shows the inward penetration depth as a function of injection pressure. At injection pressures of 600 psig and below, very little upstream penetration is achieved by the microjet. This is clear from the contour plots as well as through visual inspection of the unprocessed video data. At these pressures, the upstream penetration depth is less than one nozzle throat diameter. However, a very large increase in upstream penetration depth is achieved for the microjet operating at 700 psig. This is also apparent from the brightness contour plots. Another plateau effect is observed at pressures above 600 psig. It appears as though the maximum upstream penetration depth would approach approximately 5.5 nozzle throat diameters. Increasing the pressure above 900 psig would see only minimal returns above what is already achievable. The microjets operating at 800 and 900 psig were able to penetrate upstream 4.7 and 4.9 nozzle throat diameters respectively.

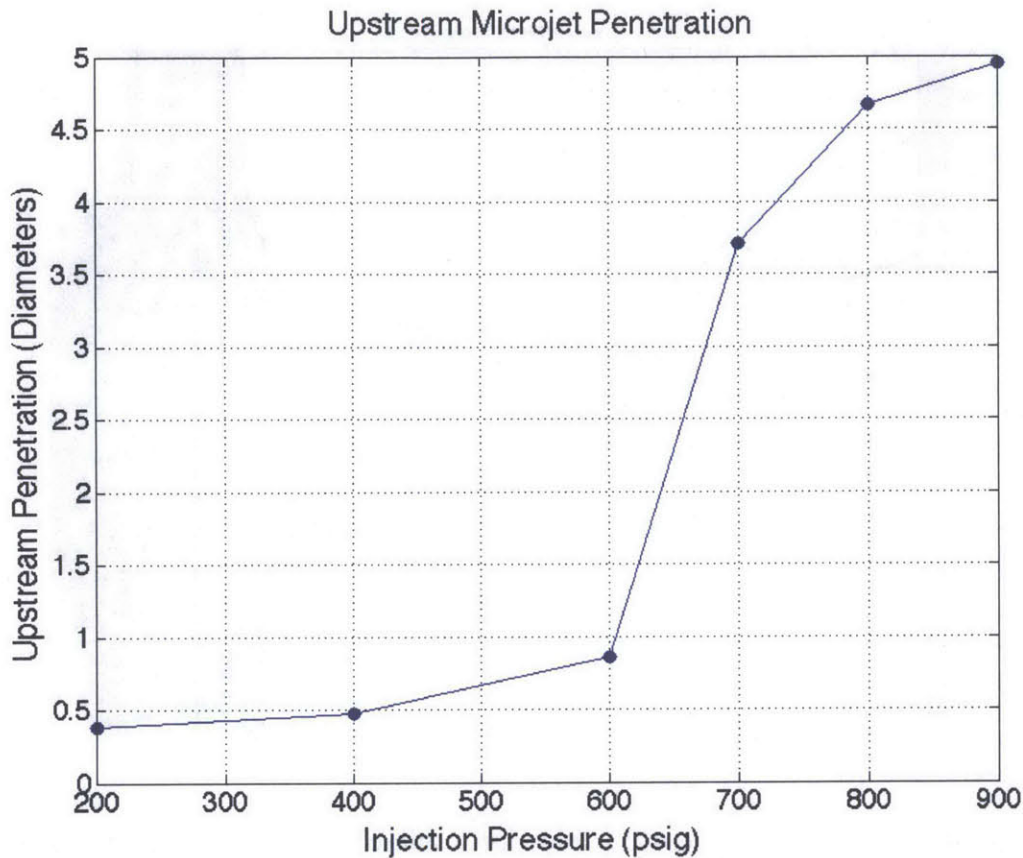


Figure 4.5.12: Upstream penetration depth as a function of microjet injection pressure. Interestingly, at injection pressures at 600 psig and below penetrate less than one nozzle diameter upstream. This is due to the weakness of the microjet at these lower pressures. A drastic increase in upstream penetration is shown, along with a plateau effect at injection pressures above 600 psig.

The behavior seen in Figure 4.5.12 is likely partially responsible for the increased misting in the shear layer seen at higher injection pressures as well. Unable to penetrate far upstream, the weaker microjets simply lack the power required to convey the working fluid (in this case water) to the shear layer.

While there is a drastic increase in upstream penetration depth at higher injection pressures, this particular quantity doesn't fully explain the large increase in noise reduction for the higher injection pressures as seen in Figure 4.4.4 and Figure 4.5.2. It is therefore necessary to take a closer look at the inward penetration depth of the microjet at varying injection pressures. The inward penetration depth – that is, the depth radially inward toward the jet centerline reached by the microjet – is plotted as a function of microjet injection pressure in Figure 4.5.13 below.

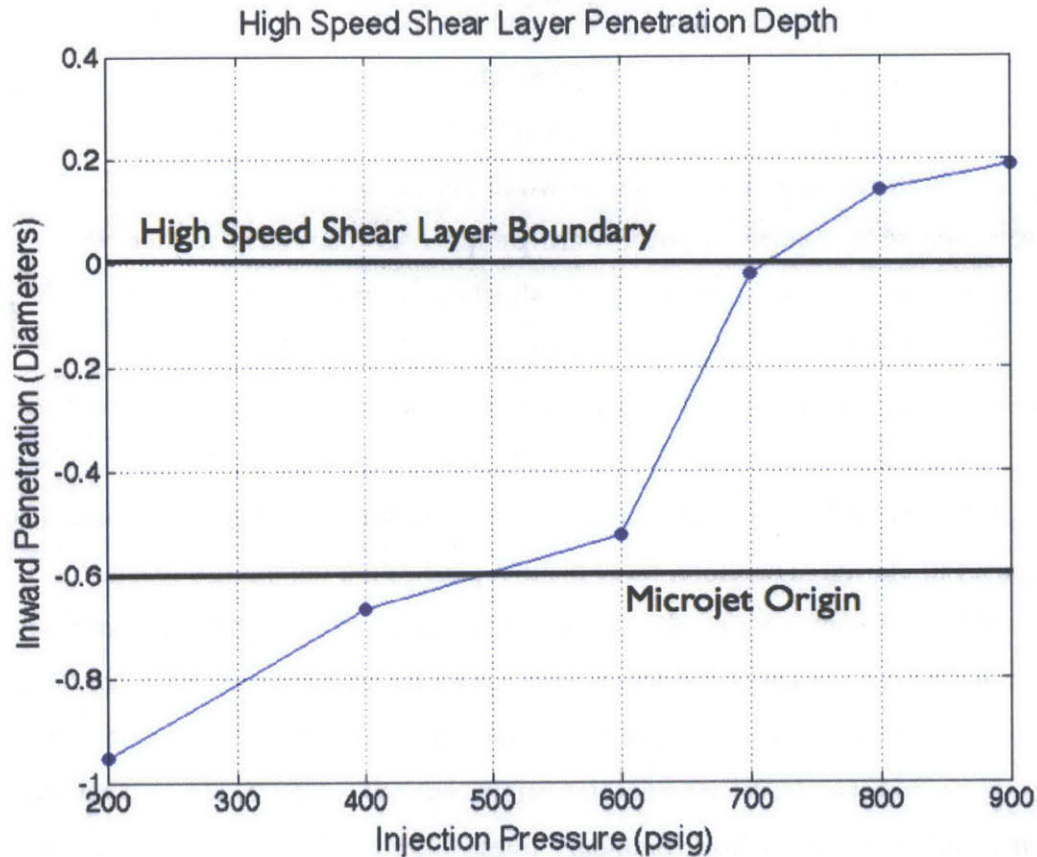


Figure 4.5.13: Inward penetration depth as a function of microjet injection pressure. The inward location of the microjet origin and the location of the high-speed shear layer boundary are marked. At 200 and 400 psig, the inward penetration depth is negative, suggesting that the microjet is swept away by the wall jet. At 600 and 700 psig the microjet penetrates inward into the shear layer, but falls short of the high-speed side. Above 700 psig the microjet penetrates past the high-speed shear layer boundary.

The microjet origin is indicated for reference on Figure 4.5.13 at a radial location of -0.6 nozzle throat diameters. As seen in Figures 4.5.9 and 4.5.10(a), low-pressure microjets are not able to penetrate inward, but instead are washed away by the wall jet. For this reason, the inward penetration depth is shown below the line indicating the microjet origin. At 600 psig, it was seen in Figure 4.5.11(b) that the microjet is strong enough to penetrate radially inward to the shear layer producing a positive penetration depth. This is shown also on Figure 4.5.13 by the point just above the microjet origin line. As with the upstream penetration depth, there is a significant increase in inward penetration depth above 600 psig. The microjet at 700 psig is able to penetrate inward

0.6 nozzle throat diameters, while the 800 and 900 psig microjets are able to penetrate 0.75 and 0.79 nozzle throat diameters respectively.

Alone, this behavior is not able to fully explain the additional noise reduction achieved for high-pressure injection as shown in Figure 4.4.4 and Figure 4.5.2. However, here we come to a nuance of the inward depth. As mentioned earlier, the vortical structures associated with high-frequency, shock-associated noise favor the high-speed side of the shear layer. Also, any technique used to effectively reduce the noise generated from this source must be able to reach this location in the shear layer. For this purpose, the location of the boundary between the low- and high-speed sides of the shear layer is indicated on Figure 4.5.13 as well. This location is defined as the radial origin for purposes of clarity. Therefore, three distinct penetration regions are reached in Figure 4.5.13. Microjets that are not able to penetrate the shear layer are shown below the microjet origin line, which is located at -0.6 nozzle throat diameters, and have negative values. Microjets that are able to penetrate the shear layer but do not reach the high-speed side are shown above the microjet origin, but still in have negative values (that below the high-speed shear layer boundary line). Microjets that are powerful enough to reach the targeted high-speed side of the shear layer fall above the high-speed shear layer boundary line, and have positive values. As can be seen from Figure 4.5.13, the microjets operating at 800 and 900 psig both meet this criterion. Both of these points correspond with the points in Figure 4.4.4 and Figure 4.5.2 associated with additional noise reduction. The 800 and 900 psig microjets' ability to reach the high-speed side of the shear layer is attributed to their increased effectiveness at reducing farfield noise associated with high-frequency, shock-associated structures.

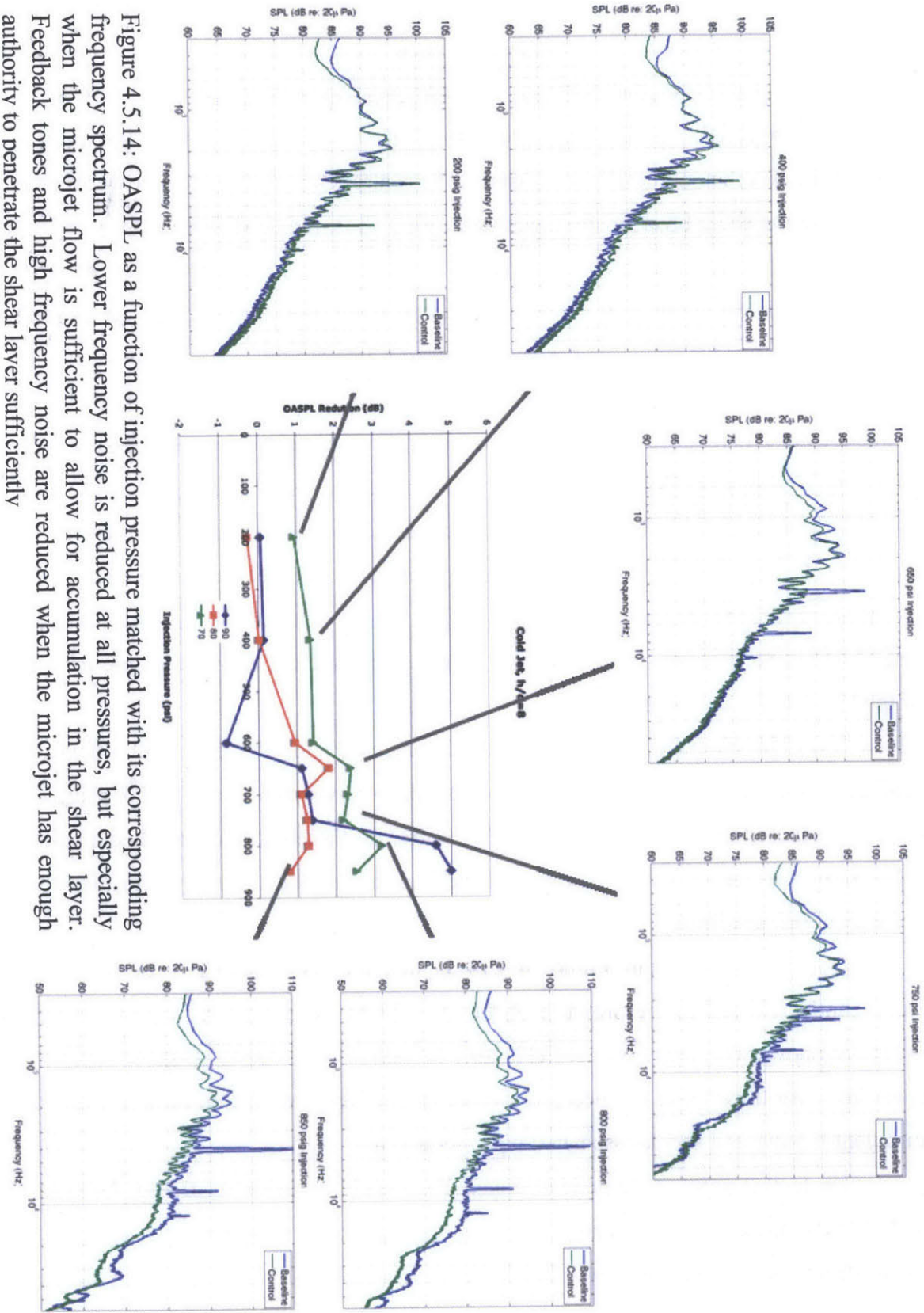


Figure 4.5.14: OASPL as a function of injection pressure matched with its corresponding frequency spectrum. Lower frequency noise is reduced at all pressures, but especially when the microjet flow is sufficient to allow for accumulation in the shear layer. Feedback tones and high frequency noise are reduced when the microjet has enough authority to penetrate the shear layer sufficiently

To further establish this point, the OASPL value as a function of pressure is represented in Figure 4.5.14. Along with each point of interest is a corresponding frequency spectrum. For the 200 psig and 400 psig cases, the feedback tones are not significantly reduced. As seen from the videos and selected images of the microjet, this is due to the fact that, at these low pressures, the control does not have the power required to penetrate the shear layer in any meaningful way. It is, rather, deflected away from the centerline by the shear layer and wall jet of the main jet. Also, at these low pressures, there is actually an increase in the high-frequency shock associated noise. At these low pressures, the microjet actually interferes constructively with this noise source.

It can also be seen from this figure that, even for microjets at low pressures, lower frequency noise is reduced. This effect increases as the microjet injection pressure is also increased. This is verified by observations from the videos, which suggest that, as the pressure increases, the volumetric flow rate and exit velocity of the microjet also increase. This increased water volume allows for the accumulation of water droplets in the shear layer. This accumulation is responsible for the reduction in size and strength of large-scale vortical structures in the shear layer. These sources are responsible for much of the low-frequency spectral content.

More importantly, as the pressure is increased to 650 psig and above, the feedback tones are more effectively suppressed. Above pressures of 750 psig, little remains of these tones. The authority of the control for these cases has reached a point so as to allow the microjet to penetrate sufficiently far into the shear layer to effectively break the feedback loop.

One final note from Figure 4.5.14 is that the high frequency noise is more significantly reduced as the pressure of the microjet is increased. As shown earlier, at pressures above 800 psig, the microjet is able to penetrate into the high-speed side of the shear layer for these cases – a necessary requirement for the reduction of high-frequency turbulent mixing and shock-associated noise reduction.

Up to this point, only general conclusions could be made regarding the spectral and OASPL reductions specifically attributed to large-scale, turbulent mixing noise, and higher-frequency, shock-associated Mach wave radiation. In order to more carefully isolate the reduction in OASPL due to Mach wave radiation, the skewness of the

pressure-time signal is presented. Previously, this metric has been used only as an indicator of the presence of the crackle in the jet. Skewness levels above 0.4 indicate that crackle is indeed present, while values below this value are inconclusive.

Since Mach wave radiation and crackle are within the same family of noise generation – that is, high-intensity ballistic shock waves – crackle can be used as a comparative metric to quantify the relative amount of suppression of the Mach wave radiation noise source. It is computed from the pressure-time signal and its standard deviation as follows:

$$k = \frac{\langle p^3 \rangle}{\sigma_p^3}.$$

Though the magnitude of the skewness is not expected to exceed the 0.4 threshold to signify the presence of crackle, a reduction in baseline skewness values will suggest a reduction in the Mach wave radiation noise source. The skewness results for these same data are shown in Figure 4.5.15 below.

There are several points of note to be observed in these results. The baseline skewness values lie consistently about the 0.037 level. The crackle threshold value for skewness is 0.4. Since we do not expect crackle as a noise source to be present in these experiments, the low baseline skewness level is not surprising. At pressures of 600 psig and below, the skewness of the signal is increased slightly. Previously, increases in high-frequency noise were observed in the spectra for these conditions, suggesting that the microjets interfere constructively with the Mach wave radiation noise source. At pressures above 600 psig, the skewness value is decreased below the baseline value, suggesting that, at these pressures, the Mach wave radiation noise source is reduced due to the microjet's ability to more effectively penetrate the shear layer of the main jet. OASPL values at microjet injection pressures above 800 psig along with the corresponding observable spectral reductions at higher frequencies would suggest that the skewness at these conditions should be dramatically reduced below baseline levels. Such reductions would serve as further proof that the microjet's ability to penetrate to the high-speed side of the shear layer is significantly responsible for the reduction in the Mach wave radiation noise source. Indeed, from Figure 4.5.15, it can be seen that the skewness values for these conditions are reduced well below their corresponding baseline values –

nearly to a full 50% of their original values. Observable microjet penetration to the high-speed side of the shear layer, visible reduction in high-frequency spectral content, and finally a reduction in the skewness of the pressure-time signal for these specific cases provide strong evidence to the idea that this particular property of the microjet is responsible for the reduction of high-frequency noise sources – specifically, Mach wave radiation.

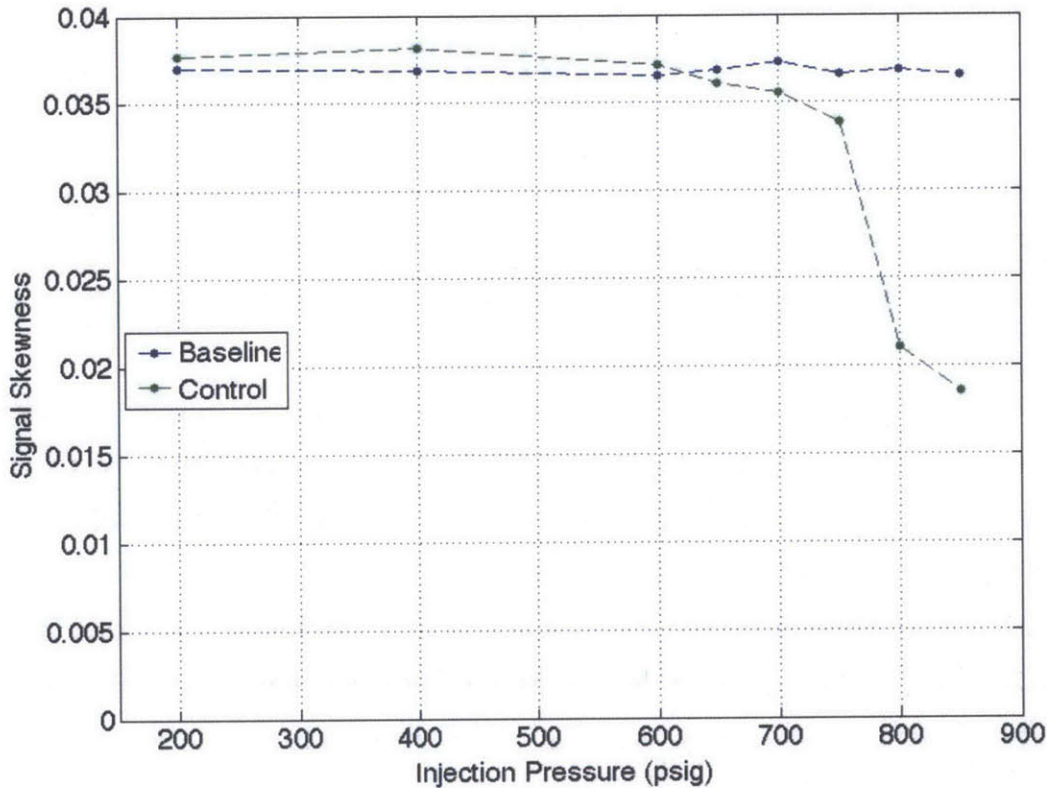


Figure 4.5.15: Skewness of the pressure-time signal for baseline and control signals as a function of microjet injection pressure. At pressures of 600 psig and below, the skewness is increased over the baseline value, illustrating the constructive interference produced by the microjet. A crossover before 650 psig suggests a net reduction in Mach wave radiation, while the substantial drop off of the skewness at pressures of 800 psig and above provide corroborating evidence that the microjet is penetrating to the high-speed side of the shear layer, and is more effectively reducing this noise source.

A summary schematic of the effect of microjet penetration depth on the farfield frequency spectra of a supersonic jet is shown in Figure 4.5.16. Penetrating into the high-speed side of the shear layer, the stronger microjets are able to break up large-scale vortical structures, which grow favorably in that region.

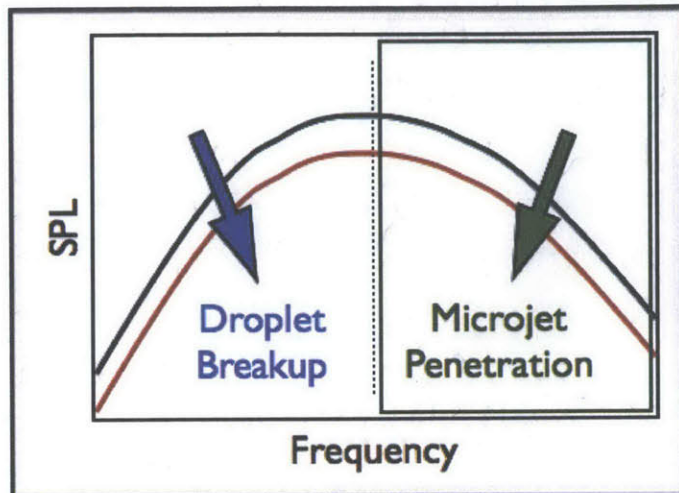


Figure 4.5.16: Simple summary schematic showing the effect of microjet penetration on the frequency spectra. Penetrating into the high-speed side of the shear layer, the stronger microjets are able to break up large-scale vortical structures, which grow favorably in that region.

CHAPTER 5

CONCLUSIONS AND FUTURE STUDY

5.1 Conclusions

The average temperatures obtained using thermocouples flush-mounted in the ground plane show good agreement with the pressure data previously acquired with flush-mounted Kulites in the same locations. The mean temperatures decrease monotonically with radial distance from the jet centerline. One would expect this to be true for an impinging jet. At an axial distance of 8 nozzle throat diameters downstream, it was found that while there is a clear maximum in the standard deviation of temperature at the jet centerline, there is also a local maximum at an $r/d = 1.53$ for all temperatures. This would serve to suggest that, in order to effect the most noise suppression at the ground plane, one would have to install some form of control at that location. At an axial distance of 10 nozzle throat diameters downstream, it was found that this result held true for temperature ratios up to 3.59. Above this temperature ratio, however, it was found that this local maximum seemed to move outward to an r/d of 2.30.

Looking at the spectra obtained from the microphone signals in the far-field, it was found that good agreement exists between the results obtained here and those obtained previously. At an axial distance of 8 nozzle throat diameters downstream, there exist strong feedback tones in each of the cases studied here. It is also clear that aqueous microjet injection at the ground plane for these cases attenuates the tonal strength of this feedback phenomenon. For temperatures of 60°F and 600°F, additional reduction of

high-frequency, broadband noise is produced. However, at 1000°F, the aqueous microjets actually produce a parasitic increase in the high-frequency, broadband noise. This would serve to suggest that ground plane microjet injection is effective in breaking the feedback loop associated with strong resonance tones. At lower temperatures, it also produces a bonus reduction in high-frequency broadband noise.

At an axial distance of 10 nozzle throat diameters downstream, it is similarly seen that aqueous microjet injection is effective in attenuating the strong tones associated with feedback. Also, as with the previous case, microjets produce an additional benefit of high-frequency broadband noise reduction. This is especially clear from the 90 degree sideline microphone. However, it was also observed that there exist no feedback tones at higher temperatures for this axial distance. Therefore, the only effect of water microjets is to exacerbate the high-frequency broadband noise.

In summarizing the OASPL reductions achieved with aqueous microjets on the ground plane, it was found that, for a jet operating at the cold condition, increasing the injection pressure (and therefore the flow rate and amount of water injected) produced greater reductions in the OASPL. However, a drastic increase in noise reduction for the 90 degree microphone is achieved at microjet injection pressures greater than 750 psig.

Similarly, for a jet operating at 600°F, larger microjet injection pressures produced better results with respect to reductions in the farfield OASPL. However, no reduction was achieved for injection pressures at 600 psig or less. At pressures above 600 psig, net reductions in noise were produced. As temperature increases, larger microjet injection pressures are required to produce appreciable noise reductions. This is due to the increased rate of growth of the shear layer. For hotter jets, the thickness of the shear layer at the ground plane is larger, and the microjet must effectively punch through a thicker layer. Therefore, only higher-pressure microjets are able to accomplish this.

For the sake of comparison, many additional variables were tweaked in order to measure their influence on the noise reduction of the impinging jet. First, microjets were affixed to the nozzle exit to compare the results obtained with ground plane microjets to those obtained by means of a more historically typical implementation location. As

expected, it was found that much larger reductions in noise are obtained with microjets at the nozzle exit. This is the optimal location for such control. However, within the constraints of the problem, such implementation is not possible. The amount of noise reduction decreases as a function of the main jet operating temperature. It was also found that larger reductions were obtained in this study as a result of the attenuation of feedback tones that are inherent in impinging flows, but which are not present in free jet flows. Also as expected, as injection pressure increases, the OASPL reduction increases.

Using nitrogen as the working fluid in microjets at the nozzle exit produced consistent reductions in OASPL regardless of injection pressure. At higher injection pressures, the microjets exhaust supersonically into the shear layer of the main jet and act as sources of high-frequency, shock-associated noise in and of themselves. This serves to counteract any additional reduction in noise attained through the increased flow rate.

Microjet locations of one, two and three inches were also studied. It was found that, for the cold jet, reductions near 5 dB were obtained when the microjets were placed at a radial distance of two inches. The amount of reduction at this location decreased with temperature. Another interesting finding is that the local maximum for both the $r=1$ and 3 locations at a temperature of 600°F. For example, microjets at a radial distance of one inch are able to produce a reduction of over 5 dB. This local maximum behavior is likely due to the change in evolution of the shear layer at higher temperatures. Starting closer to the jet centerline (as is the case for the microjets at a radial distance of one inch) allows the microjets to penetrate farther into a thicker shear layer.

Another variable investigated through the course of this study was the injection angle of the microjets. Greska determined that the optimum injection angle of microjets at the nozzle exit is 60 degrees from the direction of exhaust. In his study, it was found that this angle allowed for the microjet to more effectively penetrate the shear layer by slipping between the convected Mach waves of the shear layer, parallel to their angle of propagation. This is not physically possible from the ground plane, as it would require either outward injection or injection into the ground plane. Neither of these options makes physical sense. Therefore, as an alternative, an injection angle of 30 degrees from the ground plane normal was chosen, as it is perpendicular to the angle of the Mach wave

radiation. In order to test the effect of injection angle on the microjets' ability to reduce noise, a series of tests was performed using oblique microjets at 30 degrees from the normal and tangential microjets at 0 degrees from the normal. It was found that the tangential microjets did not produce appreciable reductions in the OASPL. However, conclusions could be drawn from the spectra obtained from these tests.

It was seen that the tangential microjets were not effective in reducing feedback tones. This is due to the fact that, as they are injected tangentially, they are not able to penetrate the shear layer and break the feedback loop. They are also not capable of reducing the high frequency, shock-associated noise, as shear layer penetration is required for this as well. They are, however, able to marginally decrease the lower frequency, turbulence-associated noise, as some of the microjet fluid is broken away and swept into the shear layer. Once there, it acts as a momentum sink, reducing the shear layer vorticity as a result of its larger density.

Oblique microjets, on the other hand, are capable of reducing feedback tones and high frequency, shock-associated noise, as they are effective at penetrating the shear layer. They are also much more capable of reducing higher-frequency, turbulence-associated noise, as the microjet is able to penetrate the shear layer before it is broken up. Therefore, more fluid is conveyed to the shear layer where it can more effectively be broken up into smaller and smaller droplets.

For the experiments run in the imaging portion of this study, it was determined that the droplet breakup based on the Weber and Ohnesorge numbers was in the shear regime, as outlined by Hsiang and Faeth [48], even more so than in previous studies [4]. This is largely due to the higher relative velocity between the fluids, as the geometry in this study allowed for microjets whose exit velocity was in a direction counter to the flow of the main jet. This droplet breakup is responsible for the reduction of low frequency noise, and is evidenced by mist (and quantified by the average pixel value in the shear layer).

From the accompanying videos to this thesis, some other observations were made. As the microjet pressure is increased, the exit velocity of the jet, and therefore the volumetric flow rate of the jet, is increased. The microjet interacts with the shear layer of

the jet in complex ways, and the depth is influenced significantly by slower, flapping modes of the main jet. The flapping of the jet can be observed visually, as well as analytically, from the videos – especially when the microjet is operated at higher pressures. As the jet flaps down toward the microjet, the microjet penetrates the shear layer and is eventually broken down into a fine mist consisting of small droplets. These droplets accumulate in the shear layer until the jet flaps back up away from the microjet, at which time the wall jet washes away the mist. The visual observation of the flapping of the main jet as well as the breakup of the microjet in the shear layer and the accumulation of mist in the recirculation regions of the flow field were also shown through the computation of the fast Fourier transform of the brightness of the shear layer from the videos.

A more subtle point involves the penetration depth of the microjet. While the upstream and inward penetration depth increases, as expected, with injection pressure, this simple increase in depth cannot fully account for the increased noise reduction achieved at higher injection pressures. However, the structures responsible for high-frequency shock-associated noise favor the high-speed side of the shear layer. At microjet injection pressures above 700 psig, the coherent microjet is able to penetrate into the high-speed side of the shear layer, thus drastically increasing its effectiveness in breaking up these structures.

Support for this hypothesis was also provided from the frequency spectra at each of the microjet conditions. For low-pressure cases, the feedback tones are not significantly reduced. As seen from the videos and selected images of the microjet, this is due to the fact that the control does not have the power required to penetrate the shear layer in any meaningful way. It is, rather, deflected away from the centerline by the shear layer and wall jet of the main jet. Also there is actually an increase in the high-frequency shock associated noise. The microjet actually interferes constructively with this noise source.

It was however shown that, even for microjets at low pressures, lower frequency noise is reduced. This effect increases as the microjet injection pressure is increased. This is verified by observations from the videos, which suggest that, as the pressure

increases, the volumetric flow rate and exit velocity of the microjet also increase. This increased water volume allows for the accumulation of water droplets in the shear layer. This accumulation is responsible for the reduction in size and strength of large-scale vortical structures in the shear layer. These sources are responsible for much of the low-frequency spectral content.

More importantly, as the pressure is increased to 650 psig and above, the feedback tones are more effectively suppressed. Above pressures of 750 psig, little remains of these tones. The authority of the control for these cases has reached a point so as to allow the microjet to penetrate sufficiently far into the shear layer to effectively break the feedback loop.

It was also shown that high frequency noise is more significantly reduced as the pressure of the microjet is increased. At and above microjet injection pressures of 800 psig, it is able to penetrate into the high-speed side of the shear layer – a necessary requirement for the reduction of high frequency turbulent mixing and shock-associated noise reduction.

Further support is given to the proposal of these two mechanisms by the results of the experiments investigating microjet injection angle. It was shown that tangential microjets are not effective in reducing feedback tones. This is due to the fact that, as they are injected tangentially, they are not able to penetrate the shear layer and break the feedback loop. They are also not capable of reducing the high frequency, shock-associated noise as seen from the frequency spectrum. This is due to the fact that shear layer penetration is necessary in order to reduce this noise source. With no radial component to their exit velocity, the tangential microjets are not able to penetrate towards the high-speed side of the shear layer.

In this respect, the droplet breakup and penetration mechanisms are somewhat coupled. While some fluid is conveyed to the shear layer and broken up into smaller and smaller droplets therein, tangential microjets are not as efficient in this conveyance as oblique microjets due to the lack of the radial velocity component. The reduction of lower frequency spectral energy is not as substantial with tangential microjets as with oblique ones.

To decouple the effects of misting from penetration depth, the baseline and control skewness of the pressure-time signal was computed for each of the operating conditions. The baseline skewness values were found to lie consistently about the 0.037 level. The crackle threshold value for skewness is 0.4. Since crackle was not expected in these experiments, the low baseline skewness level is not surprising. At pressures of 600 psig and below, the skewness of the signal is increased slightly. Previously, increases in high-frequency noise were observed in the spectra for these conditions, suggesting that the microjets interfere constructively with the Mach wave radiation noise source. At pressures above 600 psig, the skewness value is decreased below the baseline value, suggesting that, at these pressures, the Mach wave radiation noise source is reduced due to the microjet's ability to more effectively penetrate the shear layer of the main jet. OASPL values at microjet injection pressures above 800 psig along with the corresponding observable spectral reductions at higher frequencies would suggest that the skewness at these conditions should be dramatically reduced below baseline levels. Such reductions would serve as further proof that the microjet's ability to penetrate to the high-speed side of the shear layer is significantly responsible for the reduction in the Mach wave radiation noise source. It was shown that the skewness values for these conditions are reduced well below their corresponding baseline values – nearly to 50% of their original values. Observable microjet penetration to the high-speed side of the shear layer, visible reduction in high-frequency spectral content, and finally a reduction in the skewness of the pressure-time signal for these specific cases provide strong evidence to the idea that this particular property of the microjet is responsible for the reduction of high-frequency noise sources – specifically, Mach wave radiation.

This study was admittedly limited in the number of parameters that could be tweaked and studied as well as the range those parameters could be changed. In order to adjust one of the parameters, an entirely new center ground plane had to be machined. This involved obtaining the raw ¼ inch stainless steel plate stock, water jetting the plate into the correct rough shape, and finally finishes machining the plate to the specific dimensions. On each plate, microjet tubing had to be mounted and soldered in place, then mounted and centered to the ground plane. Such a procedure did not allow for adjustment of parameters in a timely manner. Therefore, the precision to which

parameters such as radial location and injection angle are optimized is very low. Therefore, future work should include refining the microjet mounting technique to allow for finer control and adjustment of these very important parameters.

The camera used to obtain the high-speed images was also limited. While the images it obtained gave valuable insights into the flow mechanisms responsible for producing noise reductions, more precise conclusions could be drawn from a camera with a higher resolution and a higher sampling rate. A PIV analysis would be useful as well in accurately determining and quantifying the droplet effect on the turbulence of the shear layer. Comparisons between the turbulence with and without control would likely yield lower vorticity levels in the shear layer with control. However, given the state of the current facility, many extreme modifications – including plumbing in a water supply for the laser, the installation of an upstream flow seeding mechanism and steps taken to ensure the safe operation of PIV test setups in the presence of strong (and sometimes very high-temperature) flows – would need to be made. Such modifications were not feasible under the time and financial constraints imposed upon the current study. For this reason, a detailed experimental plan is provided. This plan includes a discussion of experiments that would definitively prove the effect and responsibility of ground-plane microjets on the reduction of each noise source.

The experiments carried out in this study were all performed at the High Temperature, Supersonic Jet Facility at Florida State University. With respect to the F18 fighter aircraft, the nozzle used in this experiment is a 1/7-scale jet. Acoustically, frequency scales inversely with the relevant length scales in the geometry – in this case, nozzle diameter. Therefore, to compare the noise generated in this study with that produced by a full-scale jet engine, the frequencies should be divided by 7.

With respect to design, the thrust generated by a jet engine can be calculated quite simply through the principle of conservation of momentum and isentropic fluid flow relations. First, it is necessary to select an appropriate control volume around the jet engine. The control volume and jet engine are shown in Figure 5.1 below.

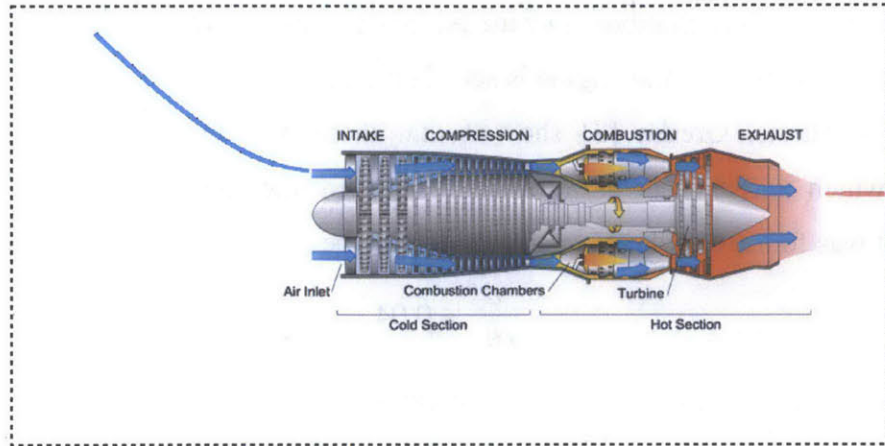


Figure 5.1: Schematic of the jet engine with a control volume, as modified from [50]. The control volume is indicated with the dashed black line. The entering streamline (blue) may be assumed to have zero velocity at the left control volume boundary, while the exiting streamline (red) exits at a much higher velocity. This velocity disparity produces the thrust.

First, the principles of conservation of mass and momentum are applied to the control volume. They are as follows:

$$\frac{d}{dt} \iiint_V \rho dV + \iint_S \rho \vec{U} \cdot \hat{n} dS = 0$$

$$\frac{d}{dt} \iiint_V \rho \vec{U} dV + \iint_S \rho \vec{U} (\vec{U} \cdot \hat{n}) dS = -\vec{F}_e - \iint_S p \hat{n} dS$$

The first equation, known as fluid mechanical continuity, states that the change in mass in the control volume plus the fluid flow out of the control volume must be equal. The second equation, describing conservation of momentum, relates the rate of change of momentum to the flow of momentum out of the control volume, external forces, and surface pressure forces. In the case of the jet engine, conservation allows for a relation of the input and output velocities. In the case of the momentum equation, during steady operation, the momentum in the control volume is constant. Also, the pressure on all surfaces of the control volume is the same. Therefore, the thrust force, F_e , is related only to the momentum flux through the control volume. Simply put, the thrust force is given as

$$F_T = -\rho U_e^2 A \hat{e}_x.$$

Given the thrust requirements of the aircraft, either the exhaust Mach number can be defined to dictate the required exit area, or the engine configuration can be defined to

dictate the exhaust Mach number. For the purposes of this exercise, it is assumed that the geometric configuration of the engine is set. Therefore, an exhaust velocity is computed.

In his thesis, Greska [3] showed that there was an optimal spacing of the microjets, which is related to the arc length between microjets and the diameter of the microjet. It was found that the optimal ratio should be

$$\frac{d}{r\theta_m} = 0.04.$$

The microjets in this study had an exit diameter of 1.0 mm. Using water jets with a 2.4 mm diameter satisfying this requirement would require 38 nozzles.

His work also determined that the momentum ratio of the radial component of the microjet to the main jet should be 10. Beyond this number there is an insignificant increase in noise reduction. Therefore, the extra effort in injecting the additional fluid cannot be justified. As such, the flow rate of the microjets should be chosen such that

$$10 = \frac{N_\mu \rho_\mu U_\mu^2 d \cos^2 \theta}{\rho_j U_j^2 D},$$

where N_μ is the number of microjets, d is the microjet diameter, θ is the angle of injection from horizontal, and D is the main jet exit diameter. Substituting this equation into the thrust equation and solving for the microjet exit velocity yields

$$U_\mu^2 = \frac{40F_T}{\pi\rho_\mu d^2 \cos^2 \theta}$$

$$U_\mu = \frac{2}{d \cos \theta} \sqrt{\frac{10F_T}{\pi\rho_\mu}}.$$

This equation can be used in conjunction with the spacing equation to provide a full design of the ground plane microjet control meeting the requirements of the application.

5.2 Future Work Plan

In this thesis, it has been established (specifically through the work of Crighton [1]) that there exist three main components of jet noise: turbulent mixing noise, resonance and broadband shock noise. These noise sources were shown by Kandula [2] to inhabit three different regions of the narrowband, far-field, noise spectra as shown in Figure 5.2.

The figure, originally published by Crighton, was modified by Kandula in order to show these specific noise regions.

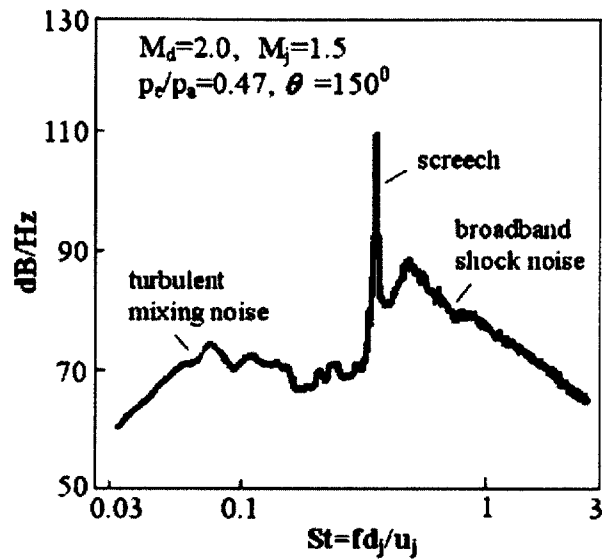


Figure 5.2: The three main noise sources and their contributions to the narrowband frequency spectrum.

Up to this point, it has been shown that microjet injection at the ground plane is capable of reducing each of the three noise sources. Much of the previous work concerned with the identification of noise suppression mechanisms deals with free and impinging jets whose control technique is applied at the nozzle exit. Krothapalli et al. [4] demonstrated that, in their experiments, the fluid microjets used in their study involved droplet breakup in the shear regime. This was mostly attributed to the high velocities associated with the flow in their setup. This study also showed that atomized microjets injected at the nozzle exit reduced the intensity and size of large-scale, coherent, turbulent structures (eddies) in the shear layer. The results of this study are reproduced in Figure 5.3.

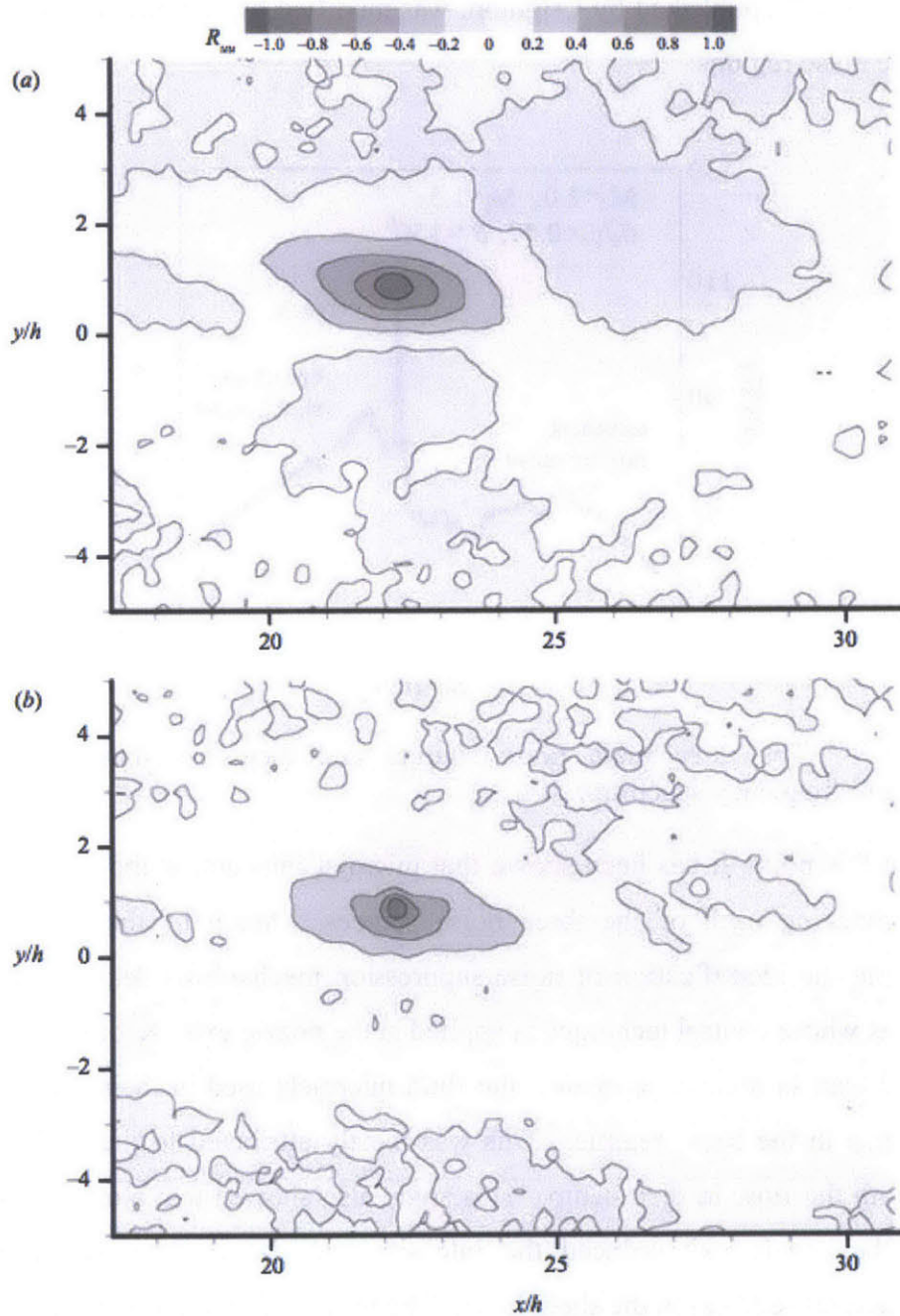


Figure 5.3: Shear layer turbulence profiles as reproduced from Krothapalli et al [4] showing the jet (a) without control and (b) with water microjet control. It can be clearly seen from this figure that the representative size and magnitude of large-scale, coherent structures propagating in the shear layer are reduced through the use of atomized water injection.

Further, Krothapalli showed that the shear layer turbulence intensity was reduced through the use of atomized water injection, shown here in Figure 5.4. As previously

discussed, turbulent mixing noise is both a subsonic and a supersonic source. It results from the growth of instabilities born at the inception of the shear layer into coherent structures with coherent vorticity. The growth of these structures is attributed to the large velocity gradients and shear forces present in the shear layer. Reduction in the shear layer vorticity is a clear indication that the turbulent mixing noise (occupying the low-frequency region of the noise spectrum) is reduced as well.

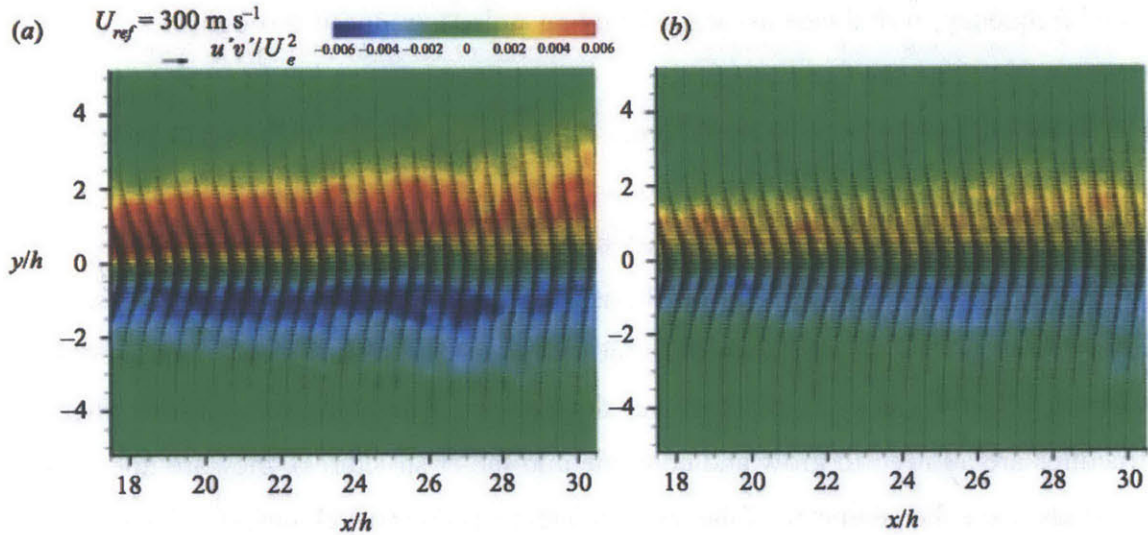


Figure 5.4: Normalized turbulence profiles within the shear layer for a jet (a) with no control and (b) with atomized microjet injection, as reproduced from Krothapalli [4]. It can be clearly seen from these profiles that the turbulence intensity associated with atomized microjet injection is much reduced from the baseline case.

Later, Greska [3] demonstrated, through the use of low-pressure water microjets mounted at the nozzle exit of a free jet, that the breakup of the water droplets could be responsible for the reduction in low-frequency broadband noise. Using low-pressure microjets ensured that the control lacked the authority required to penetrate the shear layer in any meaningful way. Rather, any noise reduction achieved would be the result of the breakup of the microjet into smaller and smaller droplets within the shear layer. As shown earlier in this thesis, his results show a reduction of lower frequency noise only. Over a broad range of experimental conditions encompassing both subsonic and supersonic flows, Greska [3], Krothapalli [4] and Washington [6] were able to show reductions to low-frequency, turbulence-associated mixing noise were achievable through the use of low-pressure, atomized microjets.

Within the scope of this work, noise reductions in the frequency spectra demonstrate reductions in noise for all frequencies (including the lower frequencies associated with turbulent mixing noise) when microjet pressure is sufficiently high. When microjet pressure is high enough to cause significant misting and droplet entrainment in the shear layer, but not high enough to penetrate the shear layer in any meaningful way, reductions in low frequencies are still achieved. This suggests that the lower frequency, turbulence associated mixing noise is reduced through the breakup of the microjet within the shear layer.

Strictly a supersonic noise source, Mach wave radiation is the result of coherent, turbulent structures convecting supersonically with respect to the ambient environment. The resulting Mach waves can be seen propagating from the Schlieren image [51] in Figure 5.5. It has been shown in this thesis that, in the region of interest, this is strictly a high frequency, small-scale phenomenon. While large-scale, lower frequency Mach wave radiation sources can exist farther downstream within the shear layer (where the structures are allowed to grow and combine into larger structures), they are not found in this study since the geometry of the test setup restricts their development.



Figure 5.5: Unprocessed Schlieren image showing the presence of Mach wave radiation as reproduced from Pappaschou [51]. The individual Mach waves can be observed clearly from this representative, unprocessed Schlieren image.

As shown previously, when the authority of the microjet is increased (beyond 750 psig injection pressure), high-frequency noise associated with Mach wave radiation is reduced. It was found that, for these cases, two measurable quantities are also changed beyond their threshold values. First, the microjet is able to penetrate to the high-speed side of the shear layer. Crighton [1] showed that the structures responsible for this noise source favor the high-speed side of the shear layer. Therefore, reaching that region of the jet should result in the reduction of that noise source – such as is seen in this study. Second, the skewness of the pressure-time signal (which is related to the amount of Mach wave radiation present in the noise profile) is significantly reduced below the baseline levels for cases above 750 psig.

First, as computed by Krothapalli et al [4], a water droplet size distribution must be computed. In their study, this measurement was performed and a droplet size probability distribution function (PDF) was computed in order to ensure that the droplet size within the area of interest was of sufficiently small size so as not to interfere with the PIV processing algorithm. Therefore, in so establishing the size of the droplets, the researchers ensured that the cross-correlation of the interrogation regions were influenced only by the seeding particles and not by the water droplets.

This experiment would be implemented through the use of a TSI Powersight solid-state, laser-based phase Doppler particle analyzer (PDPA) set to 2-D configuration mode (Model TR-SS-2D) in order to measure and analyze the droplet size PDF. This particular system setup is shown in Figure 5.6. The 2-D configuration mode includes a set of optics to allow for the laser to be transformed into a sheet, allowing for 2-D planar flow field measurements.

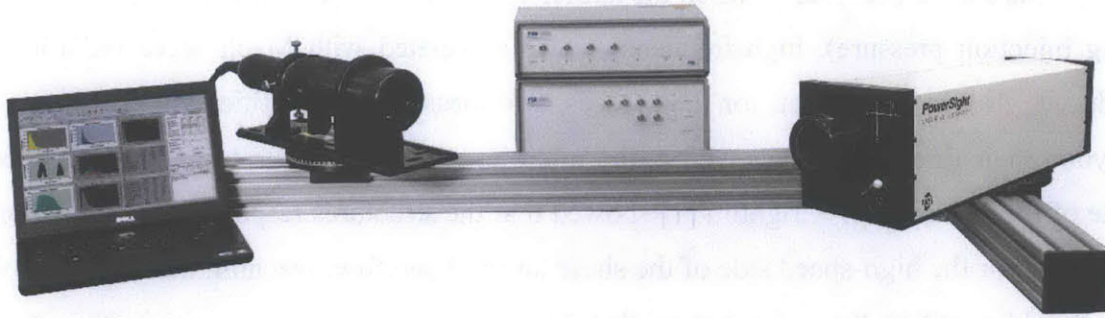


Figure 5.6: Schematic of a TSI Powersight solid-state, laser-based phase Doppler particle analyzer. This setup would be used in order to determine the particle size PDF of the microjet droplets. The purpose of this experiment would be to ensure that the water droplets in the shear layer are small enough to ensure that the PIV analysis includes only the cross-correlation of the seeding particles.

Once the droplet size in the region of interest has been established, a seeding material must be chosen. Ideally, seed particles should be of comparable density to the working fluid of the main jet. This is to ensure that the particle will follow the working fluid flow. Also to be considered is the scattering signal of the seed particles. The particles will be entrained in a fluid consisting of both air and small water droplets, so the seeding particles must produce a light scatter signal stronger than that of the water droplets. Metallic coated seed particles produced by TSI (Model number 10087) would be optimal. They have a low density at 2.6 g/cc, and a refractive index of $0.21 + 2.62i$. The significant real and imaginary components of the metallic-coated seed particles ensure a strong scatter signal and are therefore suitable for liquid as well as gaseous flows. Additionally, the nominal diameter listed for these particles is $9\mu\text{m}$. The particle size listed in the study performed by Krothapalli et al [4] was $4\mu\text{m}$ and smaller. It is expected that, since the Weber number for this study is larger than that of Krothapalli (owing to the increased relative fluid velocity), the droplet size in this study would be equal or less in diameter. Choosing these particular seed particles would ensure that they are: sufficiently small in density to ensure that they follow the flow field; and large enough in size and capable enough to produce a sufficiently strong scatter signal to negate the effect of the water droplets in the flow field. It should be noted that, in the unlikely case the droplet size is larger than that of Krothapalli, the seeding particle size should be increased accordingly.

With respect to implementation, the jet facility described in these experiments is already outfitted with an injection port upstream of the burner section. This port consists of a ¼ inch NPT hole through which an L-shaped section of tubing is inserted. The lower leg of the “L” orients the input flow along the centerline in the direction of flow. A subsequent turbulator and flow straightener would ensure that the particles are evenly dispersed before reaching the nozzle. The same PDPA system is capable of performing the PIV analysis in 2-D mode. A schematic of the proposed setup is shown in Figure 5.7.

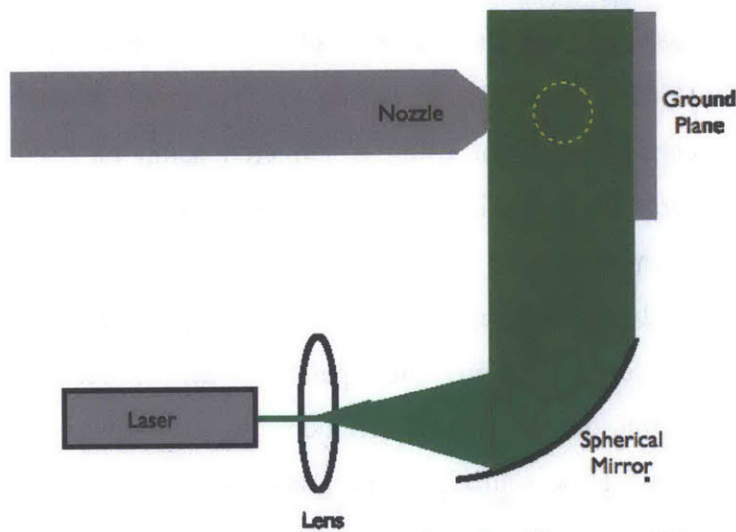


Figure 5.7: Simple schematic of the PIV setup. The flow would be seeded upstream of the nozzle exit. The camera lens would be pointed at the laser sheet as viewed from this paper. It is shown by the yellow, dotted circle.

First, a PIV experiment would be run on the seeded flow without microjet injection. The purpose of this experiment is two-fold. First, to characterize the baseline flow field characteristics – namely, to quantify the baseline turbulence levels within the shear layer. Beyond this, the average intensity of the particle-laden flow would be measured. The threshold of the cross-correlation algorithm would be set at this level in order to minimize the influence of large droplets within the flow on the PIV analysis. Then, this experiment would be repeated using microjets at varying pressures to quantify their effect on the turbulence intensity within the shear layer.

The purpose of the aforementioned experiments would be to quantify the effect of the droplet breakup and entrainment on the reduction of turbulence associated noise. While Mach wave radiation is a result of the turbulent structures convecting

supersonically, the PIV technique provides no way to visually measure or quantify the existence and magnitude of this particular noise source. This is due to the fact that turbulent mixing noise is a flow phenomenon – that is to say that it can be measured directly from the velocity of the fluid. Mach wave radiation is a result of pressure – and therefore density – gradients in the fluid. Therefore, a second experiment would need to be performed that could allow for the observation of these density gradients.

Historically, density variations in fluid flow have been observed through the use of two particular methods: schlieren and shadowgraph. For example, the images reproduced here by Papmoschou [51] in Figure 5.5 are sample schlieren images. It is proposed that a second experiment using a schlieren setup be used to observe and quantify the density gradients associated with Mach wave radiation. Since the refractive index of a fluid is a function of its density, comparing light that travels through denser areas would be diverted from its original path. Comparing this light to undiverted light produces a sort of interference pattern – this pattern, when viewed by a camera, shows the streaks corresponding to the density gradients in the flow. Much of the same equipment can be used for the schlieren experiments as used for the PIV experiments, since the basic components are the same. Some additional optics would be used including a knife edge – this is used to compare the disturbed light to the undisturbed light. A schematic of the proposed setup is shown in Figure 5.8.

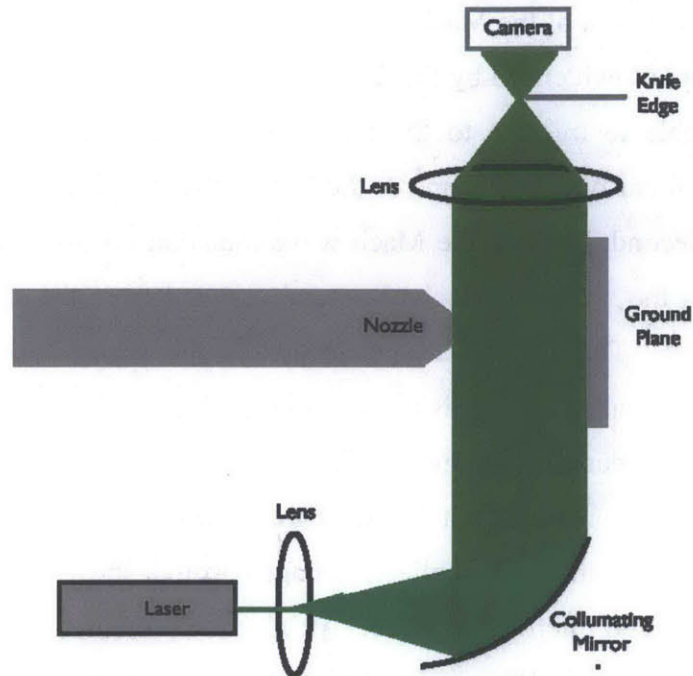


Figure 5.8: Simple schematic of the schlieren setup. A second lens and a knife edge are used in addition to the PIV setup in order to be able to compare the refracted light to the undisturbed light. This comparison produces the schlieren images.

The laser light first passes through a diverging lens, and then reflects off of a schlieren mirror. The mirror is used to redirect the light to the target, but is also concave to collimate the light. After passing through the target area (in this case the jet), the light is passed through a converging lens. At the focal point is placed a knife edge. This separates the undisturbed light from the disturbed light and enables the two images to be compared at the camera. The result is a schlieren image showing any density gradients in the flow.

First, a baseline schlieren experiment will be conducted in order to observe and quantify the Mach wave radiation present in the flow before control is implemented. Then, further schlieren experiments will be performed with microjet control using varying injection pressures. These control experiments will be performed using only one microjet for comparison with the high-speed videos presented in this study.

Schlieren imaging techniques are traditionally used only for single-phase flow visualization. Here, however, a two-phase flow is present. The water droplets in the flow during the control cases will also cause the light to refract. However, this should not

prevent the visualization of the Mach waves. First, recirculation of the water droplets is a 3-D phenomenon, as evidenced by the fact that some of the water droplets from the upper microjet were able to migrate to the bottom of the main jet nozzle. The schlieren experiment will focus on a 2-D plane of the flow, thereby reducing the amount of visible recirculation. Second, because the Mach wave radiation results from the convection of turbulent eddies, the waves themselves extend outward from the shear layer, as can be seen in Figure 5.5. The droplets are not located in this region and would therefore not affect visibility. Finally, water has a much higher density than the Mach waves. They would appear much darker than surrounding features. Setting a lower threshold on the images would effectively block out the water from the images.

It is expected that the schlieren images would show decreasing Mach wave radiation for increased microjet pressure. At injection pressures greater than 750 psig, it is expected that a dramatic decrease in Mach wave radiation would be observed.

As previously discussed, Crighton [1] and Laufer [11] observed two classes of Mach wave radiation – small-scale, high frequency located 5-8 nozzle diameters downstream and large-scale, low frequency located 12-16 nozzle diameters downstream. Moving the ground plane farther downstream – say to 20 nozzle diameters – would allow the second class of radiation to develop. Performing a final baseline experiment on this flow field and analyzing the images for Mach wave spacing could visually confirm the existence of these two classes. An increase in the shock spacing beyond 10 nozzle diameters should be apparent from the resulting schlieren images.

Finally, an imaging experiment should be performed to produce high-speed images of higher fidelity. As discussed earlier, the high-speed images presented in this thesis provide a 2-D representation of a 3-D phenomenon. Images with higher fidelity could be obtained using the PIV setup. The laser would illuminate a planer section of the jet going from the top through the bottom. Then, using the same camera, images could be obtained clearly showing the extent of the microjet's penetration into the shear layer. Since the laser only illuminates a plane through the main jet, the 3-D flow of the droplets around the jet would not appear in these images.

To summarize, Table 5.1 enumerates the experiments to be performed, the purpose of those experiments, and the order in which they should be performed.

Table 5.1: Experimental summary for future work. The order and purpose of each experiment is given in this table.

No.	Description
1	Baseline PIV without control to quantify the turbulence within the shear layer of the jet. The threshold of the images will be determined and set from this experiment
2	Repeated PIV experiments with control of varying pressure to determine the effect of the microjets on turbulence within the shear layer. The threshold found in 1 will be used for this experiment too in order to minimize the effect of large water droplets.
3	Using the PIV setup, high-speed images will be obtained to determine the extent of the microjet's penetration into the shear layer of the main jet. This will produce higher resolution images than those presented in the current work.
4	Baseline schlieren experiment will be performed to quantify the initial amount of Mach wave radiation present in the flow.
5	Additional schlieren experiments will be performed using varying microjet back pressures. These will enable the quantification of the amount of reduction of Mach wave radiation of the jet through microjet use.
6	Final schlieren experiment on the full flow field, with the ground plane moved downstream. This will allow for observation of the two classes of Mach wave radiation described by Crighton [1] and Laufer [11].

BIBLIOGRAPHY

- [1] D. G. Crighton. Orderly structure as a source of jet exhaust noise: Survey Lecture. *Structure and Mechanisms of Turbulence II*, vol. 76, *Lecture Notes in Physics*, 154-170, 1977.
- [2] M. Kandula. Broadband shock noise reduction in turbulent jets by water injection. *Applied Acoustics*, Vol. 70, pp. 1009-1014, 2009.
- [3] B. J. Greska. Supersonic jet noise and its reduction using microjet injection. PhD thesis, Florida State University, 2005.
- [4] A. Krothapalli, L. Venkatakrishnan, L. Lourenco, B. Greska and R. Elavarasan. Turbulence and noise suppression of a high-speed jet by water injection. *Journal of Fluid Mechanics*, Vol. 491, pp. 131-159, 2003.
- [5] J. D. Kulick, J. R. Fessler, J.K. Eaton. Particle response and turbulence modification in fully developed channel flow. *Journal of Fluid Mechanics*, 277:109-134, 1994.
- [6] D. Washington, A. Krothapalli. The role of water injection on the mixing noise of a supersonic jet. *AIAA Journal*, 1998-2205.
- [7] D. Papamoschou and A. Roshko. The compressible turbulent shear layer: an experimental study. *Journal of Fluid Mechanics*, 197:453-477, 1988.
- [8] S. C. Crow and F. H. Champagne. Orderly structure in jet turbulence. *Journal of Fluid Mechanics*, 48:547-591, 1971.
- [9] C. J. Moore. The role of shear-layer instability waves in jet exhaust noise. *Journal of Fluid Mechanics*, 80:321-367, 1977.
- [10] K. A. Bishop, J.E. Ffowcs Williams and W. Smith. On the noise sources of the unsuppressed high-speed jet. *Journal of Fluid Mechanics*, 50:21-31, 1971.
- [11] J. Laufer, R. Schlinker, R. E. Kaplan. Experiments on supersonic jet noise. *AIAA Journal*, 14, 4, 489-497, 1976.

- [12] B. J. Greska, A Krothapalli, W. C. Horne, N. Burnside. A near-field study of high temperature supersonic jets. *14th AIAA/CEAS Aeroacoustics Conference*, Vancouver, B.C., 2008-3026.
- [13] A. Powell. The noise of choked jets. *Journal of the Acoustical Society of America*, 25:385-389, 1953.
- [14] M. B. Alkisar. Flow field measurements in a screeching rectangular jet. PhD thesis, Florida State University, 2001.
- [15] L. J. S. Bradbury and A. H. Khadem. The distortion of a jet by tabs. *Journal of Fluid Mechanics*, 70:801-813, 1975.
- [16] M. Samimy, K. B. M. Q. Zaman and M. F. Reeder. Effect of tabs on the flow and noise field of an axisymmetric jet. *AIAA Journal*, 31(4):609-619, 1993.
- [17] D. Papamoschou and M. Debiasi. Directional suppression of noise from a high-speed jet. *AIAA Journal*, 39(3):380-387, 2001.
- [18] D. Papamoschou. Noise suppression in moderate-speed multistream jets. *8th AIAA/CEAS Aeroacoustics Conference*, (2002-2557), 2002.
- [19] G. Raman, V. Kibens, A. Cain and J. Lepicovsky. Advanced actuator concepts for active aeroacoustic control. *AIAA Paper 2000-1930*, 2000.
- [20] M. B. Alkisar, A. Krothapalli and G. W. Butler. The effect of streamwise vortices on the aeroacoustics of a Mach 0.9 jet. *Journal of Fluid Mechanics*, 578:139-169, 2007.
- [21] A. Tilghman. Audit: Super Hornet a noise risk for sailors. *Navy Times*, March 9, 2009.
- [22] Naval Research Advisory Committee Technical Report. *Tactical jet noise reduction*. April, 2009.
- [23] D. Rockwell and E. Naudascher. Self-sustained oscillations of impinging free shear layers, *Annual review of Fluid Mechanics*, Vol. 11, pp. 67-94, 1979.
- [24] A. Powell. On edge tones and associated phenomena. *Acoustica*, Vol. 3, pp. 233-243, 1953.
- [25] C.-M. Ho and N. S. Nossier. Dynamics of an impinging jet. Part I. The feedback phenomenon. *Journal of Fluid Mechanics*, Vol. 105, pp. 119-142, 1981.
- [26] C. Donaldson and R. S. Snedeker. A study of free jet impingement. Part 1. Mean properties of free and impinging jets. *Journal of Fluid Mechanics*, Vol 45, No. 2, pp. 281-319, 1971.

- [27] P.J. Lamont and B. L. Hunt. The impingement of underexpanded axisymmetric jets on perpendicular and inclined flat plates. *Journal of Fluid Mechanics*, Vol. 100, pp. 471-511, 1980.
- [28] C. K. W. Tam and K. K. Ahuja. Theoretical model of discrete tone generation by impinging jets. *Journal of Fluid Mechanics*, Vol 214, pp. 67-87, 1990.
- [29] N. L. Messersmith. Aeroacoustics of supersonic and impinging jets. *AIAA Paper 95-0509, 33rd Aerospace Sciences Meeting and Exhibit*, Reno, NV, Jan 9-12, 1995.
- [30] F. S. Alvi and K. G. Iyer. Mean and unsteady flow field properties of supersonic impinging jets with lift plates. *AIAA Paper 99-1829, 5th AIAA/CEAS Aeroacoustics Conference and Exhibit*, Bellevue, WA, May 10-12, 1999.
- [31] A. Krothapalli, E. Rajkuperan, F. S. Alvi and L. Lourenco. Flow field and noise characteristics of a supersonic impinging jet. *Journal of Fluid Mechanics*, Vol 392, pp. 155-181, 1999.
- [32] B. Henderson, J. Bridges and M. Wernet. An experimental study of the oscillatory flow structure of tone producing supersonic impinging jets. *Journal of Fluid Mechanics*, Vol. 542, pp. 115-137, 2005.
- [33] J. Lepicovsky and W. H. Brown. Effects of nozzle exit boundary-layer conditions on excitability of heated free jets. *AIAA Journal*, Vol. 26, No. 6, pp. 712-718, 1989.
- [34] K. Karamcheti, A. B. Bauer, W. L. Shields, G. R. Stegen and J. P. Woolley. Some features of an edge tone flow field. *NASA SP 207*, pp. 275-304, 1969.
- [35] Y. -H. Kweon, Y. Miyazato, T. Aoki, H. -D. Kim and T. Setoguchi. Control of supersonic jet noise using a wire device. *Journal of Sound and Vibrations*, Vol, 297, pp. 167-182, 2006.
- [36] R. Elavarasan, A. Krothapalli, L. Venkatakrisnan and L. Lourenco. Suppression of self-sustained oscillations in a supersonic impinging jet. *AIAA Journal*, Vol. 39, No. 12, pp. 2366-2373, 2001.
- [37] M. Sheplak and E. F. Spina. Control of high speed impinging-jet resonance. *AIAA Journal*, Vol. 32, No. 8, pp. 1583-1588, 1994.
- [38] C. Shih, F. S. Alvi and D. Washington. Effects of counterflow on the aeroacoustic properties of a supersonic jet. *Journal of Aircraft*, Vol. 36, No. 2, pp. 451-457, 1999.
- [39] F. S. Alvi, C. Shih, r. Elavarasan, G. Garg and A. Krothapalli. Control of supersonic impinging jet flows using supersonic microjets. *AIAA Journal*, Vol. 41, No. 7, pp. 1347-1355, 2003.

- [40] H. Lou, C. Shih and F. S. Alvi. A PIV study of supersonic impinging jets. *AIAA Paper 2003-3263*, 9th *AIAA/CEAS Aeroacoustics Conference and Exhibit*, Hilton Head, SC, May 12-13, 2003.
- [41] H. Lou, F. S. Alvi and C. Shih. Active and adaptive control of supersonic impinging jets. *AIAA Journal*, Vol. 44, No. 1, pp. 58-66, 2006.
- [42] V. H. Arakeri, A. Krothapalli, V. Siddevaram, M. B. Alkislar and L. Lourenco. On the use of microjets to suppress turbulence in a Mach 0.9 axisymmetric jet. *Journal of Fluid Mechanics*, Vol. 490, pp. 75-98, 2003.
- [43] R. Kumar, S. Lazic and F.S. Alvi. Control of high-temperature supersonic impinging jets using microjets. *AIAA Journal*, Vol. 47, pp. 2800-2811, 2009.
- [44] P. T. Soderman. The prediction of STOVL noise-current semi-empirical methods and comparisons with jet noise data. *NASA TM-102833*, 1990.
- [45] E. Zoppellari and D. Juve. Reduction of jet noise by water injection. *AIAA 1997-1622*, 3rd *AIAA/CEAS Aeroacoustics Conference*, Atlanta, GA, MA 12-14, 1997.
- [46] B. Greska and A. Krothapalli. Jet noise reduction using aqueous microjet injection. *AIAA 2004-2971*, 10th *AIAA/CEAS Aeroacoustics Conference*, Manchester, Great Britain, May 2004.
- [47] T. D. Norum. Reductions in multi-component jet noise by water injection. *AIAA 2004-2976*, 10th *AIAA/CEAS Aeroacoustics Conference*, Manchester, Great Britain, May 2004.
- [48] L. -P. Hsiang and G. M. Faeth. Drop deformation and breakup due to shock wave and steady disturbances. *International Journal of Multiphase Flow*, Vol. 21, No. 4, pp. 545-560, 1995.
- [49] J. S. Bendat and A. G. Piersol. *Random Data: Analysis and Measurement Procedures*. John Wiley & Sons, Inc., New York, third edition, 2000.
- [50] J. Dahl, *jet_engine*, http://en.wikipedia.org/wiki/File:Jet_engine.svg, 2007.
- [51] D. Papmoschou. Mach wave elimination in supersonic jets. *AIAA 1997-0147*, 35th *Aerospace Sciences Meeting*, Reno, Nevada, January 1997.

Ragaller
January 10, 2014
© 2014 Massachusetts Institute of Technology
All Rights Reserved